Quantum Cutting via Broadband Sensitization in Ytterbium-Doped Lead Halide Perovskites

Tyler Jonathon Milstein

A dissertation

submitted in partial fulfillment of the

requirements for the degree of

Doctor of Philosophy

University of Washington

2022

Reading Committee:

Daniel R. Gamelin, Chair

Brandi M. Cossairt

Xiaosong Li

Program Authorized to Offer Degree:
Chemistry

University of Washington

Abstract

Quantum Cutting via Broadband Sensitization in Ytterbium-Doped Lead Halide Perovskites

Tyler Jonathon Milstein

Chair of the Supervisory Committee:

Dr. Daniel Gamelin

Department of Chemistry

The trivalent lanthanide (Ln^{3+}) family has long been utilized for optical applications such as in lasing materials, lighting, and fiber optics. Their electronic structure is dominated by coulombic interactions and spin-orbit-split valence 4*f* states that have a minimal dependence on the ligand field environment. As a result, these 4*f* states are nearly the same energy between coordination in crystalline materials and as free ions. Yb^{3+} has one *f-f* transition, $^2F_{5/2} \rightarrow {}^2F_{7/2}$, energetically well-matched to the bandgap of crystalline silicon making it a desirable phosphor for solar spectral shifting, a method of redistributing solar irradiance to a more desirable energetic regime. Furthermore, Yb^{3+} demonstrates the ability to participate in quantum cutting, a unique photophysical process in which high energy photons are converted into multiple lower-energy photons. While this process has been demonstrated numerous times in bulk morphologies using other lanthanides, transition metals, or dyes as sensitizers, it had not yet been demonstrated to occur from broadband sensitization originating from a semiconducting material until 2017 when Yb^{3+}:$CsPbCl_3$ was shown to have a host-sensitized photoluminescent quantum yield (PLQY)

over 100%. The sensitization of this quantum cutting process is proposed to be facilitated by a defect formed upon doping in which two Yb^{3+} substitute with lattice Pb^{2+} adjacent to a charge-compensating Pb^{2+} vacancy. This defect motif results in a shallow, observable, state that rapidly localizes photoexcitation energy and cooperatively excites the two adjacent Yb^{3+} luminophores. Upon anion exchange to from the large bandgap chloride to the smaller bandgap bromide, the high quantum yields are maintained until the bandgap is smaller than twice the energy of the $^2F_{7/2} \rightarrow {}^2F_{5/2}$ transition, the energy threshold at which quantum cutting is energetically possible. Further reduction of the bandgap precipitously decreases the Yb^{3+} PLQY to nearly 0% verifying the proposed cooperative excitation scheme. This process occurs in the same manner irrespective of the surface area-to-volume ratio of the host $CsPbX_3$ (X = Cl, Cl/Br) material implicating its potential use in bulk morphologies as optically-coupled layers for solar spectral shifting on solar cells and in nano morphologies as phosphors in solar concentrators.

Table of Contents

Table of Figures

Chapter 1 Quantum Cutting in Yb^{3+}-Doped Cesium Lead Halide Perovskites

1.1 Introduction & Motivation

Recent advances in the preparation of lanthanide (Ln^{3+})-doped $CsPb(Cl_{1-x}Br_x)_3$ have spurred a new and exciting field exploring the photophysics that result in the perovskite host and lanthanide dopant. The trivalent lanthanide (Ln^{3+}) family is a family of phosphors that have unique optical properties governed by their valence 4*f* orbitals. These orbitals are highly contracted and experience shielding from the filled 5*s* and 5*p* orbitals which cause the energetic placement of the 4*f* state electronic configurations to be determined by coulombic interactions and spin orbit coupling significantly more than ligand field strength and coordination environment. As a result, Ln^{3+} 4*f* electronic structure is nearly the same between coordination in a crystalline lattice and as a free ion. These *f* electronic states for each lanthanide have been arranged into a succinct diagram known as the Dieke Diagram.[1] Excitation into excited state *f* states can constitute a significant challenge owing to parity forbidden nature of the *f-f* transitions. Thus, oscillator strengths of *f-f* transitions are generally on the order of 10^{-6}.[2-4] This requires high-powered direct excitation at a specific wavelength for *f-f* excitation. However, a sensitizer with a broad absorption range and/or large absorption coefficient (e.g. a molecular dye) along with a well-matched electronic transition with sufficient spectral overalap to the lanthanide absorption can be used to drive energy transfer (via FRET) to excited *f* states.

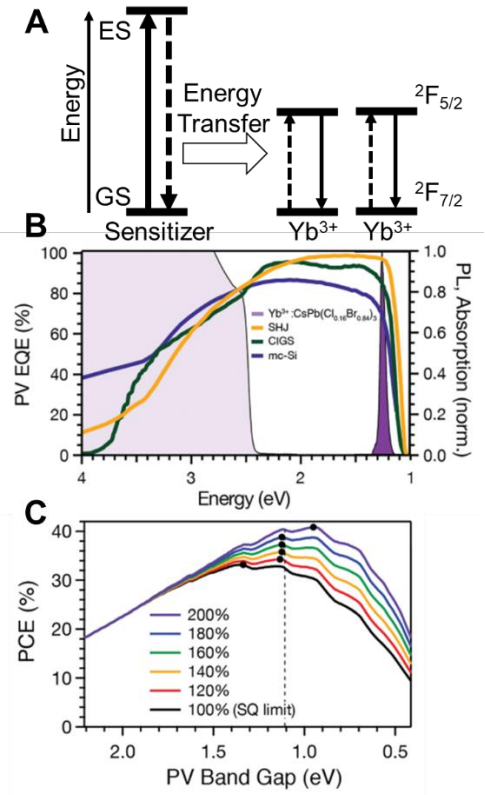

Figure 1.1 Sensitized Quantum Cutting via Yb^{3+} and Benefit for Solar Energy Harvesting.

(**A**) Generalized quantum cutting scheme showing the excitation of two Yb^{3+} activators via energy transfer from the excited state of the sensitizer. (**B**) External quantum efficiency curves of CIGS, silicon heterojunction, and monocrystalline silicon solar cells shown with Yb^{3+} emission and sensitizer $CsPbX_3$ (X = Cl/Br) host absorption. (**C**) Expected power conversion efficiencies from the detailed balance analysis with respect to the PV bandgap with quantum cutting from Yb^{3+}. The dotted black line is the band gap of silicon. Panels B and C are reprinted with permission from ref. 9. Copyright 2019 The Royal Society of Chemistry.

The most well-known *f-f* transition of the Ln^{3+} family is the $^2F_{5/2} \rightarrow {}^2F_{7/2}$ transition of Yb^{3+}. As a result of it being the only *f-f* transition of Yb^{3+}, excitation into this state will result in an emitted photon from this transition with high fidelity. Furthermore, Yb^{3+} has been demonstrated to participate in a unique photophysical phenomenon called quantum cutting (QC) in which the absorption of a high energy photon yields more than one emitted photon.[5-7] A generalized scheme of this process is shown in **Figure 1.1A**. The energy of the *f-f* transition ($E_{f\text{-}f}$) is centered at approximately 1.25 eV making it a near-infrared (NIR) transition. This energy is well-matched to the 1.12 eV bandgap of crystalline silicon (c-Si). Concordantly, its solar-sensitized emission is

highly desirable for spectral shifting in photovoltaic (PV) application.[1] **Figure 1.1B** shows the emission of Yb^{3+} overlayed with the external quantum efficiency of different PV materials with respect to energy. Photons delivered to the PV at this energy yield the greatest probability are energy harvesting. The beneficial effect of this process that can be realized is shown in **Figure 1.1C** in which the recalculated detailed balance of equations, shown as theoretical power conversion efficiency (PCE), is plotted using PVs utilizing QC Yb^{3+} with respect to the PV band gap energy and QC efficiency. As the QC process becomes more efficient, the theoretical maximum efficiency not only increases from the Shockley-Queisser limit of ~33% to ~40% but the bandgap energy at the maximum efficiency also closely aligns with the bandgap energy of silicon.[8-9] The primary benefit motivating this research is that a technology like this makes Si solar cells, the most commercially available and used PV technology, competitive with the most efficient, but costly, commercial technologies in tandem and multijunction solar cells. A high level overview of the origin of broad-band sensitized quantum cutting in Yb^{3+}:$CsPb(Cl_{1-x}Br_x)_3$ and the progress made towards devices that utilize this phenomenon is provided.

1.2 Sensitization of Quantum Cutting Yb^{3+}

1.2.1 Host Materials & Efficiency

Early attempts to sensitize Yb^{3+} using a sensitizer with a broad absorption cross section include Yb^{3+}, Pr^{3+}:$NaYF_4$ microcrystals with coumarin dyes, Yb^{3+}:CdSe, and Yb^{3+}:$Na(In_{1-x}Pb_x)S_2$.[10-12] However, the PLQYs were still lower than what could be impactful for device application.

In 2017 and 2018, Song and coworkers reported Yb^{3+}, Ce^{3+}:$CsPbCl_{1.5}Br_{1.5}$ and Yb^{3+}:$CsPbCl_3$ nanocrystals (NCs) which yielded 119% and 120% Yb^{3+} PLQY, respectively. These outstanding quantum yields were shown to be sensitized by broadband absorption from the host perovskite lattice using photoluminescence excitation (PLE) spectroscopy. Quantum yields above 100% are a signature of the unique QC process. $CsPbX_3$ (X = Cl, Br) NCs are an ideal host for Ln^{3+} owing to their large absorption cross section, facile bandgap tunability, defect tolerance, and octahedral coordination at the dopant site.[13] Of further note is the fact that Yb^{3+} is aliovalent in the Pb^{2+} sites of which it is proposed to be substituting into. This was among the first reports of aliovalent doping in lead halide perovskite nanocrystals. Representative absorption and PL of Yb^{3+}:$CsPbX_3$ (X = Cl/Br) is shown in **Figure 1.1B**.

Table 1.1. Quantum cutting Yb^{3+}-doped perovskite materials sorted by publication date.

Material	Morphology	Yb^{3+} PLQY	Reference
Yb^{3+}, Ce^{3+}:$CsPbCl_{1.5}Br_{1.5}$	Nanocrystals	119%	Song[14]
Yb^{3+}:$CsPbCl_3$	Nanocrystals	143%	Song[15]
Yb^{3+}:$CsPbCl_3$	Nanocrystals	170%	Gamelin[16]
Yb^{3+}:$CsPb(Cl_{0.35}Br_{0.65})_3$	Solution-Deposited Films	193%	Gamelin[17]
Yb^{3+}:$CsPbCl_3$	Nanocrystals	120%	Yu[18]
Yb^{3+}:$CsPbCl_3$	Nanocrystals	130%	Gamelin[19]
Yb^{3+}:$CsPb(Cl_{0.5}Br_{0.5})_3$	Thermally-evaporated Thin Films	183%	Gamelin[20]
Yb^{3+}:$CsPbCl_3$	Nanocrystals	175%	Gamelin[21]
Yb^{3+}:$CsPbCl_3$	Nanocrystals	164%	Wu[22]
Yb^{3+}:$CsPb(Cl_{1-x}Br_x)_3$	Nanocrystals	~200%	Gamelin[23]
Yb^{3+}, Pr^{3+}, Ce^{3+}:$CsPbClBr_2$	Nanocrystals	160%	Song[24]
Yb^{3+}, Mn^{2+}:$CsPbCl_3$	Nanocrystals	103%	Chen[25]
Cr^{3+}, Yb^{3+}, Ce^{3+}:$CsPbCl_3$	Nanocrystals	175%	Song[26]
Yb^{3+}:$CsPbCl_3$	Layered Films	130%	Miyaska[27]
Yb^{3+}:$CsPbCl_3$	Nanocrystals	150%	Hens[28]
Yb^{3+}, Er^{3+}:$CsPb(Cl_{0.6}Br_{0.4})_3$	Nanocrystals	129%	Mao[29]
Yb^{3+}, Er^{3+}:$CsPb(Cl_{0.6}Br_{0.4})_3$	Nanocrystals	129%	Mao[29]
Yb^{3+}:$CsPbCl_3$	Nanocrystals	110%	Li, Chen, Chen[30]
Yb^{3+}:$CsPbCl_3$	Nanocrystals	127%	Zhu[31]
Yb^{3+}:$CsPbCl_3$	Nanocrystals	130%	Weiss[32]

Since the report of these materials, numerous works have been reported in which quantum yields over 100% have been observed. These results, and the morphologies they were synthesized in, are shown in **Table 1.1**. A significant result implicit in these observations is the fact that QC is observed in bulk morphologies beyond nanomaterials. Thus, QC in Yb^{3+}:$CsPbX_3$ is a process inherent to the material allowing for broad application in various morphologies.

1.2.2 Sensitization Schemes

The energy gap between Yb^{3+} emission, centered at 1.26 eV (980 nm), and the host $CsPbCl_3$ emission, centered at 3.05 eV (410 nm) in NCs, is substantial. In order to maintain Yb^{3+} quantum cutting, the bandgap of the host must be larger than twice the $^2F_{7/2} \rightarrow {}^2F_{5/2}$ absorption ($2xE_{f\text{-}f}$). Thus, the bandgap of the host material must be > 2.5 eV (490 nm), the quantum cutting energy threshold (QCET). Sensitization is proposed to occur in a variety of mechanisms. Song and coworkers have proposed a stepwise excitation mechanism, shown in **Figure 1.2A**, in which absorbed photoexcitation energy decays to a deep trap state and subsequently excites a Yb^{3+} ion through nonradiative energy transfer. Decay from the deep trap state then excites another Yb^{3+}.[15] Gamelin and coworkers have proposed a cooperative mechanism, shown in **Figure 1.2B**, in which a shallow, Yb^{3+}-induced trap state captures photoexcitation energy and excites a Yb^{3+} dimer.[16] Others have proposed a mechanism involving a transient redox reaction in which a Yb^{3+}-induced electron trap state facilitates a charge transfer to Yb^{3+} reducing it to Yb^{2+} and subsequent oxidation allows for excitation of a coupled Yb^{3+} dimer. This process is shown schematically in **Figure 1.2C**.[28] The CT band of Yb^{3+}-Cl^- is >3.5 eV making excitation from induced trap to CT impossible without the energy of a second photon and dark process limiting its PLQY to 100% in the most ideal scenarios.[21, 33-35] A variety of other mechanisms involving other co-doped lanthanides with Yb^{3+} have been proposed.[14, 24] However, QC is observed with solely Yb^{3+}-doped materials implying sensitization of Yb^{3+} occurs by a scheme outlined in **Figure 1.2**.

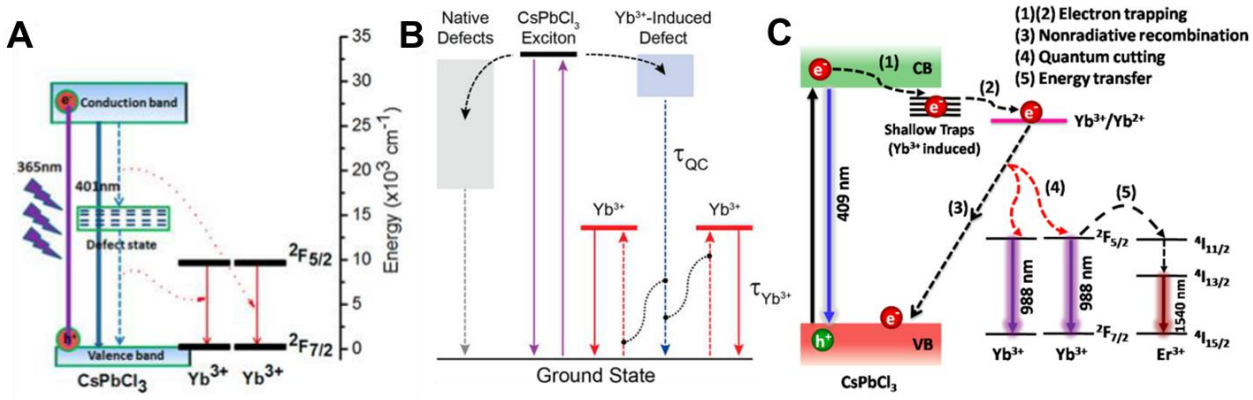

Figure 1.2 Proposed Quantum Cutting Sensitization Schemes.

(**A**) Step-wise excitation utilizing a native, deep trap in the perovskite electronic structure. Reprinted with permission from ref. 15. Copyright 2018 American Chemical Society. (**B**) Cooperative excitation of two Yb^{3+} directly from a shallow trap in the perovskite. Reprinted from ref. 16. Copyright 2018 American Chemical Society. (**C**) Cooperative excitation of two Yb^{3+} utilizing a shallow defect state in the perovskite host facilitating a charge transfer to reduce Yb^{3+} to Yb^{2+} followed by cooperative excitation of two Yb^{3+}. Reprinted with permission from ref. 28. Copyright 2020 American Chemical Society.

1.2.3 Shallow Defect State

Spectroscopic signatures of a state involved in sensitizing Yb^{3+} PL have been reported. One way to probe the existence and location of an Ln^{3+}-induced state in the host perovskite is to dope the material with a chemically similar, but spectroscopically-innocent, dopant. This type of dopant lacks interfering excited state transitions. In Watanabe *et al*. La^{3+} serves as the spectroscopically-innocent dopant in $CsPbCl_3$ single crystals. At cryogenic temperatures, a shallow and broad induced state forms in the doped sample but not in the undoped $CsPbCl_3$. However, above 80 K the doped and undoped samples are virtually identical.[36] The induced, near-band-edge (NBE) emission is recreated in nanocrystals of La^{3+}:$CsPbCl_3$ as shown in **Figure 1.3A**.[16] In both cases these data suggest that Ln^{3+} doping induces a shallow trap state consistent with the mechanism outlined in **Figure 1.2A**. The same effect is observed using other innocent RE^{3+} dopants such as Y^{3+}, La^{3+}, Gd^{3+}, and Lu^{3+} in the bromide which is shown in **Figure 1.3B**. The same induced state manifests in the chloride as well.[37] DFT calculations on Yb^{3+}:$CsPbCl_3$ provide further confirmation that the induced defect is shallow and sensitization occurs via the cooperative excitation mechanism in **Figure 1.2B**.[37]

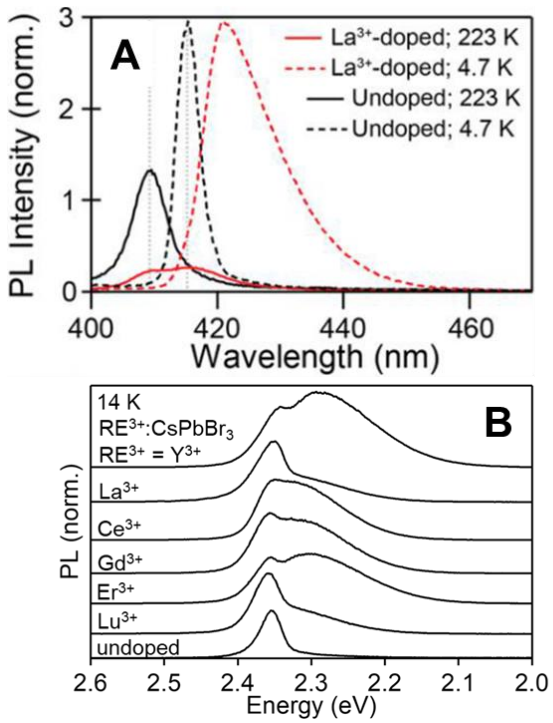

Figure 1.3 Shallow, Dopant-Induced Defect PL

(**A**) Low temperature PL of $CsPbCl_3$ and La^{3+}:$CsPbCl_3$ NCs. Reprinted with permission from ref. 16. Copyright 2018 American Chemical Society. (**B**) Low temperature PL of $CsPbBr_3$ and RE^{3+}:$CsPbBr_3$ NCs (RE = Y, La, Ce, Gd, Er, Lu). Reprinted with permission from ref. 37. Copyright 2022 American Chemical Society.

Another striking piece of data that confirms the existence of a shallow defect being necessary for sensitization (i.e. being a cooperative excitation mechanism) is the anion exchange of these materials to decrease the bandgap while monitoring the Yb^{3+} emission with respect to the bandgap energy. Halide alloying is a well-known method to predictably tune the bandgap between the blue and red ends of the visible spectrum.[38-41] **Figure 1.4A** shows the systematic change in the absorption and photoluminescence of Yb^{3+}:$CsPb(Cl_{1-x}Br_x)_3$ NCs during anion exchange from the large gap chloride to the smaller gap bromide. *In-situ* monitoring of the Yb^{3+} emission at a constant excitation rate of the host lattice yields a constant Yb^{3+} PLQY above 100% until the bandgap reaches the QCET (485 nm, ~2.55 eV) at which point the Yb^{3+} emission rapidly drops off to nearly 0 in the full bromide. Furthermore, anion exchanging back to the chloride yields a quantum yield nearly 200%, the thermodynamic limit of the quantum cutting process in this material.[23] **Figure 1.4B** plots the Yb^{3+} quantum yield as a function of the bandgap during the chloride-to-bromide

and subsequent bromide-to-chloride anion exchange reactions. If the stepwise sensitization mechanism, **Figure 1.2A**, were the primary mechanism then the Yb^{3+} emission should not be expected to go to nearly zero unless the state after anion exchange is no longer present. However, after going back to the larger gap chloride the recovery of the Yb^{3+} PLQY shows the state remains during the anion exchange. Further observation of this state remaining during anion exchange is shown in **Figure 1.4C** in which spectroscopically innocent Gd^{3+} is doped into the chloride and subsequently anion exchanged to a mixed chloride/bromide and full bromide. At low temperature, the defect state is maintained at nearly the same energy below the band edge at all the compositions probed meaning the anion exchange does not perturb the nature of the dopant-induced state. As a result of the electronic structure of the host perovskite being antibonding Pb^{2+} 6s – X^- np in the valence band and non-bonding Pb^{2+} 6p in the conduction band, halide anion exchange primarily shifts the valence band. Thus, the nature of the defect state must be an electron trap shallow to the conduction band.

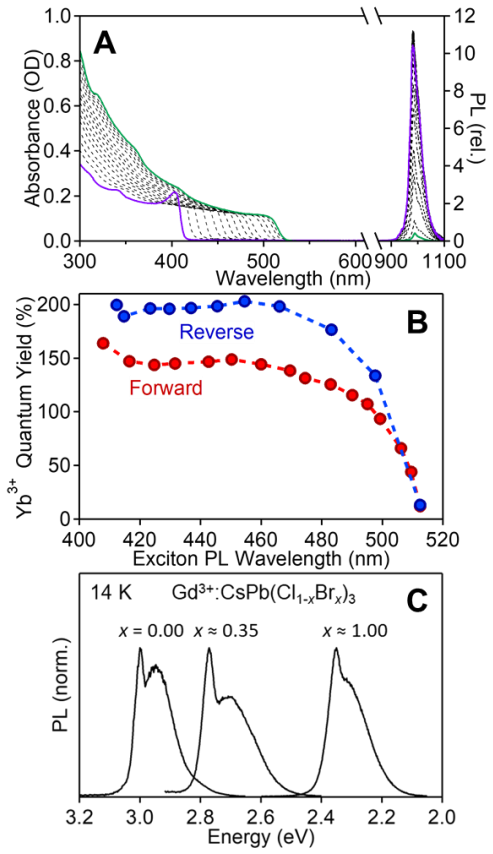

Figure 1.4 Chloride-to-Bromide Anion Exchange in Ln^{3+}:$CsPb(Cl_{1-x}Br_x)_3$ NCs.

(**A**) Absorption and PL spectra monitored *in-situ* after adding TMS-Br to Yb^{3+}:$CsPb(Cl_{1-x}Br_x)_3$ nanocrystals. Adapted with permission from ref. 23. Copyright 2019 American Chemical Society. (**B**) Yb^{3+} quantum yield as a function of the host bandgap for a representative reaction from panel A. Reprinted with permission from ref. 23. Copyright 2019 American Chemical Society. (**C**) 14 K CW spectra of 8% Gd^{3+}:$CsPb(Cl_{1-x}Br_x)_3$ NCs varying *x*. Reprinted with permission from ref. 37. Copyright 2022 American Chemical Society.

1.2.4 Charge Compensating Defect Motif

Given the octahedral coordination of the Pb^{2+} ion in $CsPbX_3$, Ln^{3+} most likely substitute for Pb^{2+}. X-ray characterization of the coordination of Yb^{3+} confirm this.[42] Thus, Ln^{3+} acts as an aliovalent dopant in the lead halide perovskites. To maintain charge neutrality, the excess charge must be compensated. In similar systems such as Gd^{3+}:$CsCdBr_3$ and Gd^{3+}:$CsMgX_3$ (X = Cl, Br) it has been reported by McPherson and coworkers that the predominant doping motif is the cooperative doping of two Ln^{3+} coupled with a charge-balancing M^{2+} vacancy ($V_{M(II)}$) between the dopants. This conclusion was established using EPR spectroscopy.[43-44] The doping motif of Gd^{3+}:$CsCdBr_3$ is shown in **Figure 1.5A**. Despite some minor dissimilarities between the crystal structures, a similar doping motif is assumed to happen in the lead halide perovskites. In this scenario, a pair of Ln^{3+} dopants cooperatively substitute in Pb^{2+} sites with an adjacent V_{Pb}. It was also found that the doping concentration of Yb^{3+} was generally correlated with the amount of Cs^+ added ruling out the possibility of V_{Cs} cooperatively doping with Yb^{3+} as a primary defect motif.[16] While structural characterization using x-ray spectroscopy is still lacking, calculations probing various defect formation energies in perovskite materials have been reported. **Figure 1.5B** shows the resulting energy level from specific defects in $CsPbBr_3$ from first-principles calculations. It is known that the formation energy of the vacancy defects have the lowest formation energy of the numerous point defects that can form in perovskite materials. The V_{Pb} defect is expected to manifest within ~0.2 eV of the valence band.[45-49] Li *et al*. studies the electronic structure and formation energies of specific types of Yb^{3+}-V_{Pb}-Yb^{3+} motifs and also find similarly low formation energies of V_{Pb} pinning the induced state near the band gap. This leads to the conclusion that Yb^{3+} sensitization happens primarily via the cooperative mechanism.[37]

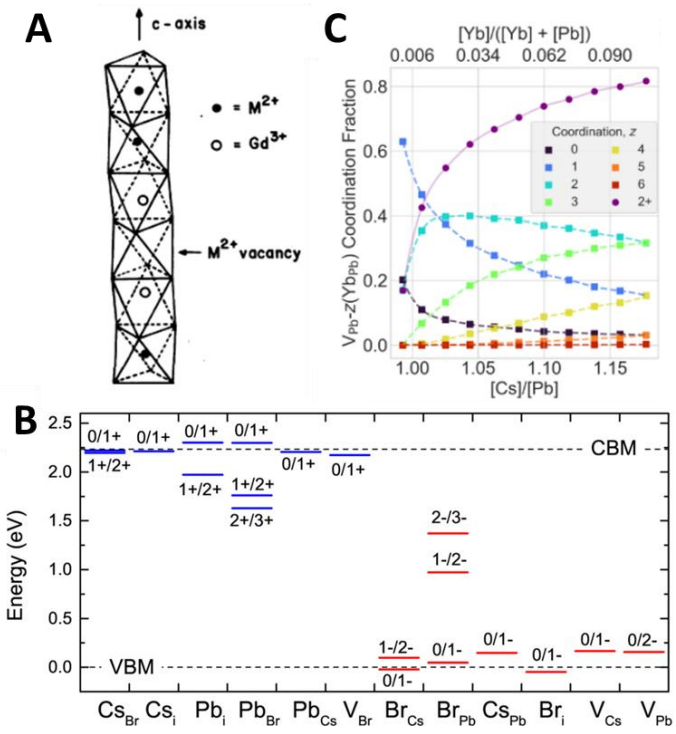

Figure 1.5 Induced Defect Motif.

(**A**) The "McPherson Pair" motif demonstrated using Gd^{3+}:$CsCdBr_3$. A charge-compensating Cd^{2+} vacancy (V_{Cd}) is always found between two neighboring Gd^{3+} dopants. Reprinted with permission from ref. 44. Copyright 1977 American Physical Society. (**B**) Energy level diagrams detailing specific induced states from various structural defects in $CsPbBr_3$. Reprinted with permission from ref. 48. Copyright 2017 American Chemical Society. (**C**) Probability distribution of various Yb^{3+} doping motifs involving V_{Pb} with respect to the doping concentration of (top) Yb^{3+} and the (bottom) [Cs]:[Pb] ratio. Reprinted with permission from ref. 51. Copyright 2022 American Physical Society.

Figure 1.5C describes the distribution of nearest cation neighbor Yb^{3+} with respect to an induced V_{Pb} in geometrically-optimized Yb^{3+}:$CsPbCl_3$ using Monte Carlo simulations. The probabilities of being found in different doping motifs involving one or two Yb^{3+} substituting for Pb^{2+} with a V_{Pb} is plotted with respect to the Yb^{3+} doping concentration. The probability of forming isolated Yb^{3+} rapidly decreases as the doping level increases while the probability of finding Yb^{3+} in a dissociated dimer (one Yb^{3+} is not next nearest cation neighbor, nnn, to V_{Pb} but is still within the 10 Å bohr radius of dexter type energy transfer) or local dimer (both Yb^{3+} is nn to V_{Pb}) increase. At relevant doping concentrations, >6% Yb^{3+}, there is >90% probability of finding Yb^{3+} in any

sort of dimer, dissociated or local. Thus, the proposed Yb^{3+}-V_{Pb}-Yb^{3+} motif forming the observed shallow defect state is a plausible hypothesis for the sensitization of Yb^{3+}.

1.3 Exciton to Defect to Ytterbium Dynamics

The nature of this induced state has resulted in the outstanding quantum yields observed for Yb^{3+} sensitized luminescence. For one, quantum yields in the chlorides are often times limited to ~20% for excitonic emission due to efficient trapping to native defects such as dangling bonds. In $CsPbBr_3$, hot carrier trapping in native or intentionally added hot carrier traps occurs on a picosecond timescale.[50] Ergo, to observe quantum cutting with the efficiencies reported in **Table 1.1**, trapping to the dopant-induced defect state must happen on a time scale competitive with 1-10 ps. Equation 1.1 can be used to extract an approximate value for the rate constant of energy transfer from the exciton to the induced state, k_{ET}, needed to yield 200% quantum yields.

$$\Phi_{NIR} = \Phi_{ET} * \Phi_{QC} * (2 * \Phi_{Yb}) = \frac{nk_{ET}}{nk_{ET}+k_{nr}+k_{exciton}} * \Phi_{QC} * (2 * \Phi_{Yb}) \qquad (1.1)$$

$\Phi_{NIR}, \Phi_{ET}, \Phi_{QC}, \Phi_{Yb}$ represent the quantum efficiencies of the observed NIR PL, exciton-to-induced-defect energy transfer, defect-to-Yb^{3+} energy transfer, and the internal quantum efficiency of a single Yb^{3+} phosphor, respectively. k_{ET}, k_{nr}, and $k_{exciton}$ represent the rate constants for exciton-to-defect energy transfer, non-radiative decay, and exciton radiative decay, respectively. Assuming 100% PLQY after energy transfer from the exciton, 200% observed PLQY in the NIR, $k_{nr} = 1x10^{12}$ s^{-1}, and $k_{exciton} = 1x10^{9}$ s^{-1} as approximate rate constants, Φ_{NIR} is shown as a function of varying k_{ET} in **Figure 1.6A**. To observe quantum yields above 100% from the NIR, k_{ET} must be at on the order of at least $1x10^{12}$ s^{-1} or greater (i.e. faster than 1 ps). The assumption that Φ_{QC} is unity is validated by Milstein *et al*. in which no shallow defect emission is observed at any temperature (13 to 296 K) in Yb^{3+}:$CsPbCl_3$ NCs indicating energy transfer rate from the induced defect state to the adjacent Yb^{3+} is much greater than the radiative rate.[16] Φ_{Yb} is assumed to be unity due to its monoexponential decay.[16, 33] Despite the fast energy transfer on the order of 100s fs, excitonic emission is still observed which was attributed to be the result of a small *n* in eq. 1.1.[16]

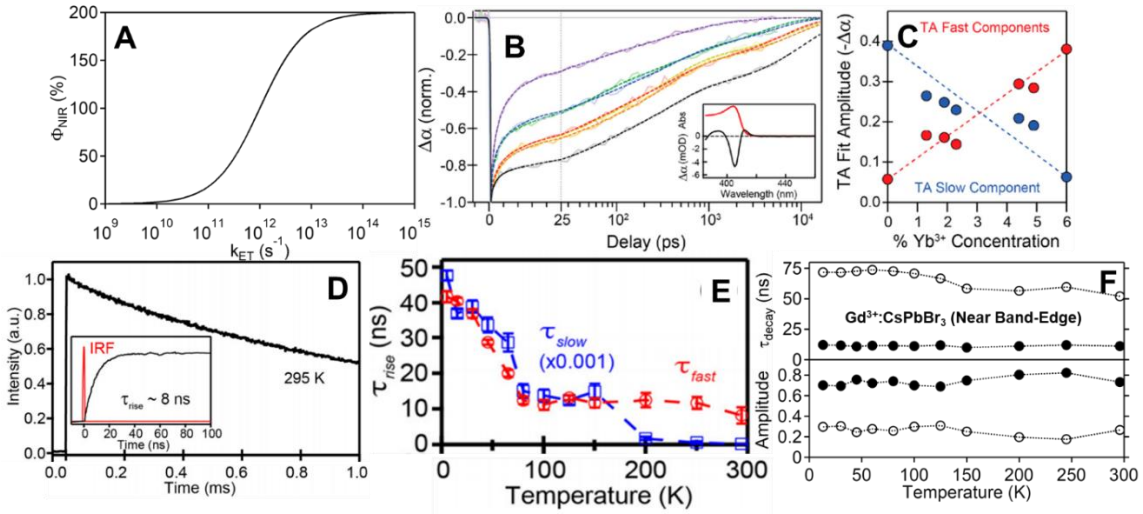

Figure 1.6 Exciton, Yb^{3+}, and NBE Dynamics.

(**A**) Effect of k_{ET} on the observed NIR PLQY, Φ_{NIR}, of Yb^{3+}:$CsPbCl_3$. (**B**) TA bleach recovery dynamics with fits of the exciton of Yb^{3+}:$CsPb_{1-x}Cl_3$. Black: undoped, red to purple: 1.3% to 6.0% Yb^{3+}. (**C**) Scatterplot showing the average amplitude of the time constants as a function of the doping concentration. Red: 300 fs, 2.0 ps, and 8.4 ps; Blue: slowest component (~5 ns). Panels B and C are reprinted from ref 16. Copyright 2018 American Chemical Society. (**D**) Temperature-dependent Yb^{3+} PL rise times and (**E**) scatterplot showing the rise times with respect to temperature. Panels D and E are reprinted with permission from ref. 33. Copyright 2020 American Physical Society. (**F**) Scatterplot showing the decay lifetimes and amplitudes from the induced, near band-edge state in Gd^{3+}:$CsPbBr_3$ NCs (filled: fast component; open: slow component). Reprinted with permission from ref. 37. Copyright 2022 American Chemical Society.

This observation is observed in the ultrafast transient absorption (TA) data of Yb^{3+}:$CsPbCl_3$ nanocrystals, shown in **Figure 1.6B**. These data show Yb^{3+}-induced depopulation of the exciton state occurs with an instrument-limited lifetime of ~300 fs. Other time constants of 2.0 and 8.4 ps are also observed. The average amplitude of these time constants, shown in **Figure 1.6C**, is observed to increase in amplitude as the concentration of Yb^{3+} is increased in the lattice.[16] The amplitude of the 300 ps time component matches the same trend as the steady-state branching ratio of the Yb^{3+} PL. Thus, nonradiative energy transfer to the induced defect state occurs at a rate commensurate to the trapping rate inherent to the host perovskite which yields the efficient systems reported; this process is exacerbated by Yb^{3+} doping.

At all temperatures, the Yb^{3+}-induced defect emission is not observed making it difficult to probe directly probe the state.[16] However, in conjunction with the TA data, rise time of the Yb^{3+}

emission and doping with spectroscopically innocent dopants can provide an indirect way to understand the defect. **Figures 1.6D-6E** show the temperature-dependent rise times for Yb^{3+}:$CsPbCl_3$ NCs reported in Roh *et al*. The emission rise times are as long as 40 ns at 5 K and 10 ns at 296 K. Similar results are also reported for Bridgmann-grown single crystals.[33] Given the disparity in time between ~300 fs depopulation of the exciton and 10 ns for Yb^{3+} excitation, there must be an intermediate state in the sensitization of Yb^{3+}. **Figure 1.6F** shows the time-resolved decay times and amplitudes from biexponential fitting from the induced defect state in Gd^{3+}:$CsPbBr_3$ at various temperatures from 14 to 296 K. Interestingly, it is observed to be on the order of 10 ns through the entire temperature range. This would agree well with the results from Roh *et al*. Since this state is not observed in Yb^{3+}-doped samples at any temperature, it implies that this state can transfer energy to Yb^{3+} with high fidelity, considering PLQYs of doped samples approach the thermodynamic limit in many samples.

1.4 Solar Applications Involving Yb^{3+}

1.4.1 Optically-Coupled QC Layer on Si PVs

The most efficient PV technologies available are tandem and multi-junction solar cells which utilize materials with progressively larger bandgaps stacked on top allowing the voltages to add in series. This reduces thermalization losses and has resulted in efficiencies above 30% making them the most efficient devices available.[51-52] However, due to the long fabrication process requiring high purity epitaxial crystal growth and multiple charge extraction/surface passivation layers, these devices come at a significant cost of approximately $4-5/W which is an order of magnitude more expensive than energy from Si solar cells.[51]

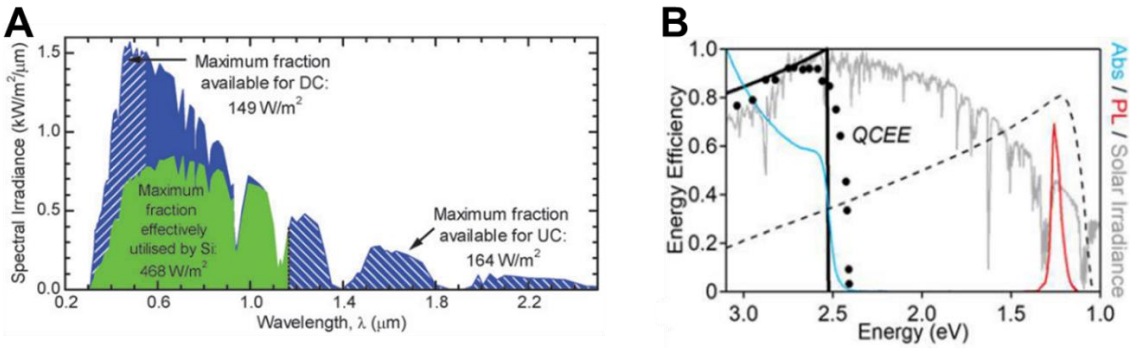

Figure 1.7 Solar Energy Harvesting and Quantum Cutting Energy Efficiency

(**A**) Solar spectral irradiance showing the fraction of the energy available to Si PVs (green) overlayed with the fraction of solar energy available to Si PVs utilizing

spectral shifting. Reprinted with permission from ref. 57. Copyright 2006 Elsevier. (**B**) Energy efficiency of c-Si solar cells and the quantum cutting phenomenon (left) overlayed with the Yb^{3+}:$CsPb(Cl_{0.25}Br_{0.75})_3$ absorption/PL, and AM1.5 solar spectrum (right). (solid black: theoretical QCEE; circles: experimentally-derived QCEE from anion exchange; dashed black: theoretical c-Si PV energy efficiency). Reprinted from ref. 23. Copyright 2019 American Chemical Society.

A simpler method for higher efficiency PV devices is to use solar spectral shifting, namely quantum cutting. The excess of energy from the high energy end of the visible spectrum is available for quantum cutting to the NIR bandgap of Si and CIGS.[1, 8, 12, 53-54] **Figure 1.7A** shows the solar irradiance with respect wavelength for what is available to Si PVs and Si PVs that utilize spectral shifting. Upconsverion is another way to uptake more solar energy but is beyond the scope of this chapter. In an ideal scenario, an extra ~25% of solar irradiance could be harnessed by Si PVs using downconversion technology.[55] The favorable energetic matching of the $^2F_{5/2} \rightarrow {}^2F_{7/2}$ transition of Yb^{3+} with the bandgap of c-Si (**Figure 1.1B**) makes it the ideal candidate as a phosphor in this process.[1, 54] The energy efficiency of c-Si solar cells overlayed with the solar spectrum (AM1.5G) and Yb^{3+}:$CsPb(Cl_{0.75}Br_{0.25})_3$ absorption, PL, and quantum cutting energy efficiency is shown in **Figure 1.7B**. The energy efficiency, η_{eff}, is defined as

$$\eta_{eff} = \frac{E_g}{E_{incident}} \tag{1.2}$$

in which $E_{incident}$ is the energy of an incident photon and E_g is the bandgap of the material. As the energy of the incident photon increases, more of the energy is lost as thermalization. Thus, to avoid significant energy loss, quantum cutting from the high energy regime of the solar spectrum is a way to optimize the energy being harvested. The quantum cutting energy efficiency (QCEE) is

$$\eta_{QCEE} = \frac{E_{PL}}{E_{abs}} \Phi_{\mathrm{NIR}} \tag{1.3}$$

in which E_{PL} is the PL energy of Yb^{3+} and E_{abs} is the band gap of the host perovskite. The quantum efficiency of Yb^{3+} is assumed to be 100%. The QCEE maximizes when the bandgap of the host $CsPb(Cl_{1-x}Br_x)_3$ is $2xE_{f\text{-}f}$ in which $x \approx 0.75$.

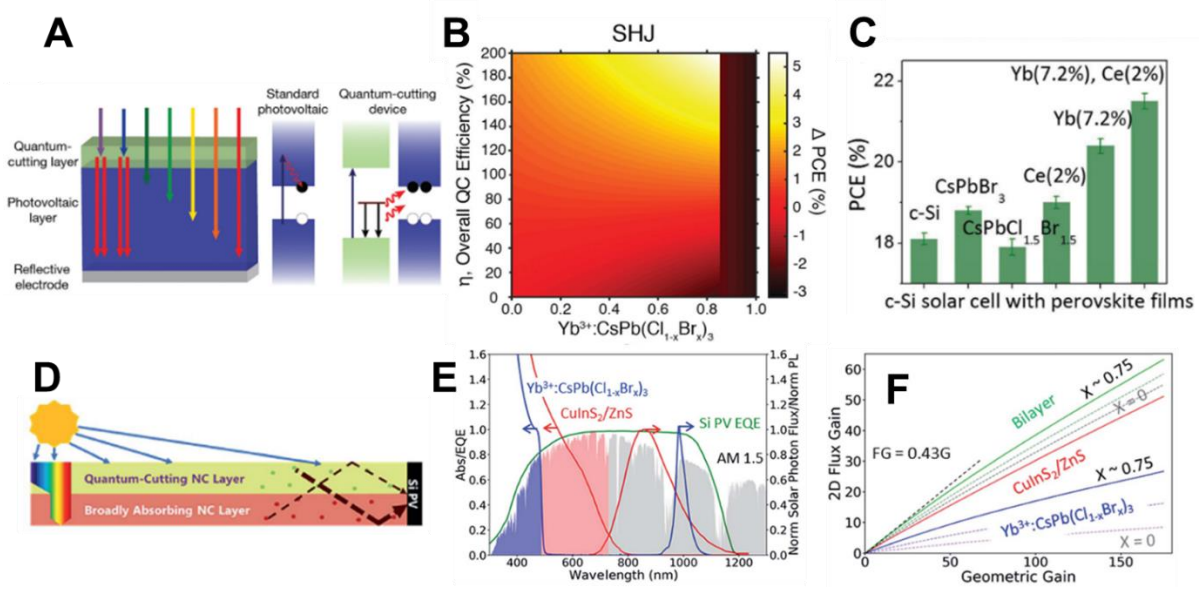

Figure 1.8 Applications of Quantum Cutting Perovskites

(**A**) Diagram of an optically-coupled QC layer deposited directly onto a PV device. In standard photovoltaics, one absorbed photon results in one photogenerated electron-hole pair than can be extracted. In a quantum cutting device, one high-energy absorbed photon results in two photogenerated electron-hole pairs that can be extracted. (**B**) Theoretical change in the power conversion efficiency (PCE) of a silicon heterojunction cell (SHJ) with respect to Φ_{NIR} as a function of the increasing bromide content (decreasing band gap) of the host perovskite. Panels A and B are reprinted with permission from ref. 9. Copyright 2019 The Royal Society of Chemistry. (**C**) Measured PCEs of c-Si solar cells with different variations of $CsPb_{1-a-b}Yb_aCe_b(Cl_{1-x}Br_x)_3$ NCs deposited on the surface. Reprinted with permission with ref. 14. Copyright 2017 Wiley. (**D**) Monolithic bilayer LSC with a QC perovskite and broadly absorbing layer underneath. (**E**) Absorption and PL of Yb^{3+}:$CsPb(Cl_{1-x}Br_x)_3$ and $CuInS_2$/ZnS NC phosphors overlayed with Si PV EQE and the AM1.5 solar spectrum. (**F**) Bilayer LSC device modeling of the theoretical maximum flux gain relative to x (bromide alloying content) and the geometric gain. Panels D-F are reprinted with permission from ref.19. Copyright 2019 The Royal Society of Chemistry.

The results of **Table 1.1** show that Yb^{3+} sensitization also occurs in bulk morphologies. Solution-deposited films, flash-sublimated thin films, and single crystals have all been observed to sensitize Yb^{3+}.[17, 20, 27, 33, 56] The flash-sublimated thin films provide the greatest utility for solar applications owing to their remarkable optical quality and uniformity after deposition. In Crane *et al*. the authors demonstrate the ability to flash sublimate quantum cutting Yb^{3+}:$CsPb(Cl_{1-x}Br_x)_3$ thin films on to glass substrate and achieve optical densities as high as 2 with negligible sub-band-

gap scattering.[20] Recalculating the detailed balance for the efficiency of specific solar cells, it is found that PCE boosts in silicon heterojunction (SHJs) and CIGS PVs can go beyond a 5% increase from the uncoated PVs in the most ideal scenario with Yb^{3+}:$CsPb(Cl_{0.25}Br_{0.75})_3$. Even 100% PLQY can yield a ~2% gain in efficiency. **Figure 1.8B** plots these theoretical efficiency boost of a SHJ solar cell with respect to the perovskite bromide content (ie. the bandgap), x, and the QC PLQY. Other significant advantages when coupling the QC perovskite with a silicon PV occur: 1) The ability to texture both ends of the PV allowing for greater probability of photon absorption, 2) Using silicon heterojunction cells which are optimized for NIR absorption, and 3) simple, low-cost design. In tandem cells, the high cost of the materials came from the crystal growth steps and reagent costs.[51] Meanwhile, fabrication of Si-based PVs are commercially standardized and have the ability to be printed at significant rates with low cost (<\$0.50 W^{-1}).[57]

Deposition of a QC Yb^{3+}:$CsPb(Cl_{1-x}Br_x)_3$ layer on small PV modules has been reported to yield a PCE gain upwards of 3.5%.[14, 24] **Figure 1.8C** shows the appreciable gain in EQE from Si PV modules before and after a QC layer of $Cs(Pb_{1-a-b}Yb_aCe_b)(Cl_{1-x}Br_x)_3$ is deposited on the surface through a simple solvent evaporation method. Furthermore, Song and coworkers show the EQE curves of the PVs exhibit an increase in efficiency at wavelengths of irradiation corresponding to the absorption the perovskite.[14, 24] While these results are an encouraging start, further improvement of the deposition technique and optical coupling are required to get optimal performance.

1.4.2 Luminescent Solar Concentrators (LSCs)

LSCs are an exciting next-generation technology that utilize a phosphor (i.e. molecular dye or nanocrystals) with a large Stokes Shift embedded in a transparent polymer matrix to capture solar energy. Emitted light is waveguided to solar cells lining the edges and are used to generate a current.[58] Yb^{3+}:$CsPb(Cl_{1-x}Br_x)_3$ ($x \leq 0.75$) is an ideal candidate due to the high quantum yields and zero reabsorption loss. The authors of Luo *et al.* design a small scale 25 cm^2 LSC embedded with an internal quantum efficiency of 118% and external quantum efficiency (EQE) of 3.8%. Further modeling shows that with a 200% QY sample of Yb^{3+}:$CsPb(Cl_{1-x}Br_x)_3$ that absorbs >7% of solar photons could yield an EQE in excess of 10% in a 100 cm^2 device making them among the most efficient devices possible.[22, 59] The corresponding flux gain (FG), a ratio of converted photons with an LSC-PV device to a bare PV device with the same solar flux, ends up being comparable to other

reported LSCs of similar sizes.[22] However, in Cohen *et al*. the authors find that parasitic NIR absorption from C-H bonds drastically reduces the efficiency of such devices, and a polymer matrix without C-H bonds is necessary to realize the maximum efficiency. However, options to use fluorinated polymers or a glassy matrix could suffice.[19, 60-61]

At the ideal bandgap for the highest QCEE, only 8% of all usable solar photons is being absorbed and waveguided. Having an embedded material like Yb^{3+}:$CsPb(Cl_{1-x}Br_x)_3$ NCs is ideal for LSCs that also function as windows because there is minimal visible absorption, however, the device itself yields a poor flux gain for larger sizes. In devices where solar concentration is paramount and the degree of tinting is irrelevant, a broadly absorbing material with a large stokes shift is also required. Ideally, this material would be in a separate layer below the quantum cutting layer to ensure the highest energy photons result in quantum cutting while the rest of the rest of the yield of the solar spectrum is waveguided. A monolithic bilayer LSC with Yb^{3+}:$CsPb(Cl_{1-x}Br_x)_3$ NCs as the quantum cutting layer and $CuInS_2$/ZnS NCs as the broadly absorbing layer below has been envisioned.[19] A diagram of this device is shown in **Figure 1.8D**. The absorption and PL of these materials overlayed with Si PV EQE and AM1.5 solar spectrum are shown in **Figure 1.8E**. Both these phosphors have minimal reabsorption losses and broad absorption cross sections allowing for most of the visible spectrum to be captured. The theoretical 2D flux gain of an LSC of this type with respect to the increase in its area is shown in **Figure 1.8F**. The incorporation of the broadly-absorbing layer significantly increases the amount of sunlight that can be concentrated. The overall FG of this device is 63 for a device of 70 x 70 x70 cm^3 which corresponds to a 19% enhancement of performance compared to champion $CuInS_2$ LSC technology of the same volume.[19, 62] This comes at the cost of decreased visible transmittance which may limit its widespread applicability as solar windows. However, they can function as ideal solar windows for greenhouses where the red end of the solar spectrum, most efficiently taken up by plants, is not absorbed.

1.4.3 Saturation Effects

Saturation of Yb^{3+} emission in the perovskite lattice can occur.[16-17] The behavior is due to the large absorption cross section of the perovskite and the long emission lifetime of Yb^{3+}. It is proposed that exciting the nanocrystal before the Yb^{3+} population have decayed to the ground state results in excitation to a charge transfer transition of Yb^{3+}-X^-. This effect can be negated by

accessing higher effective doping concentration regimes >6% Yb^{3+}.[21] Currently, the intensity from one sun of excitation on Yb^{3+}:$CsPb(Cl_{1-x}Br_x)_3$ would result in ~20% and ~40% loss of Yb^{3+} emission for x = 0 and 0.75, respectively.[21] Thus, the ability to overcome the saturation effect is of paramount importance for designing devices with optimal efficiency.

1.5 Outlook

The broad-band sensitization of Yb^{3+} emission via the defect motif required for charge compensation from aliovalent doping is, from a fundamental standpoint, a remarkable phenomenon. However, detailed structural characterization of the defect motif and luminescence from directly-excited Yb^{3+}-Yb^{3+} dimers are still key data sets yet to be reported. These data would provide foundational evidence in addition to what has already been reported supporting the proposed cooperative excitation mechanism. Understanding this excitation mechanism catalyzes the research from an application standpoint in the development of more efficient phosphors. The potential for broader application is what will drive further innovation for QC PV devices. Optimum optical coupling and efficient/scalable deposition techniques that are not deleterious to the NIR PLQY are all necessary engineering advancements for these devices that are required to realize the theoretical boosts in PV PCEs reported.

References

1. van der Ende, B. M.; Aarts, L.; Meijerink, A. *Phys. Chem. Chem. Phys.* **2009,** *11*, 11081-11095.
2. Hehlen, M. P.; Güdel, H. U. *J. Chem. Phys.* **1993,** *98*, 1768-1775.
3. Wenger, O. S.; Gamelin, D. R.; Güdel, H. U.; Butashin, A. V.; Kaminskii, A. A. *Phys. Rev. B* **1999,** *60*, 5312-5320.
4. Venkata Krishnaiah, K.; Rajeswari, R.; Upendra Kumar, K.; Surendra Babu, S.; Martín, I. R.; Jayasankar, C. K. *J. Quant. Spectrosc. Radiat. Transfer* **2014,** *140*, 37-47.
5. Eilers, J. J.; Biner, D.; van Wijngaarden, J. T.; Krämer, K.; Güdel, H. U.; Meijerink, A. *Appl. Phys. Lett.* **2010,** *96*, 151106.
6. Katayama, Y.; Tanabe, S. *Materials* **2010,** *3*.
7. Duan, Q.; Qin, F.; Wang, D.; Xu, W.; Cheng, J.; Zhang, Z.; Cao, W. *J Appl. Phys.* **2011,** *110*, 113503.
8. Trupke, T.; Green, M. A.; Würfel, P. *J. Appl. Phys.* **2002,** *92*, 1668-1674.
9. Crane, M. J.; Kroupa, D. M.; Gamelin, D. R. *Energy Environ. Sci.* **2019,** *12*, 2486-2495.
10. Martín-Rodríguez, R.; Geitenbeek, R.; Meijerink, A. *J. Am. Chem. Soc.* **2013,** *135*, 13668-13671.
11. Creutz, S. E.; Fainblat, R.; Kim, Y.; De Siena, M. C.; Gamelin, D. R. *J. Am. Chem. Soc.* **2017,** *139*, 11814-11824.
12. Wang, Z.; Meijerink, A. *J. Phys. Chem. Lett.* **2018,** *9*, 1522-1526.

13. Protesescu, L.; Yakunin, S.; Bodnarchuk, M. I.; Krieg, F.; Caputo, R.; Hendon, C. H.; Yang, R. X.; Walsh, A.; Kovalenko, M. V. *Nano Lett.* **2015,** *15*, 3692-3696.
14. Zhou, D.; Liu, D.; Pan, G.; Chen, X.; Li, D.; Xu, W.; Bai, X.; Song, H. *Adv. Mater.* **2017**, 1704149.
15. Pan, G.; Bai, X.; Yang, D.; Chen, X.; Jing, P.; Qu, S.; Zhang, L.; Zhou, D.; Zhu, J.; Xu, W.; Dong, B.; Song, H. *Nano Lett.* **2017,** *17*, 8005-8011.
16. Milstein, T. J.; Kroupa, D. M.; Gamelin, D. R. *Nano Lett.* **2018,** *18*, 3792-3799.
17. Kroupa, D. M.; Roh, J. Y.; Milstein, T. J.; Creutz, S. E.; Gamelin, D. R. *ACS Energy Lett.* **2018,** *3*, 2390-2395.
18. Zhang, X.; Zhang, Y.; Zhang, X.; Yin, W.; Wang, Y.; Wang, H.; Lu, M.; Li, Z.; Gu, Z.; Yu, W. W. *J. Mater. Chem. C* **2018,** *6*, 10101-10105.
19. Cohen, T. A.; Milstein, T. J.; Kroupa, D. M.; MacKenzie, J. D.; Luscombe, C. K.; Gamelin, D. R. *J. Mater. Chem. A* **2019,** *7*, 9279-9288.
20. Crane, M. J.; Kroupa, D. M.; Roh, J. Y.; Anderson, R. T.; Smith, M. D.; Gamelin, D. R. *ACS Appl. Energy Mater.* **2019,** *2*, 4560-4565.
21. Erickson, C. S.; Crane, M. J.; Milstein, T. J.; Gamelin, D. R. *J. Phys. Chem. C* **2019,** *123*, 12474-12484.
22. Luo, X.; Ding, T.; Liu, X.; Liu, Y.; Wu, K. *Nano Lett.* **2019,** *19*, 338-341.
23. Milstein, T. J.; Kluherz, K. T.; Kroupa, D. M.; Erickson, C. S.; De Yoreo, J. J.; Gamelin, D. R. *Nano Lett.* **2019,** *19*, 1931-1937.
24. Zhou, D.; Sun, R.; Xu, W.; Ding, N.; Li, D.; Chen, X.; Pan, G.; Bai, X.; Song, H. *Nano Lett.* **2019,** *19*, 6904-6913.
25. Cai, T.; Wang, J.; Li, W.; Hills-Kimball, K.; Yang, H.; Nagaoka, Y.; Yuan, Y.; Zia, R.; Chen, O. *Adv. Sci.* **2020,** *7*, 2001317.
26. Ding, N.; Xu, W.; Zhou, D.; Ji, Y.; Wang, Y.; Sun, R.; Bai, X.; Zhou, J.; Song, H. *Nano Energy* **2020,** *78*, 105278.
27. Ishii, A.; Miyasaka, T. *J. Chem. Phys.* **2020,** *153*, 194704.
28. Zeng, M.; Artizzu, F.; Liu, J.; Singh, S.; Locardi, F.; Mara, D.; Hens, Z.; Van Deun, R. *ACS Appl. Nano Mater.* **2020,** *3*, 4699-4707.
29. Zhu, Y.; Pan, G.; Shao, L.; Yang, G.; Xu, X.; Zhao, J.; Mao, Y. *J. Alloys Compd.* **2020,** *835*, 155390.
30. Huang, H.; Li, R.; Jin, S.; Li, Z.; Huang, P.; Hong, J.; Du, S.; Zheng, W.; Chen, X.; Chen, D. *ACS Appl. Mater. Interfaces* **2021,** *13*, 34561-34571.
31. Xu, K.; Chen, D.; Huang, D.; Zhu, H. *J. Lumin.* **2021,** *240*, 118464.
32. Chang, W. J.; Irgen-Gioro, S.; Padgaonkar, S.; López-Arteaga, R.; Weiss, E. A. *J. Phys. Chem. C* **2021,** *125*, 25634-25642.
33. Roh, J. Y. D.; Smith, M. D.; Crane, M. J.; Biner, D.; Milstein, T. J.; Krämer, K. W.; Gamelin, D. R. *Phys. Rev. Mater.* **2020,** *4*, 105405.
34. Demirbilek, R.; Heber, J.; Sergey, I. N. In *Charge transfer and 4fn-4fn-1 5d transitions of trivalent rare-earch ions in CsCdBr3*, Proc.SPIE, 2002.
35. Jørgensen, C. K. *Prog. Inorg. Chem.* **2007,** *12*, 101-158.
36. Watanabe, K.; Koshimizu, M.; Yanagida, T.; Fujimoto, Y.; Asai, K. *Jpn. J. Appl. Phys.* **2016,** *55*, 02BC20.
37. Milstein, T. J.; Roh, J. Y.; Jacoby, L. M.; Crane, M. J.; Sommer, D. E.; Dunham, S. T.; Gamelin, D. R. *Chem. Mater.*, submitted.
38. Li, X.; Duan, S.; Liu, H.; Chen, G.; Luo, Y.; Ågren, H. *J. Phys. Chem. Lett.* **2019**, 487-492.

39. Akkerman, Q. A.; D'Innocenzo, V.; Accornero, S.; Scarpellini, A.; Petrozza, A.; Prato, M.; Manna, L. *J. Am. Chem. Soc.* **2015,** *137*, 10276-10281.
40. Nedelcu, G.; Protesescu, L.; Yakunin, S.; Bodnarchuk, M. I.; Grotevent, M. J.; Kovalenko, M. V. *Nano Lett.* **2015,** *15*, 5635-5640.
41. Imran, M.; Caligiuri, V.; Wang, M.; Goldoni, L.; Prato, M.; Krahne, R.; De Trizio, L.; Manna, L. *J. Am. Chem. Soc.* **2018,** *140*, 2656-2664.
42. Creutz, S. E.; Crites, E. N.; De Siena, M. C.; Gamelin, D. R. *Chem. Mater.* **2018,** *30*, 4887–4891.
43. Zhao, S.; Zhang, Y.; Zang, Z. *Chem. Commun.* **2020,** *56*, 5811-5814.
44. Henling, L. M.; McPherson, G. L. *Phys. Rev. B* **1977,** *16*, 4756-4760.
45. McPherson, G. L.; Henling, L. M. *Phys. Rev. B* **1977,** *16*, 1889-1892.
46. Yin, W.-J.; Shi, T.; Yan, Y. *Appl. Phys. Lett.* **2014,** *104*, 063903.
47. Li, C.; Guerrero, A.; Zhong, Y.; Huettner, S. *J. Phys.: Condens. Matter* **2017,** *29*, 193001.
48. Kang, J.; Wang, L.-W. *J Phys. Chem. Lett.* **2017,** *8*, 489-493.
49. Liu, N.; Yam, C. *Phys. Chem. Chem. Phys.* **2018,** *20*, 6800-6804.
50. Steele, J. A.; Puech, P.; Monserrat, B.; Wu, B.; Yang, R. X.; Kirchartz, T.; Yuan, H.; Fleury, G.; Giovanni, D.; Fron, E.; Keshavarz, M.; Debroye, E.; Zhou, G.; Sum, T. C.; Walsh, A.; Hofkens, J.; Roeffaers, M. B. J. *ACS Energy Lett.* **2019,** *4*, 2205-2212.
51. Sommer, D. E.; Gamelin, D. R.; Dunham, S. T. *Phys. Rev. Mater.*, in press.
52. Wu, K.; Liang, G.; Shang, Q.; Ren, Y.; Kong, D.; Lian, T. *J. Am. Chem. Soc.* **2015,** *137*, 12792-12795.
53. Essig, S.; Allebé, C.; Remo, T.; Geisz, J. F.; Steiner, M. A.; Horowitz, K.; Barraud, L.; Ward, J. S.; Schnabel, M.; Descoeudres, A.; Young, David L.; Woodhouse, M.; Despeisse, M.; Ballif, C.; Tamboli, A. *Nat. Energy* **2017,** *2*, 17144.
54. Cariou, R.; Benick, J.; Feldmann, F.; Höhn, O.; Hauser, H.; Beutel, P.; Razek, N.; Wimplinger, M.; Bläsi, B.; Lackner, D.; Hermle, M.; Siefer, G.; Glunz, S. W.; Bett, A. W.; Dimroth, F. *Nat. Energy* **2018,** *3*, 326-333.
55. Meijer, J.-M.; Aarts, L.; van der Ende, B. M.; Vlugt, T. J. H.; Meijerink, A. *Phys. Rev. B* **2010,** *81*, 035107.
56. van der Ende, B. M.; Aarts, L.; Meijerink, A. *Adv. Mat.* **2009,** *21*, 3073-3077.
57. Richards, B. S. *Sol. Energy Mater. Sol. Cells* **2006,** *90*, 2329-2337.
58. Ishii, A.; Miyasaka, T. *Adv. Sci.* **2020,** *7*, 1903142.
59. Liu, Z.; Sofia, S. E.; Laine, H. S.; Woodhouse, M.; Wieghold, S.; Peters, I. M.; Buonassisi, T. *Energy Environ. Sci.* **2020,** *13*, 12-23.
60. Erickson, C. S.; Bradshaw, L. R.; McDowall, S.; Gilbertson, J. D.; Gamelin, D. R.; Patrick, D. L. *ACS Nano* **2014,** *8*, 3461-3467.
61. Bergren, M. R.; Makarov, N. S.; Ramasamy, K.; Jackson, A.; Guglielmetti, R.; McDaniel, H. *ACS Energy Lett.* **2018,** *3*, 520-525.
62. Cohen, T. A.; Huang, Y.; Bricker, N. A.; Juhl, C. S.; Milstein, T. J.; MacKenzie, J. D.; Luscombe, C. K.; Gamelin, D. R. *Chem. Mater.* **2021**.
63. Paschotta, R.; Nilsson, J.; Tropper, A. C.; Hanna, D. C. *IEEE J Quantum Electron.* **1997,** *33*, 1049-1056.
64. Bradshaw, L. R.; Knowles, K. E.; McDowall, S.; Gamelin, D. R. *Nano Lett.* **2015,** *15*, 1315-1323.

Chapter 2 Picosecond Quantum Cutting in Ytterbium-Doped $CsPbCl_3$ Nanocrystals

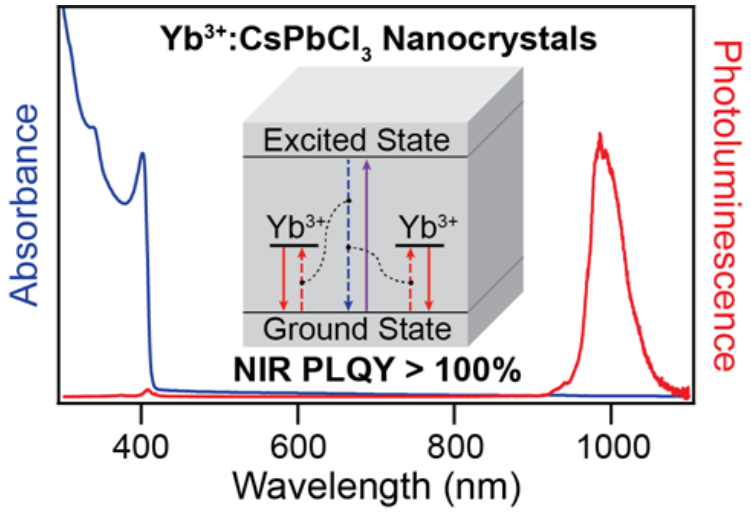

Abstract. Recent advances in ytterbium doping of $CsPbX_3$ (X = Cl, Cl/Br) nanocrystals have opened exciting new opportunities for their application as downconverters in solar energy conversion technologies. Here, we describe a hot-injection synthesis of Yb^{3+}:$CsPbCl_3$ nanocrystals that reproducibly yields sensitized Yb^{3+} $^2F_{5/2} \rightarrow {}^2F_{7/2}$ luminescence with near-infrared photoluminescence quantum yields (PLQYs) well over 100% and near-zero excitonic luminescence. Near-infrared PLQYs of 170% have been measured. Through a combination of synthesis, variable-temperature photoluminescence spectroscopy, and transient-absorption and time-resolved photoluminescence spectroscopies, we show that the formation of shallow Yb^{3+}-induced defects play a critical role in facilitating a picosecond nonradiative energy-transfer process that de-excites the photoexcited nanocrystal and simultaneously excites two Yb^{3+} dopant ions, *i.e.*, quantum cutting. Energy transfer is very efficient at all temperatures between 5 K and room temperature, but only grows more efficient as the temperature is elevated in this range. Our results provide insights into the microscopic mechanism behind the extremely efficient sensitization of Yb^{3+} luminescence in $CsPbX_3$ nanocrystals, with ramifications for future applications of high-efficiency spectral-conversion nanomaterials in solar technologies.

2.1 Introduction

All-inorganic, metal-halide perovskite $CsPbX_3$ (X = Cl, Br, I) nanocrystals (NCs) have been the subject of intense recent research due to their high photoluminescence quantum yields (PLQY), narrow emission bandwidths, broadband absorption, and band-gap tunability throughout the ultraviolet (UV), visible, and near-infrared (NIR) spectrum *via* size control (quantum size effects) and compositional alloying.[1-3] These properties have made perovskite NCs attractive materials for optoelectronic applications such as LEDs, lasing, displays, solar cells, and photodetectors.[4-6] The incorporation of impurity ions, or doping, in metal-halide perovskite NCs also imparts interesting optical properties. For example, substitutional B-site doping of $CsPbCl_3$ NCs with manganese ions (Mn^{2+}) gives rise to a broad, red-shifted emission band centered around 600 nm,[7-9] resulting from NC sensitization of internal Mn^{2+} *d-d* emission. Very recently, successful doping of various trivalent lanthanide ions (or rare earths, RE) into colloidal perovskite NCs of $CsPbCl_3$ and $CsPbCl_{3-x}Br_x$ has been reported.[10-11] These materials display the rich, efficient, and inherently narrow luminescence features of the lanthanides sensitized by the perovskite NCs, and have enabled promising proof-of-principle demonstration of downconversion approaches to efficient solid-state lighting and solar photovoltaics.

Several publications have highlighted the attractiveness of Yb^{3+} as a luminescence activator for applications in solar spectral shifting and luminescent solar concentration.[10, 12-15] Yb^{3+} has a simple electronic structure involving a single $^2F_{5/2}$ excited-state multiplet centered ~1.3 eV above the $^2F_{7/2}$ ground state. This energy difference matches the bandgap of silicon (1.1 eV) well. Whereas extensive work has been done on Yb^{3+} doping of colloidal $NaYF_4$, LaF_3, and related insulator NCs, most intermediate- or narrow-gap colloidal semiconductor NCs possess soft anions that have low affinity for Yb^{3+}, and many possess tetrahedral cation sites that also disfavor Yb^{3+} incorporation. Sensitized NIR emission has been reported for colloidal Yb^{3+}-doped CdSe, $NaInS_2$, and $PbInS_4$ NCs, but the resulting NIR PLQYs were relatively small (<~10%), limiting practical applications.[14, 16] The successful synthesis of Yb^{3+}-doped $CsPbCl_3$ NCs thus addresses a long-standing challenge in nanocrystal chemistry. Remarkably, not only did this work demonstrate sensitization of Yb^{3+} luminescence by the NCs, but it also described NIR PLQYs that exceeded 100%, attributed to quantum cutting. Yb^{3+} is a well-known activator for quantum cutting in bulk crystals, where the process is generally achieved *via* co-doping with other lanthanides such as Nd^{3+} or Pr^{3+}.[12, 17-18] Very little is known about the structural or photophysical properties of Yb^{3+} dopants

in perovskite NCs, however. Here, we apply a combination of synthesis and spectroscopic methods to examine the microscopic energy-transfer mechanism responsible for PLQYs > 100% in Yb^{3+}:$CsPbCl_3$ NCs. Comparisons between Yb^{3+} and Mn^{2+} luminescence activators in perovskite nanocrystals are also discussed.

2.2 Physical Characterization

In our hands, synthesis of Yb^{3+}:$CsPbCl_3$ NCs following the methods described in refs 10-11 was met with some difficulties associated with poor precursor solubility (particularly $YbCl_3$•$6H_2O$). We have therefore developed a hot-injection synthesis of colloidal $CsPbCl_3$ and Yb^{3+}:$CsPbCl_3$ NCs following the approach we previously introduced[19] for making Cs_2AgBiX_6 (X = Cl, Br) NCs, in which metal-acetate salts and chlorotrimethylsilane serve as the cation and halide precursors, respectively (see **2.7** for complete synthetic details). This synthetic route is attractive in part because of the high solubilities of the acetate precursors in high-boiling-point organic solvents, compared to less-soluble chloride salts used in other popular syntheses.[19-21] **Figure 2.1** summarizes general characterization data collected for representative undoped $CsPbCl_3$ NCs and (6%) Yb^{3+}-doped $CsPbCl_3$ NCs. The transmission electron microscopy (TEM) images in **Figures 2.1A,B** show cubic crystallites with average edge lengths of approximately 13 and 16 nm for the undoped and Yb^{3+}-doped $CsPbCl_3$ NCs, respectively. **Figure 2.1C** shows X-ray diffraction (XRD) data collected from both samples, consistent with the perovskite crystal structure without detectable crystalline impurities. Negligible shifts of the XRD reflections are observed with Yb^{3+} doping, even at high Yb^{3+} concentrations. **Figures 2.1D,E** show representative room-temperature absorption and steady-state PL spectra of undoped and Yb^{3+}-doped $CsPbCl_3$ NCs, respectively. The absorption spectra of both samples show similar onsets and peak positions. The PL spectrum of the undoped $CsPbCl_3$ NCs shows strong luminescence at 410 nm, corresponding to band-edge excitonic emission. In contrast, the PL spectrum of the Yb^{3+}:$CsPbCl_3$ NCs shows very little band-edge luminescence but intense NIR PL centered at 990 nm, corresponding to the $^2F_{5/2} \rightarrow {}^2F_{7/2}$ *f-f* emission of Yb^{3+}. The average lifetime of this Yb^{3+} emission is over 2 ms (**Appendix 2.5**), approaching its radiative limit and suggesting little nonradiative quenching of the emissive excited state. These data demonstrate successful synthesis of high-quality Yb^{3+}:$CsPbCl_3$ NCs.

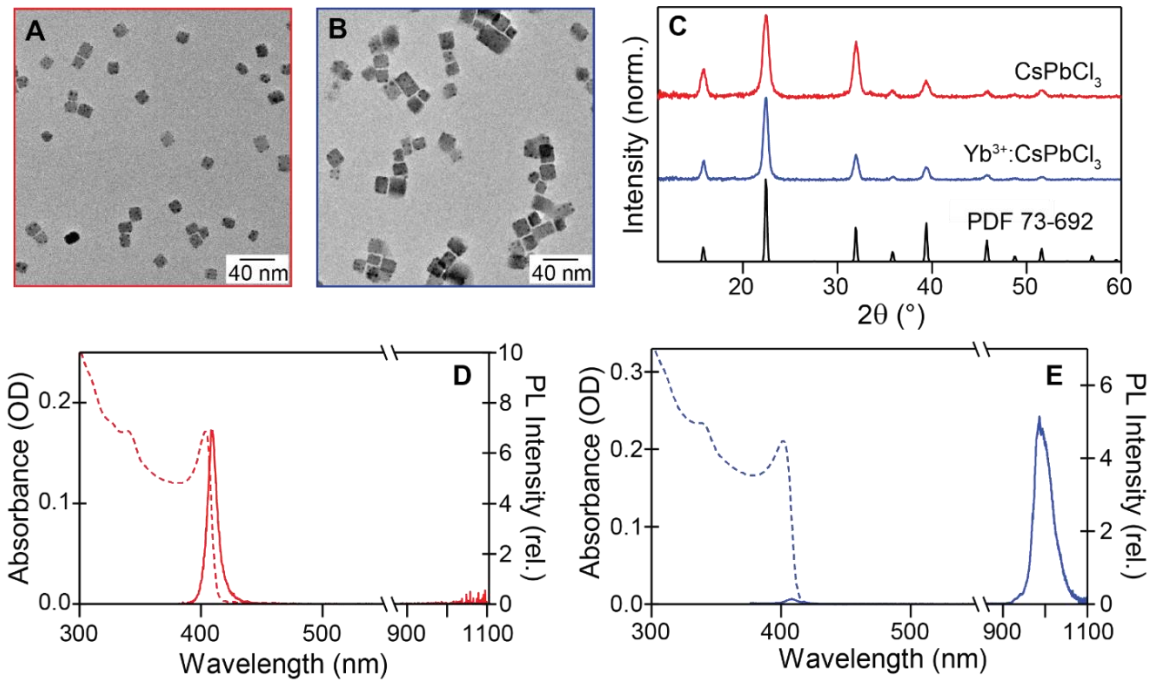

Figure 2.1 Physical characterization of Yb^{3+}:$CsPbCl_3$ nanocrystals.

(A,B) TEM and **(C)** XRD data for undoped *d* = 13 nm $CsPbCl_3$ NCs (red) and *d* = 16 nm 6.0% Yb^{3+}:$CsPbCl_3$ NCs (blue). The dark spots in the TEM images result from *in situ* Pb^{2+} reduction by the electron beam, as commonly observed in $CsPbX_3$ NCs.[22] **(D,E)** Absorbance (dashed lines) and PL (solid lines) spectra of the same NCs. Yb^{3+} concentrations are defined as $[Yb^{3+}]/([Yb^{3+}] + [Pb^{2+}])$, measured analytically on the purified NCs by ICP-AES.

2.3 Yb^{3+} PL Efficiency

To probe the effect of increasing the Yb^{3+} doping level, we performed a series of reactions under fixed conditions, varying only the nominal $[Yb^{3+}]$:$[Pb^{2+}]$ precursor ratio in the reaction mixture. We do not observe any appreciable changes in the $CsPbCl_3$ NC absorption spectrum with increasing Yb^{3+} concentration (**Appendix 2.19**), but both Yb^{3+} incorporation and Yb^{3+} luminescence intensity appear to increase with increasing Yb^{3+} precursor concentrations before peaking at a nominal $[Yb^{3+}]$:$[Pb^{2+}]$ ratio of ~0.8 under these conditions, and then decrease again when this ratio is increased further (**Figure 2.2A** and **Appendix 2.4**). Upon analysis, we find a general trend of increasing NIR luminescence with increasing Yb^{3+} incorporation across the entire series, with some scatter. **Figure 2.2B** plots the excitonic and Yb^{3+} $^2F_{5/2} \rightarrow {}^2F_{7/2}$ absolute PLQYs measured using an integrating sphere *vs* the analytical Yb^{3+} concentration in the NCs. Excitonic PLQYs of the undoped samples are ~20% and decrease sharply to <1% upon increasing the Yb^{3+} concentration to just ~0.7% (see **Appendix 2.12**). Conversely, the Yb^{3+} $^2F_{5/2} \rightarrow {}^2F_{7/2}$ PLQYs

increase roughly in proportion to the analytical doping concentration of Yb^{3+}, rising from 10 to 130% for 0.2 and 7.4% Yb^{3+}, respectively. At the highest Yb^{3+} doping level, we measure absolute PLQYs well above 100%, confirming this observation in recent reports.[11] The Cs^{+} concentration in the reaction mixture was also found to affect both Yb^{3+} incorporation and the resulting NC optical properties (**Appendix 2.5**). **Figure 2.2B** includes additional excitonic and Yb^{3+} $^2F_{5/2} \rightarrow {}^2F_{7/2}$ PLQY data points obtained from reactions varying the nominal Cs^{+} concentration, and these data follow the same trend lines as those obtained with [Yb^{3+}] as the reaction variable, suggesting that the final Yb^{3+} concentration primarily dictates the resulting spectral properties.

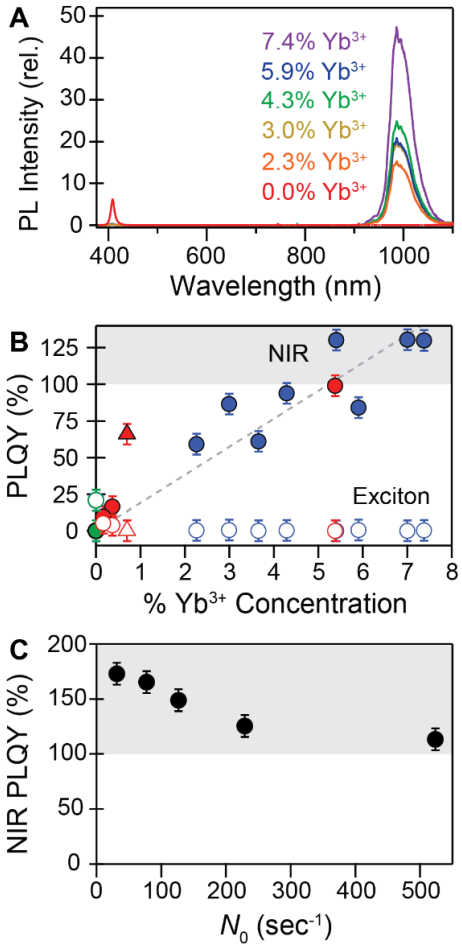

Figure 2.2 Quantum-cutting PL efficiency.

(A) Room-temperature PL spectra of colloidal $CsPbCl_3$ NCs (red) and Yb^{3+}:$CsPbCl_3$ NCs with analytical (nominal [Yb^{3+}]:[Pb^{2+}]) Yb^{3+}concentrations of 2.3% (0.1, orange), 3.0% (0.2, yellow), 4.3% (0.4, green), 5.9% (1.5, blue), and

7.4% (0.8, purple), all prepared with a fixed nominal ratio of $[Cs^+]:[Pb^{2+}] = 1.2$ in the reaction vessel. Yb^{3+} concentrations are defined as $[Yb^{3+}]/([Yb^{3+}] + [Pb^{2+}])$, measured analytically on the purified NCs by ICP-AES. **(B)** Exciton (open) and NIR (closed) PLQYs plotted as a function of Yb^{3+} concentration. λ_{ex} = 375 nm, CW excitation rate, N_0 = 369 sec^{-1}. The green data are from reactions without the addition of Yb^{3+} (undoped NCs). The blue data are from reactions varying the nominal Yb^{3+} concentrations at a fixed ratio of $[Cs^+]:[Pb^{2+}] = 1.4$. The red data are from additional reactions varying the nominal Cs^+ concentrations at a fixed ratio of $[Yb^{3+}]:[Pb^{2+}] = 0.2$. The data represented as triangles are from a reaction at the highest nominal $[Cs^+]:[Pb^{2+}]$, where a mixture of $CsPbCl_3$ and Cs_4PbCl_6 crystal phases are detected by XRD. **(C)** NIR PLQYs of a sample of 5.2% Yb^{3+}-doped $CsPbCl_3$ NCs plotted as a function of per-NC photoexcitation rate, tuned by varying the CW photoexcitation power at λ_{ex} = 380 nm. The experimental NIR PLQY reaches 170% at its highest value.

Importantly, the PLQYs of these NCs are somewhat power dependent, showing saturation effects even at relatively low excitation powers. **Figure 2.2C** plots the NIR PLQY for 5.2% Yb^{3+}-doped $CsPbCl_3$ NCs as a function of NC excitation rate. The PLQY increases from 110% up to 170% upon reducing the excitation rate by a factor of ~17. PL saturation occurs at these relatively low excitation rates because of the combination of the very large absorption cross-sections of the $CsPbCl_3$ NCs (σ = 4.2 x10^{-14} cm^2 at 380 nm) with the long Yb^{3+} PL decay time (τ_{avg} > 2 ms). This PL saturation reflects the introduction of a new non-radiative relaxation mechanism that only occurs upon photoexcitation of already excited NCs. The PLQY of 170% measured here is the highest for any colloidal NC to date and is very close to the theoretical maximum of 200% for such a visible-to-NIR quantum cutting process involving Yb^{3+}.

Figure 2.3A plots steady-state PL spectra of 7.4% Yb^{3+}:$CsPbCl_3$ NCs measured at several temperatures from 5 to 265 K. The excitonic PL is much weaker than the Yb^{3+} PL, but it is magnified here (12x) for clarity. At 5 K, the NIR region of the PL spectrum shows several resolved features characteristic of crystal-field splittings in the Yb^{3+} $^2F_{5/2} \rightarrow {}^2F_{7/2}$ emission. Increasing the temperature broadens these features, but the integrated intensities do not drop. Instead, whereas the excitonic PL intensity decreases rapidly as the temperature increases, the NIR Yb^{3+} $^2F_{5/2} \rightarrow {}^2F_{7/2}$ PL intensity only increases with increasing temperature. The onset temperature for this increase is ~50 K, possibly associated with thermal excitation of vibrations. **Figure 2.3B** summarizes this temperature dependence by plotting the integrated excitonic and Yb^{3+} $^2F_{5/2} \rightarrow {}^2F_{7/2}$ PL intensities *vs* temperature. The NIR emission intensity actually triples upon increasing temperature from 5 to 265 K. The absorbance of these Yb^{3+}:$CsPbCl_3$ NCs at the excitation

wavelength changes by <10% over this temperature range (**Appendix 2.17**). The integrated NIR PL is thus 10-200 times more intense than the excitonic PL at all temperatures. Overall, these data show efficient Yb^{3+} sensitization even at 5 K, and indicate that some aspect of the sensitization is thermally assisted. Importantly, these data show no evidence of thermally activated nonradiative decay of the luminescent Yb^{3+} excited state.

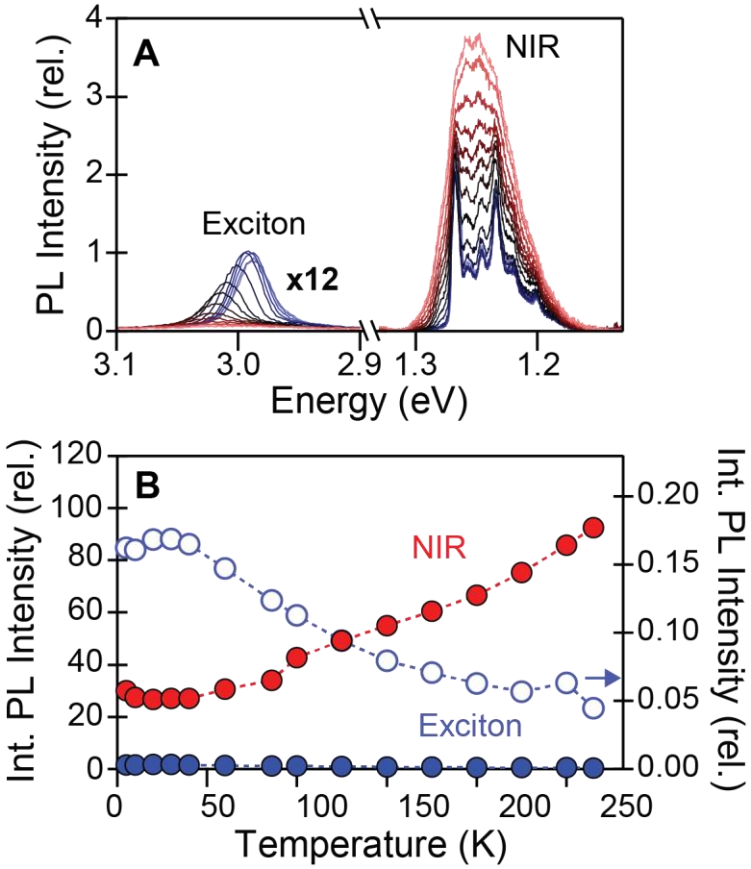

Figure 2.3 Variable temperature Yb^{3+}:$CsPbCl_3$ nanocrystal PL.

(A) Variable-temperature photoluminescence spectra of *d* = 16 nm 7.4% Yb^{3+}:$CsPbCl_3$ NCs, measured from 5 (light blue) to 280 K (pink). **(B)** Integrated NIR and excitonic PL intensities plotted *vs* temperature. The excitonic PL intensity is plotted both on same scale (closed circles) and on a magnified scale (open circles, x550) as the NIR PL.

2.4 Dynamics

To probe the origins of this extremely efficient sensitized NIR luminescence in these Yb^{3+}:$CsPbCl_3$ NCs, we applied time-resolved spectroscopic techniques. **Figure 2.4** compares room-temperature excitonic PL-decay and transient-absorption (TA) exciton-bleach-recovery

dynamics measured for a series of Yb^{3+}:$CsPbCl_3$ NCs with Yb^{3+} content ranging from 0 – 6%. The time-resolved PL (TRPL) data (**Figure 2.4A**) are limited at short times by an approximately 280 ps instrument response time, but at longer times these data show nearly monoexponential decay with a time constant of ~6 ns, associated with radiative decay of the exciton (τ_{rad}). The PL intensity of the slow component as a function of time [$I_S(t)$] can be fit by a monoexponential decay function at delay times, *t*, between 5 and 15 ns, defined by

$$I_S(t) = A\exp[-t/\tau] \quad (2.1)$$

where *A* denotes the fitting amplitude and τ denotes the time constant. The amplitude of this slow decay component obtained from fitting the normalized PL decay curves is plotted *vs* Yb^{3+} concentration in **Figure 2.4B**. This amplitude decreases with increasing Yb^{3+} concentration, indicating a reduction in slow exciton PL with increasing Yb^{3+} doping. To obtain the amplitude of all fast PL decay (including decay that occurs faster than the instrument response time), we subtracted the slow component's amplitude from the normalized amplitude (= 1) at $t = 0$. The fast amplitudes are also plotted in **Figure 2.4B**. For comparison, **Figure 2.4B** further plots the ratio of steady-state NIR PL intensity to total PL intensity at each Yb^{3+} concentration: [*I*(NIR)/*I*(total)]. The fraction of fast PL decay roughly tracks this ratio at larger Yb^{3+} concentrations, but the data show that most of the effect of Yb^{3+} occurs faster than the instrument response (280 ps). These data thus suggest that Yb^{3+} excitation is associated with very rapid exciton depopulation.

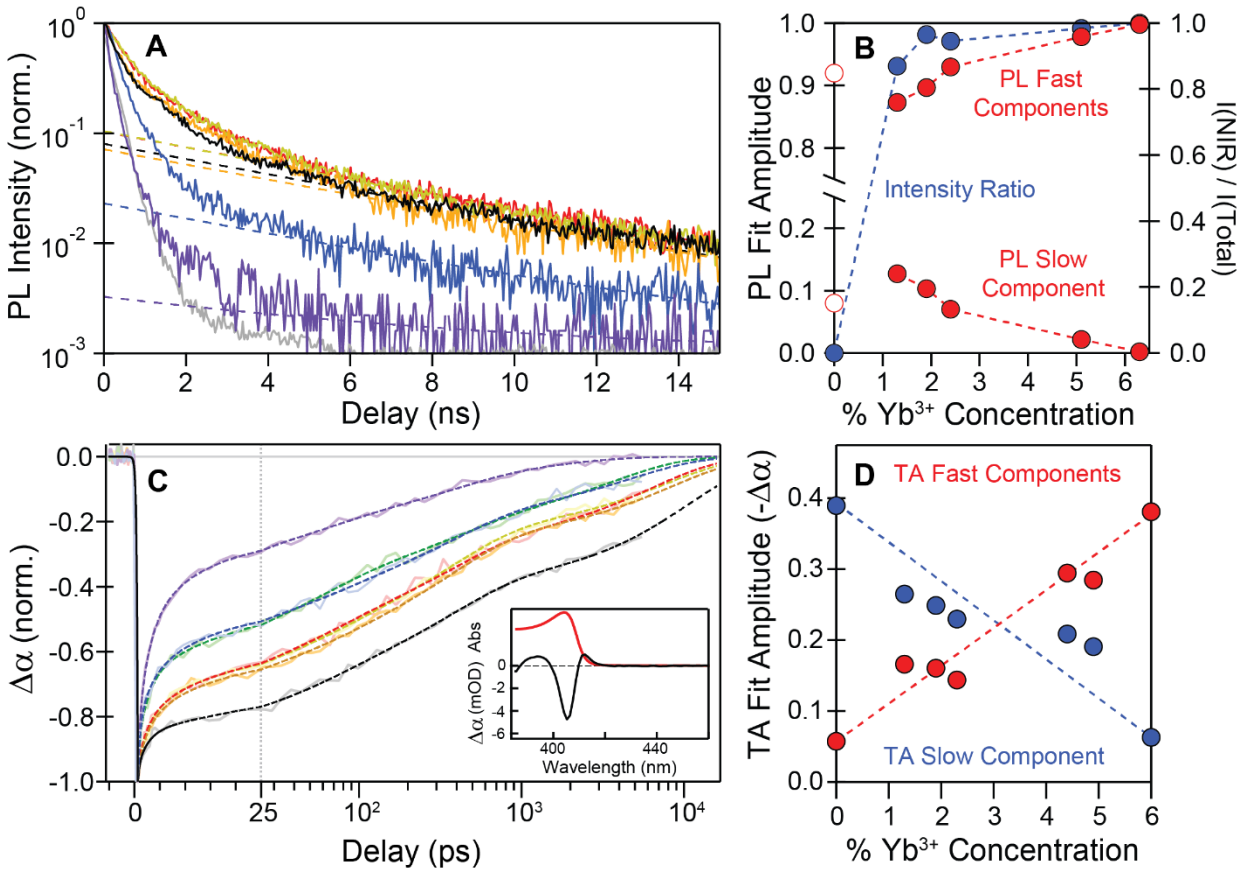

Figure 2.4 Room-temperature exciton dynamics of Yb^{3+}:$CsPbCl_3$ NCs.

(A) Room-temperature TRPL decay traces for undoped (black trace) and Yb^{3+}-doped (red to purple) $CsPbCl_3$ NCs. The instrument response function (IRF) is also plotted (grey). The IRF curve is shifted downward by 10^{-3} for clarity of the logarithmic presentation. **(B)** Fast and slow PL decay amplitudes (red) and PL intensity ratio (blue) plotted *vs* analytical Yb^{3+} concentration. **(C)** First-exciton-bleach-recovery kinetics measured at room temperature. Inset: Representative absorption and transient-absorption spectra at the $CsPbCl_3$ NC absorption edge, showing the negative first-exciton bleach signal. **(D)** Fast (red) and slow (blue) TA amplitudes plotted *vs* analytical Yb^{3+} concentration.

TA data for the same series of Yb^{3+}:$CsPbCl_3$ NCs exhibit qualitatively similar trends but provide more information about short-time dynamics. TA spectra of these samples are all dominated by a bleach of the lowest-energy exciton transition, attributable to band-edge state filling upon photoexcitation (**Figure 2.4C**, see Appendix). **Figure 2.4C** summarizes the excited-state dynamics for the various NC samples shown in **Figure 2.4A**, plotting TA amplitudes averaged over the full-width-at-half-maximum of this band-edge bleach feature *vs* time. These TA kinetics were fit using the kinetic model described by Wu *et al.* for $CsPbBr_3$ NCs (sum of

exponentials weighted by their respective carrier contribution to the band-edge bleach signal; model details in the SI).[23] The fitting results agree well with those in ref. [23] for the undoped NCs, and we modified the model to account for additional Yb^{3+}-based processes in the doped NCs. Like in the TRPL, the amplitude of the slow component associated with radiative recombination (ns time constants) systematically decreases with increasing Yb^{3+} content (**Figure 2.4D**), suggesting the introduction of new excited-state recombination pathways upon doping. Accordingly, two new fast-decay components (with sub-ps and ~10 ps time constants) appear upon introduction of Yb^{3+} and increase in amplitude with increasing Yb^{3+} content (**Figure 2.4D**). These results verify the conclusion drawn from the TRPL analysis that Yb^{3+} doping introduces fast components in the exciton relaxation dynamics.

The dynamics and VTPL data allow analysis of the very high quantum yields in these samples. Taking the NIR PL quantum yield to be

$$\Phi_{\text{NIR PL}} = \frac{nk_{\text{ET}}}{(nk_{\text{ET}}+k_{\text{rad}}+k_{\text{tr}})} * \Phi_{\text{Yb}^{3+}} \quad (2.2)$$

in which $\Phi_{\text{Yb}^{3+}}$ represents the internal luminescence QY of the Yb^{3+} activators and ET, rad, and tr and denote energy transfer to Yb^{3+}, radiative band-edge recombination, and carrier trapping, respectively. Increasing *n* (the number of optically active Yb^{3+} activators) results in a higher NIR PLQY as the branching ratio approaches unity. $\Phi_{\text{Yb}^{3+}}$ itself is inherently large, as determined from the VTPL data in which the NIR emission shows no thermal quenching when the temperature is increased toward room temperature. Interestingly, despite the rapid and efficient energy transfer in combination with the fast carrier trapping, excitonic luminescence is still observed. We understand this to be the result of a small *n* (see Appendix 2.2 for details and discussion below).

It is instructive to compare Yb^{3+} and Mn^{2+} as luminescence activators in perovskite NCs. Although both activator ions can have very high internal quantum efficiencies for luminescence, the highest PLQYs of the Yb^{3+}:$CsPbCl_3$ NCs (170%, **Figure 2.2C**) are almost three times as large as the highest PLQYs observed from Mn^{2+}:$CsPbCl_3$ NCs to date (up to 60%).[7-9, 24] Furthermore, energy transfer from the NCs to Yb^{3+} is not suppressed at cryogenic temperatures, nor is it too slow to compete with exciton recombination despite the fact that exciton recombination accelerates to sub-nanosecond timescales at low temperatures. These characteristics contrast those of Mn^{2+}:$CsPbCl_3$ NCs, whose luminescence is completely dominated by excitonic emission at low temperatures because energy transfer to Mn^{2+} is too slow to compete with exciton recombination at these temperatures. Energy transfer to Mn^{2+} in $CsPbCl_3$ NCs likely proceeds *via* a resonant

Dexter-type energy-transfer process involving the NC exciton and an upper ligand-field excited state of Mn^{2+} at the same energy.[9] This energy matching along with the fact that Mn^{2+} experiences greater covalency with the surrounding lattice should give rise to much larger electronic coupling and hence greater Dexter energy-transfer rates compared to Yb^{3+}, which has poor electronic coupling and no upper excited states at the energy of the $CsPbCl_3$ exciton. Thus, if energy transfer to Yb^{3+} proceeded by an analogous Dexter-type mechanism, then it should be much slower, not much faster as observed. Energy transfer to Mn^{2+} occurs on the timescale of hundreds of picoseconds to nanoseconds, but energy transfer to Yb^{3+} appears to occur on the timescale of one picosecond. Indeed, exciton depopulation leading to Yb^{3+} sensitization is so fast that it is competitive with other fast carrier-trapping processes active even in undoped $CsPbCl_3$ NCs, *e.g.*, as illustrated from their TA kinetics (sub-ps and ~2 ps for the hole- and electron-trapping time constants, respectively). Such fast energy transfer to Yb^{3+} appears incommensurate with the known characteristics of Yb^{3+} as a luminescence activator. This inconsistency suggests that energy transfer to Yb^{3+} must occur *via* an alternative route, rather than *via* normal exciton-dopant Dexter-type energy transfer.

2.5 Sensitization via the Defect Motif

We propose that the extremely fast exciton depopulation observed in these Yb^{3+}:$CsPbCl_3$ NCs, in conjunction with the correlation between Yb^{3+} doping and NIR PLQYs, implies the integral participation of lattice defects in the Yb^{3+} sensitization mechanism. Moreover, to achieve the extraordinary PLQYs of as high as ~170%, this sensitization mechanism must involve quantum cutting. To account for these considerations, we hypothesized that Yb^{3+} doping itself introduces correlated defects that rapidly localize excitation energy in the vicinity of the Yb^{3+} activators. Picosecond energy localization by such a defect would then be followed by energy transfer from that defect to a pair of neighboring Yb^{3+} ions, resulting in emission of two NIR photons, *i.e.*, quantum cutting. This process would be manifested in eq 2 as multiplication of the branching ratio by a factor of 2. If this hypothesis is correct, such defects are likely associated with the aliovalent charge of Yb^{3+} in the $CsPbCl_3$ lattice, which requires charge compensation.

To test for such a dopant-induced lattice defect, we doped $CsPbCl_3$ NCs with La^{3+} cations using the same methods employed to synthesize the Yb^{3+}:$CsPbCl_3$ NCs. La^{3+} is optically inert but still aliovalent, and it has the same charge-compensation requirements as Yb^{3+}. **Figure 2.5A** shows

PL spectra of 1.3% La^{3+}:$CsPbCl_3$ NCs collected at 4.7 and 223 K. For comparison, **Figure 2.5A** also plots parallel data collected for undoped $CsPbCl_3$ NCs. At 4.7 K, the La^{3+}:$CsPbCl_3$ NCs indeed show a prominent, broad PL feature indicative of shallow-trap emission. This feature peaks ~40 meV below the excitonic PL of the undoped $CsPbCl_3$ NCs. No other emission is observed from the La^{3+}:$CsPbCl_3$ NCs. A similar trap PL band has been reported for La^{3+}:$CsPbCl_3$ single crystals,[25] suggesting that this is an internal lattice defect not associated with the NC surfaces. This trap luminescence in these La^{3+}:$CsPbCl_3$ NCs is very bright below ~80 K, but increasing the temperature above ~80 K causes excitonic PL to grow in at the expense of the broad trap PL, and the overall PL decreases substantially (**Appendix 2.20** for additional data). The trap PL is still observed at the highest temperature in this series (223 K), and it is also observed at room temperature. At cryogenic temperature, ~99% of this trap PL decays within ~300 ps, with the remaining ~1% decaying slower (**Appendix 2.21**). The observation of near-band-edge trap PL in the La^{3+}:$CsPbCl_3$ NCs provides strong support for the hypothesis of a shallow dopant-induced defect state introduced when trivalent cations are doped into $CsPbCl_3$ NCs.

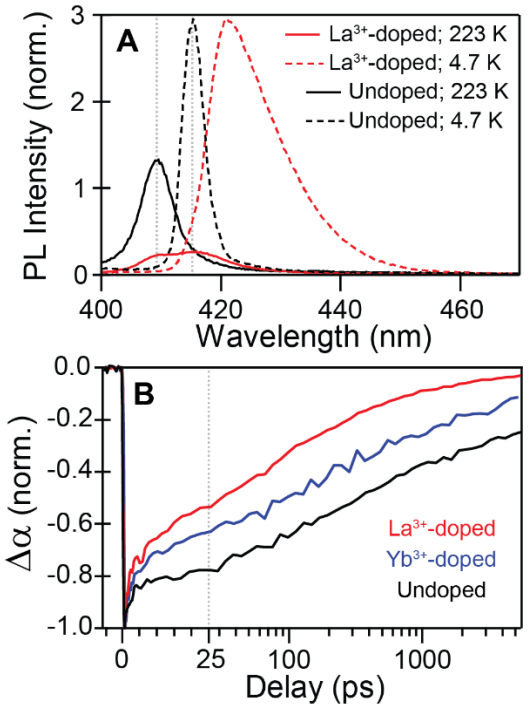

Figure 2.5 Induced-defect state PL and dynamics.

(**A**) Variable temperature PL of 1.3% La^{3+}-doped (red) and undoped (black) $CsPbCl_3$ NCs at 4.7 K (dashed) and 223 K (solid) under 375 nm excitation. (**B**) TA bleach recovery kinetics of undoped (black), 1.3% La^{3+}-doped (red), and 1.3% Yb^{3+}-doped (blue) $CsPbCl_3$ NCs.

This conclusion is bolstered by TA studies of the La^{3+}:$CsPbCl_3$ NCs. **Figure 2.5B** shows TA bleach recovery kinetics measured for undoped, Yb^{3+}-doped, and La^{3+}-doped $CsPbCl_3$ NC samples. Similar to the Yb^{3+}:$CsPbCl_3$ NC data, the La^{3+}:$CsPbCl_3$ NC kinetic trace is fit well using two additional fast bleach-recovery components (sub-ps and ~10 ps time constants) relative to the undoped $CsPbCl_3$ NCs, suggesting that both trivalent dopants introduce similar trapping defects.

The above information now allows a mechanism underlying the extremely efficient sensitization of NIR PL in Yb^{3+}:$CsPbCl_3$ NCs to be proposed. The data suggest that Yb^{3+} doping introduces a charge-compensating defect that acts as a shallow trap. This defect localizes excitation energy on the picosecond timescale. Charge compensation could be manifested as a cation vacancy (V_{Cs} or V_{Pb}) or loss of a surface oleylammonium ligand. Previous computational work characterizing possible common defects and their energies relative to the band edges in $CsPbBr_3$ has shown that V_{Cs} and V_{Pb} are both shallow traps,[26] which would be consistent with the relatively small energy difference between excitonic and trap-induced defect PL seen in **Figure 2.5**. The energies of such traps relative to the band edges of $CsPbCl_3$ are unknown, however, as is the influence of a neighboring trivalent cation on these energies. To be consistent with the observation of efficient quantum cutting, we propose that the relevant defect is a V_{Pb} within a charge-neutral M^{3+}-V_{Pb}-M^{3+} defect complex. In fact, an analogous charge-compensating motif is already well documented in $CsCdBr_3$ and related halide lattices, where it is known as a "McPherson pair".[27-28] Although the crystal structure of those materials differs from the perovskite structure, an analogous defect complex appears reasonable here. Additionally, V_{Pb} rather than V_{Cs} formation is consistent with our experimental observation that the NIR PLQY actually increases with increasing nominal Cs^+ concentration during synthesis, a condition that should disfavor V_{Cs} formation. Carrier capture by V_{Pb} within a Yb^{3+}-V_{Pb}-Yb^{3+} defect complex localizes this defect excited state in close proximity to two Yb^{3+} cations simultaneously; this localization enables energy transfer to both Yb^{3+} ions in a cooperative quantum-cutting step. The La^{3+}-induced defect emission exceeds only slightly the energy required for simultaneous excitation of both neighboring Yb^{3+} ions. This PL intensity is nearly zero at exactly twice the energy of the highest Yb^{3+} $^2F_{5/2}$-$^2F_{7/2}$ crystal-field absorption feature in this lattice (~2.56 eV), but this energy gap is easily bridged by a few lattice phonons. Importantly, because this defect state population decays within ~300 ps in the analogous

La^{3+}:$CsPbCl_3$ NCs, energy transfer from this state to Yb^{3+} must occur even faster than this, *i.e.*, this quantum cutting occurs on a picosecond timescale.

Scheme 2.1 summarizes these mechanistic conclusions. **Scheme 2.1A** illustrates the formation of a dopant-induced shallow defect level upon incorporation of trivalent impurity ions into the $CsPbCl_3$ lattice. This new defect level is able to compete with native defects for capture of photogenerated carriers. It is proposed to be a charge-neutral M^{3+}-V_{Pb}-M^{3+} defect complex. When the trivalent dopant is spectroscopically innocent, such as La^{3+}, formation of this defect is manifested as near-band-edge PL. Scheme 1b illustrates how this scenario changes when the trivalent defect is Yb^{3+}. In this case, formation of the trapped excited state is followed by nearly resonant energy transfer to form two excited Yb^{3+} ions in a single, concerted, quantum-cutting step. Quantum cutting is aided by the fact that the proposed V_{Pb} defect is always in close proximity to two Yb^{3+} ions because of its role in their charge compensation. This proximity provides sufficient electronic coupling to both Yb^{3+} ions for efficient simultaneous excitation of both. As a shallow defect, V_{Pb}-localized photogenerated charge carriers will have a large Bohr radius, aiding electronic coupling to both Yb^{3+} ions simultaneously (**Scheme 2.1C**). This proposed mechanism differs from the one suggested previously to explain quantum cutting in Yb^{3+}:$CsPbCl_3$ NCs,[11] which involves decay of a band-edge photogenerated electron to a defect state coupled to excitation of a single Yb^{3+} ion, and subsequent electron decay from the defect state to the valence band releasing another quantum of energy to excite a second Yb^{3+} ion. Our data provide direct evidence for formation of a shallow dopant-induced defect state in these materials, and in the absence of any other detectable mid-gap states in these NCs, this result strongly suggests that sensitization occurs *via* simultaneous excitation of Yb^{3+} pairs as illustrated in Scheme 1b. We note that the integral role of a specific defect implied by **Scheme 2.1** is consistent with the otherwise unusual observation that very high Yb^{3+} concentrations are needed to fully quench excitonic PL in these Yb^{3+}:$CsPbCl_3$ NCs, despite picosecond exciton depopulation kinetics. This apparent inconsistency is explained by the need for a specific Yb^{3+}-V_{Pb}-Yb^{3+} defect complex to achieve not only quantum cutting, but Yb^{3+} sensitization at all. In the absence of such a well-positioned (energetically and spatially) defect, exciton-to-Yb^{3+} energy transfer is expected to be very slow (much slower than Mn^{2+}) because of poor electronic coupling and a large energy mismatch.

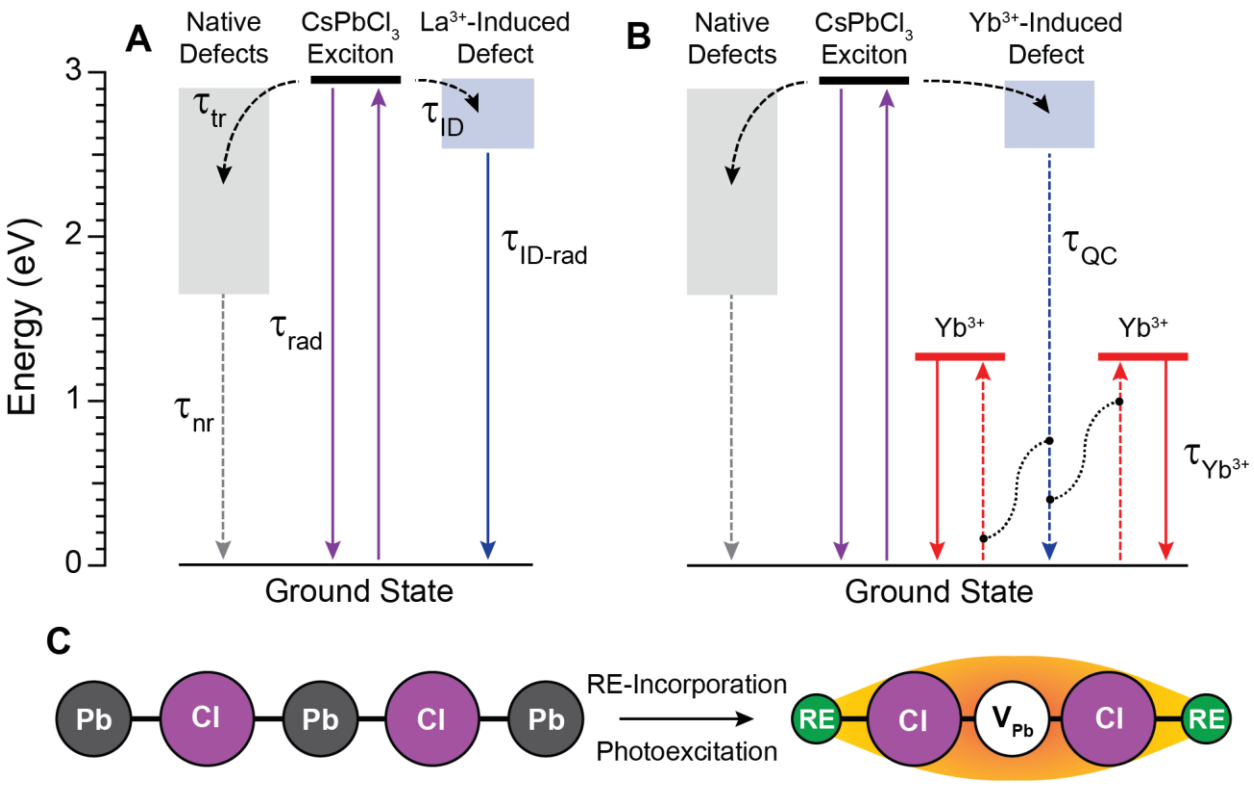

Scheme 2.1. Sensitized quantum-cutting scheme and defect motif. Proposed (A) La^{3+}-induced defect emission process, (B) Yb^{3+}-sensitization mechanism involving an analogous Yb^{3+}-induced defect state, and (C) the proposed charge-neutral vacancy-defect structure arising from doping $CsPbCl_3$ NCs with trivalent cations.

2.6 Conclusions

In conclusion, high-quality Yb^{3+}:$CsPbCl_3$ NCs have been synthesized *via* a novel hot-injection route starting from the respective metal-acetate salts and halide precursors. These NCs show analytical Yb^{3+} concentrations as high as 7.5% and replicable PLQYs exceeding 100%, reaching as high as ~170%. These extremely high PLQYs are shown to result from picosecond energy capture by a Yb^{3+}-induced defect that subsequently transfers its energy to two neighboring Yb^{3+} ions in a single cooperative step on the picosecond timescale. The above-unity quantum yields of these materials make them very promising for numerous photonic applications, from photodetection to solar energy conversion. The results presented here provide insights into the origins of this unique photophysical property, and further advance the development of Yb^{3+}-doped perovskite nanocrystals for such applications.

2.7 Experimental Methods

Materials. Lead acetate trihydrate [$Pb(OAc)_2 \cdot 3H_2O$] (99.9%, Baker Chemical), ytterbium acetate hydrate [$Yb(OAc)_3 \cdot xH_2O$] (99.9%, Strem Chemical), lanthanum acetate hydrate [$Yb(OAc)_3 \cdot xH_2O$] (99.9%, Strem Chemical), cesium acetate [CsOAc] (99.9%, Alfa Aesar), anhydrous ethanol (200 proof, Decon Laboratories, Inc.), chlorotrimethylsilane (TMS-Cl) (98%, Acros Organics), 1-octadecene (ODE) (90%, Sigma Aldrich), olyelamine (OAm) (70%, Sigma Aldrich), oleic acid (OA) (90%, Sigma Aldrich), hexanes (99%, Sigma Aldrich), and anhydrous ethyl acetate (99%, Sigma Aldrich) were used as received unless otherwise noted.

Nanocrystal synthesis and purification. Yb^{3+}:$CsPbCl_3$ NCs with the highest Yb^{3+} emission quantum yield were synthesized by hot-injection following procedures reported previously for synthesis of analogous Cs_2AgBiX_6 (X=Cl, Br) elpasolite NCs.[19] Briefly, 5 mL ODE, 0.5 mL OAm, 1.0 mL OA, 0.2 mmol $Pb(OAc)_2 \cdot 3H_2O$, 280 μL of 1 M CsOAc in ethanol, and 0.16 mmol $Yb(OAc)_3 \cdot xH_2O$ were added to a 50 mL round bottom flask. This solution was stirred and degassed on a Schlenk line at room temperature for 5 min before heating to 110 °C and degassed for 1 hr. The reaction vessel was then flushed with N_2 and heated to 240 °C. Upon reaching this temperature, 0.2mL of TMS-Cl in 0.5 mL ODE was swiftly injected. Immediately after injection, the flask was cooled to room temperature using a water bath. The crude nanocrystal solution was centrifuged at 1318 xg for 15 minutes. The supernatant was discarded and the pellet was resuspended in hexanes. The NCs were then washed with ethyl acetate. The solution was then centrifuged at 1318 xg for 10 min. The supernatant was discarded, and the pellet was resuspended in hexanes. The mixture was allowed to settle overnight and then filtered through a 0.2 μm PTFE filter. Samples were stored in glass vials in ambient conditions.

Nanocrystal synthesis variations. Yb^{3+}:$CsPbCl_3$ NCs of varying Yb^{3+} concentrations were synthesized following the protocol reported above except the nominal Yb^{3+} amount was varied using values of 0.02, 0.04, 0.08, 0.16, and 0.30 mmol $Yb(OAc)_3 \cdot xH_2O$. Reactions varying the Cs^+ content were also prepared following the protocol reported above except 140 μL, 200 μL, 280 μL, and 360 μL of 1M CsOAc in EtOH were added while the $Yb(OAc)_3 \cdot xH_2O$ concentration was held constant at 0.16 mmol. Synthesis of La^{3+}:$CsPbCl_3$ NCs also followed the above protocol, except the $Yb(OAc)_3 \cdot xH_2O$ was replaced with 0.16 mmol $La(OAc)_3 \cdot xH_2O$. We have noticed that analytical Yb^{3+} concentration often does not directly track the nominal Yb^{3+} concentration.

General characterization. Absorption spectra were taken with an Agilent Cary 60 spectrometer. Steady-state room-temperature photoluminescence (PL) data were measured using a 375 nm laser for excitation and a LN_2-cooled silicon CCD for detection. All spectra were corrected for instrument response. NC TEM images were obtained using an FEI TECNAI F20 microscope operating at 200 kV. Samples for TEM were prepared by dropcasting NC suspensions onto carbon-coated copper grids from TED Pella, Inc. Reported NC sizes reflect measurement of 300 individual nanocrystals in each case. Elemental composition was determined by inductively coupled plasma – atomic emission spectroscopy (ICP-AES, PerkinElmer 8300). Samples were prepared by digesting the NCs in concentrated nitric acid overnight with sonication. Powder X-ray diffraction was measured using a Bruker D8 Advance. Samples were prepared by dropcasting NC suspensions onto silicon substrates. Samples were irradiated using Cu Kα radiation (50000 mW).

Photoluminescence quantum yields (PLQY). Absolute photoluminescence quantum yield measurements were performed on dilute colloidal NC samples dispersed in hexane (OD < 0.2 at NC first exciton) placed in a sealed 1 cm path length quartz cuvette (Spectrocell) and positioned in a 5.3 inch teflon-based integrating sphere using a custom cuvette holder. The samples were directly excited with a 375 nm laser or Xe lamp, and attenuated with neutral density filters, as necessary. Excitation power was measured through a 1000 μm pinhole to calculate excitation flux. Light from the sphere was fiber coupled to a home-built fluorescence spectrometer using a LN_2-cooled silicon CCD for detection. All spectra were corrected for integrating sphere, fiber, lens, grating, and detector spectral response using a radiometric calibration lamp (Ocean Optics, LS-1-Cal). We confirmed and extended the emission correction curve generated using the calibrated lamp in the UV-Vis spectral region using secondary emission standards, as described in reference 26.[29] PLQY was calculated using:

$$PLQY = \frac{N_{em}}{N_{abs}} = \frac{\int I_{sample}(\lambda) - I_{ref}(\lambda) d\lambda}{\int E_{ref}(\lambda) - E_{sample}(\lambda) d\lambda} \quad (2.3)$$

where “I” indicates the spectrally corrected intensity of the emitted light, “E” indicates the spectrally corrected intensity of the excitation light, “sample” indicates measurements of NC samples, and “ref” indicates measurements of a reference cuvette containing neat hexane. We continuously calibrated our PLQY setup using well-characterized dye emission standards and

found good agreement with literature values: Rhodamine 6G – Measured (91.9%); Literature (90-92%).[30] IR140 – Measured (19.9%); Literature (20.0%).[31]

Transient-absorption (TA) spectroscopy. TA data were collected using an Ultrafast Systems Helios spectrometer. The light source consisted of a Coherent Libra amplified Ti:Sapphire laser operating at 1 kHz and 800 nm, with ~3.9 mJ maximum pulse energy and ~100 fs pulse width. Pump pulses (365 nm) were generated using a Coherent OPerA Solo Ultrafast optical parametric amplifier and passed through a 365nm +/- 10nm bandpass filter. Pump and probe beams were directed into the entrance ports of the Helios spectrometer, and the pump beam was attenuated using neutral density filters. Broadband probe pulses (350-850 nm) were generated by focusing the 800 nm pump beam onto a translating CaF_2 crystal. Time delays up to ~5.5 ns were achieved *via* an optical delay line. Colloidal NC samples dispersed in hexane (OD of approximately 0.2 at 365 nm) were placed in a sealed 2 mm path length quartz cuvette (Spectrocell) equipped with a teflon stirbar. During laser irradiation, samples were vigorously stirred and translated to prevent sample degradation/photocharging by ensuring a fresh sample population with each pump pulse such that scan-to-scan kinetics did not appreciably change with prolonged laser exposure. Without stirring/translation during laser exposure, we observed rapid degradation of the sample as observed by substantial changes in scan-to-scan kinetics, especially at early time delays, and eventual precipitation of the NCs from solution. All TA measurements were performed under conditions in which the laser pump fluence was tuned sufficiently low to produce, on average, less than a single exciton per NC per pulse ($0 < \langle N \rangle < 0.2$) with less than 2% probability of biexciton formation (see **Appendix 2.2**).

Time-resolved photoluminescence (TRPL) spectroscopy. Time-resolved excitonic photoluminescence was measured separately from the time-resolved near-IR (NIR) photoluminescence. For the excitonic luminescence, colloidal samples were prepared by dropcasting the nanocrystal solutions onto quartz substrates. To ensure thick and even films, the colloidal solutions were mixed in octane with a hexane-to-octane ratio of 8:1 v/v and several layers were added. The samples were loaded into a closed-cycle cryostat capable of cooling the sample to 20 K. Samples were irradiated with 355 nm light from the third harmonic of an Ekspla Nd:YAG laser firing at a repetition rate of 25 Hz. Luminescence was detected using a Hamamatsu streak camera, and measurements were performed using 20 ns and 200 ns measurement windows, which yield instrument response times of ~280 ps and 2.7 ns, respectively. Excitation of the sample was

performed at a right angle to the detection path with a maximum pump fluence of 10^{12} photons per cm^2 per pulse. Integration of the 200 ns streak camera images results in over 95% of emitted photons from the exciton. For time-resolved NIR luminescence, colloidal nanocrystals in hexane were irradiated with 405 nm light using 20 Hz square-wave pulses, and the NIR luminescence was detected using a silicon photodiode with a built-in amplifier and recorded with a Tektronix digital oscilloscope.

Average PL lifetimes (τ_{avg}) were determined by fitting the PL decay traces to a biexponential function in which the PL intensity, I(t), is

$$\mathrm{I(t)} = A_1 e^{-(\frac{t}{\tau_1})} + A_2 e^{-(\frac{t}{\tau_2})} \tag{2.4}$$

where A_n denotes the amplitude of each time component, τ_n. The weighted average of the time components, τ_{avg}, is then given by the following equation:

$$\tau_{avg} = \frac{\Sigma A_n \tau_n^2}{\Sigma A_n \tau_n} \tag{2.5}$$

Variable-temperature absorption spectroscopy. Colloidal NCs were dropcasted onto sapphire discs, loaded into a helium flow cryostat, and cooled to 12 K. Absorption spectra were measured at various temperatures between 12 K and room temperature using an Agilent Cary 5000 UV-Vis-NIR spectrometer.

Variable-temperature photoluminescence (VTPL). Colloidal NCs were dropcasted onto quartz discs, loaded into a liquid helium cooled cryostat, and cooled to 5 K. PL spectra were measured at various temperatures between 5 and 265 K using CW 375 nm light from an LED. All spectra were corrected for the wavelength dependent instrument response.

2.8 Acknowledgments

The following people are acknowledged for their contribution to this chapter: Daniel Kroupa for acquiring the dynamics data, PLQYs, and illustrating the figures; Daniel Gamelin for supervising the entirety of the project.

This research was supported by the U.S. National Science Foundation (DMR-1505901 to D.R.G.), and by the State of Washington through the University of Washington Clean Energy Institute (to T.J.M.), including *via* funding from the Washington Research Foundation (to D.M.K.).

This research was partially supported by the U.S. National Science Foundation through the University of Washington Molecular Engineering Materials Center, a Materials Research Science and Engineering Center (DMR-1719797). Part of this work was conducted at the Molecular Analysis Facility, a National Nanotechnology Coordinated Infrastructure site at the University of Washington which is supported in part by the National Science Foundation (grant ECC-1542101), the University of Washington, the Molecular Engineering & Sciences Institute, the Clean Energy Institute, and the National Institutes of Health. Michael De Siena is acknowledged for acquiring the TEM images. Dr. Sidney Creutz is acknowledged for helpful discussion.

References

1. Protesescu, L.; Yakunin, S.; Bodnarchuk, M. I.; Krieg, F.; Caputo, R.; Hendon, C. H.; Yang, R. X.; Walsh, A.; Kovalenko, M. V., *Nano Lett.* **2015,** *15*, 3692-3696.
2. Nedelcu, G.; Protesescu, L.; Yakunin, S.; Bodnarchuk, M. I.; Grotevent, M. J.; Kovalenko, M. V., *Nano Lett.* **2015,** *15*, 5635-5640.
3. Protesescu, L.; Yakunin, S.; Kumar, S.; Bär, J.; Bertolotti, F.; Masciocchi, N.; Guagliardi, A.; Grotevent, M.; Shorubalko, I.; Bodnarchuk, M. I.; Shih, C.-J.; Kovalenko, M. V., *ACS Nano* **2017,** *11*, 3119-3134.
4. Zhang, F.; Zhong, H.; Chen, C.; Wu, X.-g.; Hu, X.; Huang, H.; Han, J.; Zou, B.; Dong, Y., *ACS Nano* **2015,** *9*, 4533-4542.
5. Swarnkar, A.; Marshall, A. R.; Sanehira, E. M.; Chernomordik, B. D.; Moore, D. T.; Christians, J. A.; Chakrabarti, T.; Luther, J. M., *Science* **2016,** *354*, 92.
6. Kim, Y.-H.; Wolf, C.; Kim, Y.-T.; Cho, H.; Kwon, W.; Do, S.; Sadhanala, A.; Park, C. G.; Rhee, S.-W.; Im, S. H.; Friend, R. H.; Lee, T.-W., *ACS Nano* **2017,** *11*, 6586-6593.
7. Liu, W.; Lin, Q.; Li, H.; Wu, K.; Robel, I.; Pietryga, J. M.; Klimov, V. I., *J. Am. Chem. Soc.* **2016,** *138*, 14954-14961.
8. Parobek, D.; Roman, B. J.; Dong, Y.; Jin, H.; Lee, E.; Sheldon, M.; Son, D. H., *Nano Lett.* **2016,** *16*, 7376-7380.
9. Yuan, X.; Ji, S.; De Siena, M. C.; Fei, L.; Zhao, Z.; Wang, Y.; Li, H.; Zhao, J.; Gamelin, D. R., *Chem. Mater.* **2017,** *29*, 8003-8011.
10. Zhou, D.; Liu, D.; Pan, G.; Chen, X.; Li, D.; Xu, W.; Bai, X.; Song, H., *Adv. Mater.* **2017**, 1704149.
11. Pan, G.; Bai, X.; Yang, D.; Chen, X.; Jing, P.; Qu, S.; Zhang, L.; Zhou, D.; Zhu, J.; Xu, W.; Dong, B.; Song, H., *Nano Lett.* **2017,** *17*, 8005-8011.
12. Meijer, J.-M.; Aarts, L.; van der Ende, B. M.; Vlugt, T. J. H.; Meijerink, A., *Phys. Rev. B* **2010,** *81*, 035107.
13. Erickson, C. S.; Bradshaw, L. R.; McDowall, S.; Gilbertson, J. D.; Gamelin, D. R.; Patrick, D. L., *ACS Nano* **2014,** *8*, 3461-3467.
14. Creutz, S. E.; Fainblat, R.; Kim, Y.; De Siena, M. C.; Gamelin, D. R., *J. Am. Chem. Soc.* **2017,** *139*, 11814-11824.
15. van der Ende, B. M.; Aarts, L.; Meijerink, A., *Phys. Chem. Chem. Phys.* **2009,** *11*, 11081-11095.

16. Martín-Rodríguez, R.; Geitenbeek, R.; Meijerink, A., *J. Am. Chem. Soc.* **2013,** *135*, 13668-13671.
17. van der Ende, B. M.; Aarts, L.; Meijerink, A., *Adv. Mat.* **2009,** *21*, 3073-3077.
18. Liu, L.; Li, M.; Cai, S.; Yang, Y.; Mai, Y., *Opt. Mater. Express* **2015,** *5*, 756-763.
19. Creutz, S. E.; Crites, E. N.; De Siena, M. C.; Gamelin, D. R., *Nano Lett.* **2018,** *18*, 1118-1123.
20. Imran, M.; Caligiuri, V.; Wang, M.; Goldoni, L.; Prato, M.; Krahne, R.; De Trizio, L.; Manna, L., *J. Am. Chem. Soc.* **2018,** *140*, 2656-2664.
21. Krieg, F.; Ochsenbein, S. T.; Yakunin, S.; ten Brinck, S.; Aellen, P.; Süess, A.; Clerc, B.; Guggisberg, D.; Nazarenko, O.; Shynkarenko, Y.; Kumar, S.; Shih, C.-J.; Infante, I.; Kovalenko, M. V., *ACS Energy Lett.* **2018,** *3*, 641-646.
22. Dang, Z.; Shamsi, J.; Palazon, F.; Imran, M.; Akkerman, Q. A.; Park, S.; Bertoni, G.; Prato, M.; Brescia, R.; Manna, L., *ACS Nano* **2017,** *11*, 2124-2132.
23. Wu, K.; Liang, G.; Shang, Q.; Ren, Y.; Kong, D.; Lian, T., *J. Am. Chem. Soc.* **2015,** *137*, 12792-12795.
24. Xu, K.; Lin, C. C.; Xie, X.; Meijerink, A., *Chem. Mater.* **2017,** *29*, 4265-4272.
25. Watanabe, K.; Koshimizu, M.; Yanagida, T.; Fujimoto, Y.; Asai, K., *Jpn. J. Appl. Phys.* **2016,** *55*, 02BC20.
26. Kang, J.; Wang, L.-W., *J Phys. Chem. Lett.* **2017,** *8*, 489-493.
27. Henling, L. M.; McPherson, G. L., *Phys. Rev. B* **1977,** *16*, 4756-4760.
28. McPherson, G. L.; Henling, L. M., *Phys. Rev. B* **1977,** *16*, 1889-1892.
29. Gardecki, J. A.; Maroncelli, M., *Appl. Spectrosc.* **1998,** *52*, 1179-1189.
30. Würth, C.; González, M. G.; Niessner, R.; Panne, U.; Haisch, C.; Genger, U. R., *Talanta* **2012,** *90*, 30-37.
31. Hatami, S.; Wurth, C.; Kaiser, M.; Leubner, S.; Gabriel, S.; Bahrig, L.; Lesnyak, V.; Pauli, J.; Gaponik, N.; Eychmuller, A.; Resch-Genger, U., *Nanoscale* **2015,** *7*, 133-143.

2.9 Appendices

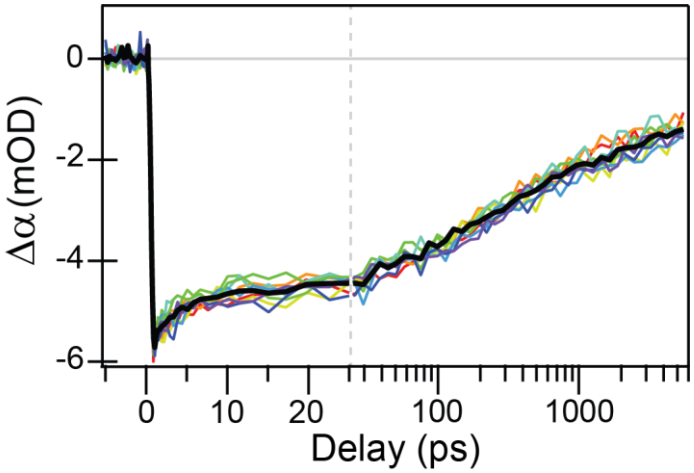

Appendix 2.1. TA kinetics of individual scans all-scan average. These data highlight the low scan-to-scan variability upon vigorous stirring and translation of colloidal $CsPbCl_3$ NC samples upon exposure to 365 nm laser excitation. (colored: individual scans, black: all-scan average).

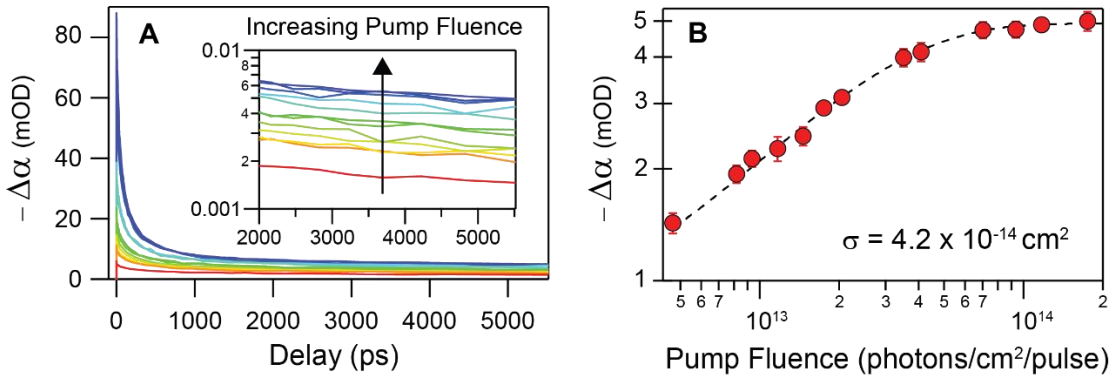

Appendix 2.2. Fluence-dependent TA measurements. (**A**) Fluence-dependent TA kinetics for undoped $CsPbCl_3$ NCs upon 365 nm laser excitation. Inset shows the late-time TA kinetics. (**B**) Late-time TA kinetics at 5500 ps extracted from a linear fit of the data from 2000-5500 ps as a function of laser pump fluence. The data are fit to extract an absorption cross section of 4.2 x 10^{-14} cm^2.

We performed a laser fluence-dependent TA experiment to determine the absorption cross section, σ, of undoped $CsPbCl_3$ NCs. We monitored the late time delay TA signal (2000-5500 ps; after complete decay of multiexciton signal) as it should scale with σ and saturate with increasing laser pump fluence following Poisson statistics. Here, the probability of generating i photons per NC is given by

$$p_i = \frac{\langle N \rangle^i}{i!} e^{-\langle N \rangle} \qquad \text{(App. 2.1)}$$

where $\langle N \rangle$ is the average number of excitons per NC. Thus, the late time TA kinetic signal as a function of laser fluence can be modeled with

$$-\Delta\alpha(t \gg \tau_{xx}) \propto (1 - p_0) = 1 - e^{-\langle N \rangle} \qquad \text{(App. 2.2)}$$

where τ_{xx} is the multiexciton lifetime. $\langle N \rangle$ can be expressed as $\langle N \rangle = \sigma j_p$ where j_p is the laser pump fluence, which can be calculated from the measured laser power at the sample position. Based on the fit to our data, we calculate an absorption cross section of 4.2 x 10^{-14} cm^2 for the undoped $CsPbCl_3$ NCs.

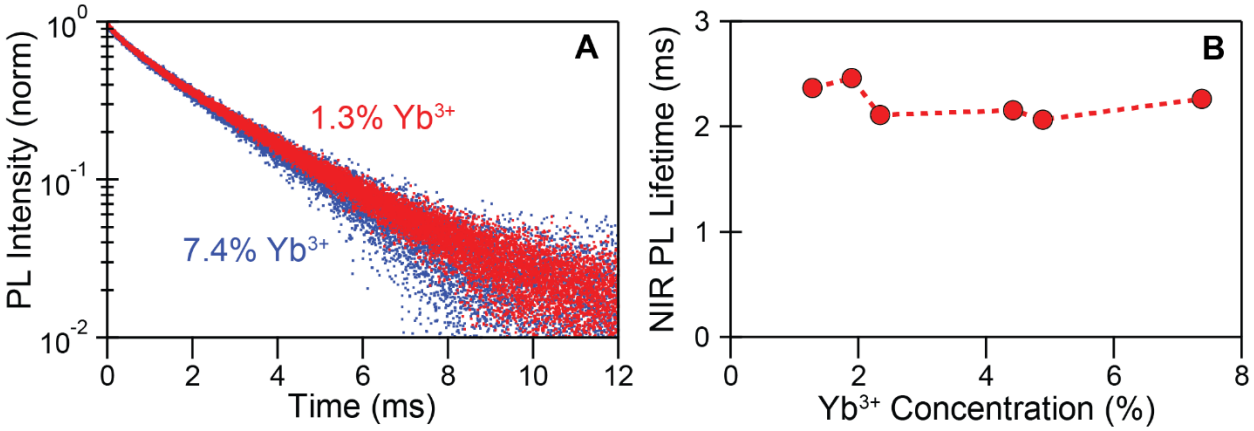

Appendix 2.3. Room temperature Yb^{3+} PL lifetimes. (**A**) Room-temperature time-resolved PL of the NIR emission for (red) 1.3% Yb^{3+} and (blue) 7.4% Yb^{3+}:$CsPbCl_3$ NCs. (**B**) Average NIR PL lifetime, τ_{avg}, as a function of Yb^{3+} concentration.

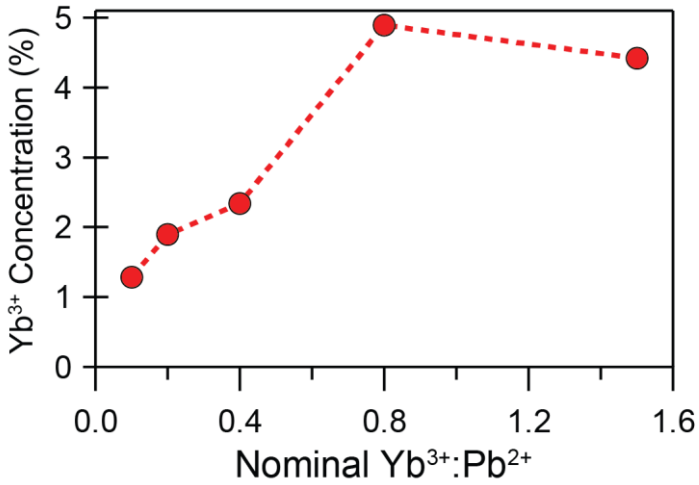

Appendix 2.4. Yb^{3+} doping concentration as a function of varying nominal Yb^{3+}:Pb^{2+}. Analytical Yb^{3+} concentration plotted versus the nominal Yb^{3+}:Pb^{2+} ratio used in the NC synthesis.

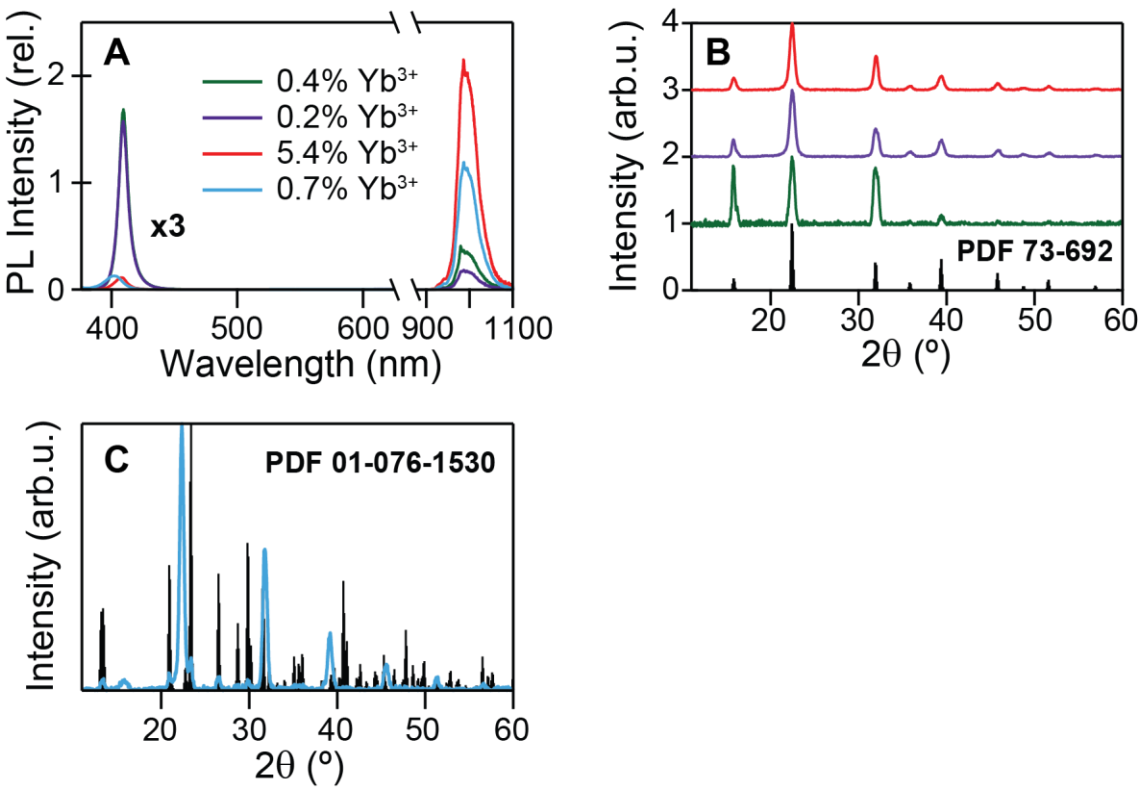

Appendix 2.5. **Effect of increasing nominal [Cs^+].** (**A**) Steady-state PL of samples in using Cs^+:Pb^{2+} nominal ratios of 0.6 (green) 1.0 (purple) and 1.4 (red) and 1.8 (blue) with a fixed Yb^{3+}:Pb^{2+} ratio of 0.2. Excitonic emission is magnified 6x for clarity. (**B**) XRD data of the corresponding samples against $CsPbCl_3$ reference. (**C**) XRD data of sample made with nominal [Cs^+]:[Pb^{2+}] of 1.8 shown with Cs_4PbCl_6 reference. The resulting excitonic emission and final [Yb^{3+}] is highly sensitive to the initial amount of Cs^+ present in the reaction mixture. Interestingly, most synthetic protocols using Cs-oleate for hot injection call for a Cs^+:Pb^{2+} nominal ratio of ~0.25. However, Yb^{3+} incorporation is only high when the nominal ratio is above 1.0 and appears optimal at 1.4 for this reaction scheme. At a certain point, too much Cs^+ (ratio of 1.8) results in the impurity Cs_4PbCl_6 composition.

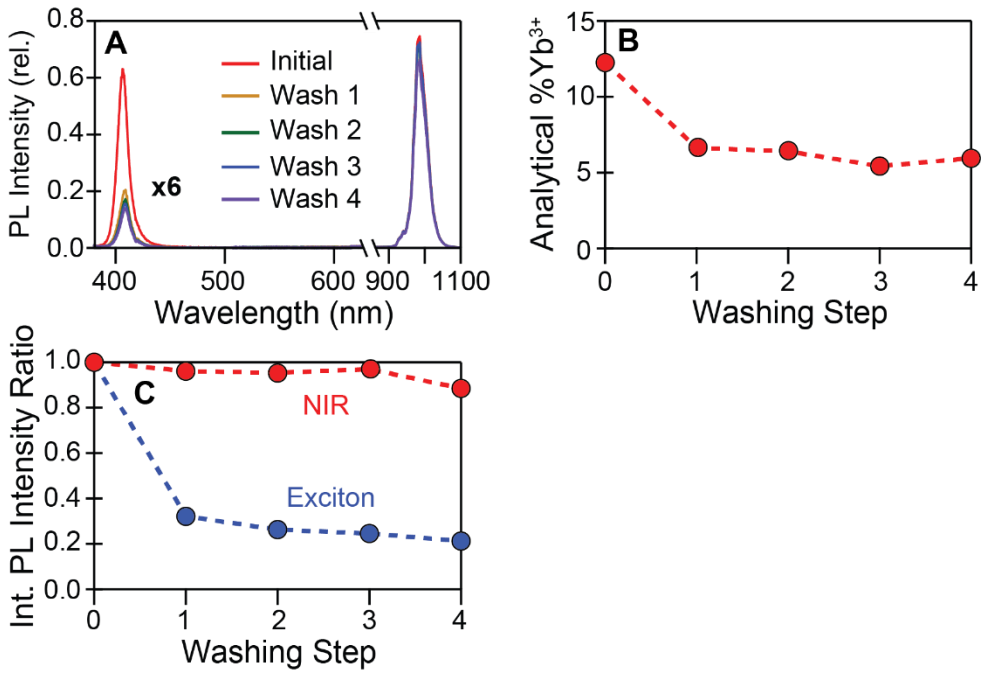

Appendix 2.6. Effect of excessive washing on exciton and Yb^{3+} PL. (**A**) Steady-state PL of the same sample before and after each washing step. Exciton is magnified 6x for clarity. All spectra are corrected and absorbance normalized. (**B**) The analytical Yb^{3+} concentration with respect to the number of washes. (**C**) Scatter plot of the integrated PL ratio of the NIR (red) and excitonic (blue) emission respective to their initial value. We show that only one washing step is necessary to remove excess unreacted material such as metal oleates that could cause an overestimation of composition by elemental analysis. The washing steps largely affect the excitonic emission (~70% loss) while the NIR emission remains as high as 90% of its initial value even after 4 washing cycles with ethyl acetate.

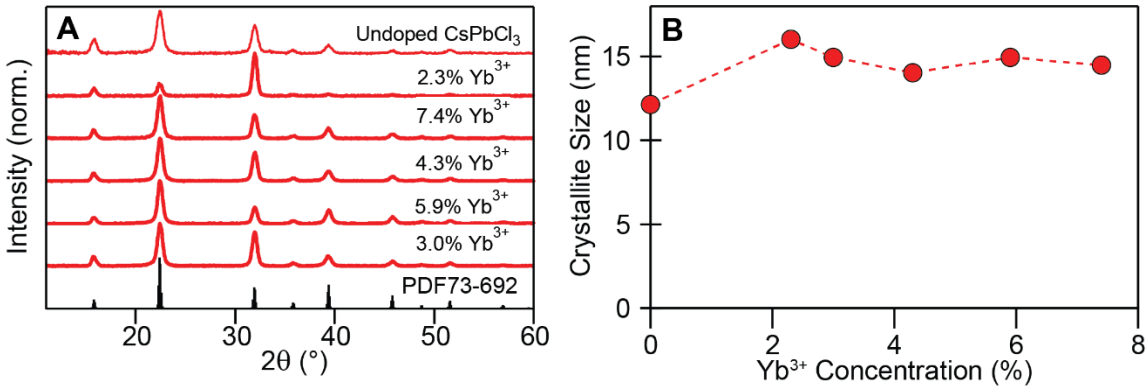

Appendix 2.7. XRD of $CsPb_{1-x}Yb_xCl_3$. (**A**) XRD data of samples (red) from Figure 2.2a and reference $CsPbCl_3$ NCs (black) arranged in order of increasing Yb^{3+}:Pb^{2+} nominal ratios (0.1, 0.2, 0.4, 0.8, 1.5) from bottom to top. Data from undoped $CsPbCl_3$ NCs are also shown. (**B**) Results from Scherrer size analysis of Yb^{3+}-doped and undoped $CsPbCl_3$ NCs.

For each sample, the effective crystallite size, ε, was determined using the Scherrer equation

$$\varepsilon = \frac{K\lambda}{\beta cos(\theta)} \quad \text{(App. 2.3)}$$

in which K is the shape factor (0.94), λ is the X-ray wavelength (0.15406 nm), β is the FWHM of the measured reflection (2θ = 22.4°), and θ is the Bragg angle.

Transient Absorption Spectroscopy - Kinetic Model. Wu *et al.* studied charge-transfer kinetics from colloidal $CsPbBr_3$ NCs to small, surface-bound molecular species.[6] They showed that high $CsPbBr_3$ NC PL QYs (~80%) could be attributed to negligible carrier trapping pathways with ~94% of lowest excitonic states decaying with a single exponential lifetime of 4.5 ns. Additionally, they showed that the occupancy of both band-edge electrons and holes contribute to the NC exciton bleach signal, with 67.2% and 32.8% contribution, respectively. Even though the calculated effective masses of the electron and hole are similar, they hypothesize that the greater exciton bleach contribution from the electron could be due to higher degeneracy in the valence band. They fit their kinetic data to a sum of exponentials weighted by bleach signal carrier contribution for electron/hole transfer and subsequent cross relaxation between the carrier transferred to surface anchored molecular species and the remaining carrier delocalized at the NC band edge. Additionally, they propose that because charge transfer to surface bound molecular species is extremely efficient, at sufficiently high dye loading, band-to-band exciton recombination does not need to be included in the model. Overall, their kinetic fitting routine nicely models their experimental data. Considering $CsPbBr_3$ and $CsPbCl_3$ have similar electronic structures/carrier effective masses,[5] we made the assumption that the contribution of electron and hole occupancy to the measured TA exciton bleach kinetics experimentally determined for $CsPbBr_3$ NCs would be similar for $CsPbCl_3$ NCs.

As-synthesized $CsPbCl_3$ NCs typically show much lower PLQYs than the other lead halide perovskite NCs, presumably due to more efficient nonradiative recombination pathways at lattice or surface defects. Therefore, we can treat these carrier trap states in a similar way that Wu *et al.* treated charge transfer species using a sum of exponentials, including carrier trapping and corresponding cross relaxation. However, we also observe exciton PL from these NCs, so we must include a fifth exponential term to account for band-edge radiative recombination. The possible

excited state carrier recombination pathways present in undoped $CsPbCl_3$ NCs are summarized in **Appendix Scheme 1**. Upon photoexcitation, both holes and electrons rapidly localize to available trap states with rates of k_1 and k_2, respectively (sub-ps to 10's of ps). These trapped carriers can recombine with delocalized band edge carriers with rates of k_4 and k_5 (10's – 100's of ps). Finally, electrons and holes that reside in a subset of the NC ensemble that do not exhibit active trap pathways can undergo band-to-band recombination with a rate of k_6 (typically nanoseconds for $CsPbX_3$ NCs).

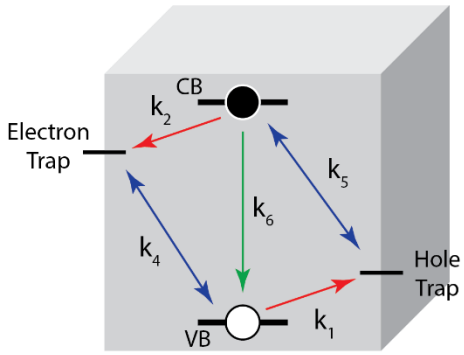

Appendix Scheme 2.1. Possible excited state recombination pathways present in undoped $CsPbCl_3$ NCs.

Using a sum of five exponentials – of which the sum of two decay amplitudes is weighted by 0.33 (0.67) for hole (electron) trapping and corresponding cross-relaxation - we fit the undoped $CsPbCl_3$ NC TA kinetics allowing all of the exponential time constants to vary. We found good agreement with the experimental data (**Appendix 2.5**). Fit parameters are summarized in **Appendix Table 2.1**.

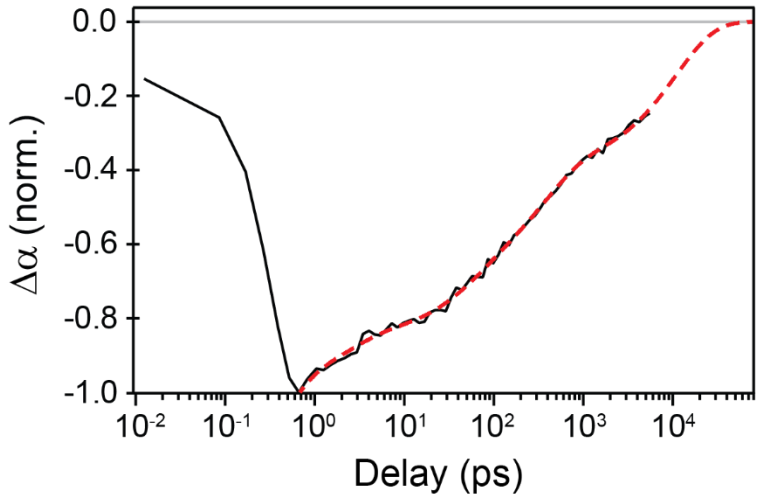

Appendix 2.8. TA kinetics of undoped $CsPbCl_3$ NCs. Raw data (black) and resulting fit to a sum of five exponentials (dashed red).

Next, we wanted to see if there were any components in the TA kinetics of the Yb^{3+} doped NCs that differed from the undoped NCs. Because all of the samples exhibited some degree of exciton PL, we first tested the theory that the kinetics at long pump-probe delays should be similar. Upon normalizing at long delays, it became evident that the interband recombination lifetime of the NCs shortened with increasing Yb^{3+} content (kinetics at long delays did not overlap). After normalizing the kinetics at intermediate delays (trapped carrier cross-relaxation timescales; 50-150 ps), the overlap was much better and the undoped response was subtracted away from the doped response; therefore, the remaining response should be due only to carrier recombination pathways associated with Yb^{3+} incorporation. The Yb^{3+}-related kinetic response fit nicely to a sum of two exponentials with time constants of ~0.3 ps and 8.4 ps (**Appendix 2.6**).

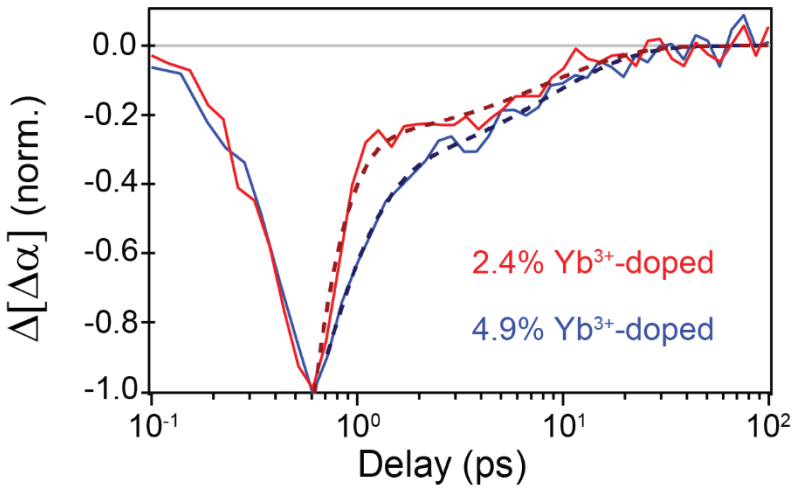

Appendix 2.9. Normalized TA Kinetics. Representative TA kinetic response of two Yb^{3+} doped $CsPbCl_3$ NC samples after normalizing at intermediate delays (50-150 ps) and subtracting away response from undoped NCs. The resulting fits (dashed) are a sum of two exponential decay functions.

The fast time component (~0.3 ps) is similar to the native hole trapping time constant, τ_1, found in the undoped NCs, but the longer time constant (8.4 ps), denoted as τ_3, is not an obvious component of the undoped NC exciton recombination kinetics. Regardless, the timescales of these decays suggests that Yb^{3+} incorporation introduces new carrier recombination pathways, the identity of which is discussed in detail in the main text. We performed a global fit of all the Yb^{3+}:$CsPbCl_3$ NC TA kinetics, normalized to 1 at early pump-probe delay, using a sum of six exponentials. Time constants τ_1, τ_2, τ_3, τ_4, and τ_5 were held constant and τ_6 was allowed to float. The decay amplitudes were also allowed to float. The result of the global fit to the TA data is shown in **Figure 2.4C** of the main text, and the best-fit parameters are recorded in **Appendix Table 2.1**.

Appendix Table 2.1. TA kinetic global-fitting time constants and amplitudes for undoped and Yb^{3+}-doped $CsPbCl_3$ NCs.

Table S1	*τ_1=0.3 ps*	*τ_2=2 ps*	*τ_3=8.4 ps*	*τ_4=49.85 ps*	*τ_5=355.09 ps*		
Sample ID	**A_1**	**A_2**	**A_3**	**A_4**	**A_5**	**A_6**	**τ_6 (ps)**
Undoped	-0.0576	-0.11462	N/A	-0.14922	-0.30903	-0.3899	10907
1.3% Yb^{3+}	-0.06640	-0.12402	-0.09972	-0.1789	-0.27476	-0.26523	6263.5
1.9% Yb^{3+}	-0.03760	-0.14848	-0.10606	-0.14535	-0.33632	-0.22977	7616.6
2.4% Yb^{3+}	-0.04253	-0.11794	-0.1178	-0.11898	-0.35048	-0.2488	8416.1
4.4% Yb^{3+}	-0.10061	-0.19403	-0.19403	-0.22573	-0.17669	-0.20894	3635.4
4.9% Yb^{3+}	-0.16074	-0.19735	-0.12373	-0.14646	-0.23593	-0.19089	4500.1
6.0% Yb^{3+}	-0.15600	-0.29181	-0.22541	-0.12782	-0.14627	-0.06299	1760.2

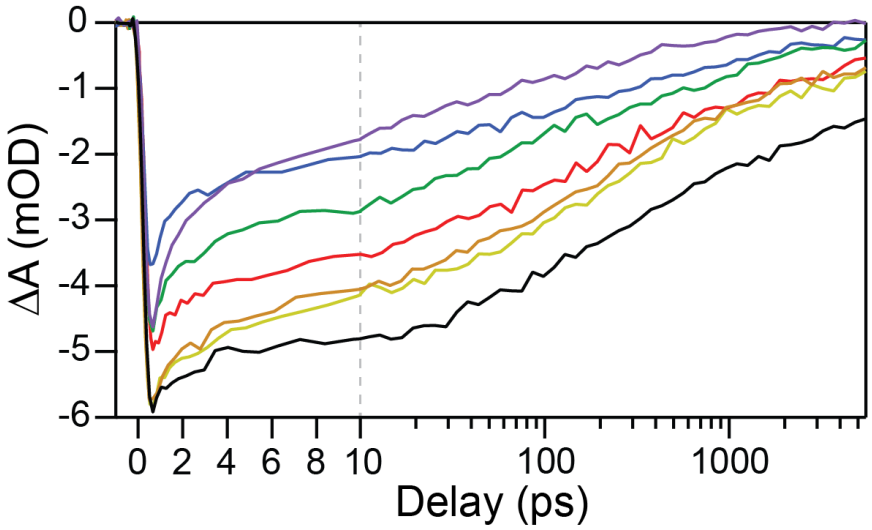

Appendix 2.10. **Raw TA kinetic data.** Averaged scans over the FWHM of the first exciton peak bleach for undoped (black) and Yb^{3+}-doped (colored; colors consistent with Figure 4) $CsPbCl_3$ NCs dispersed in hexane.

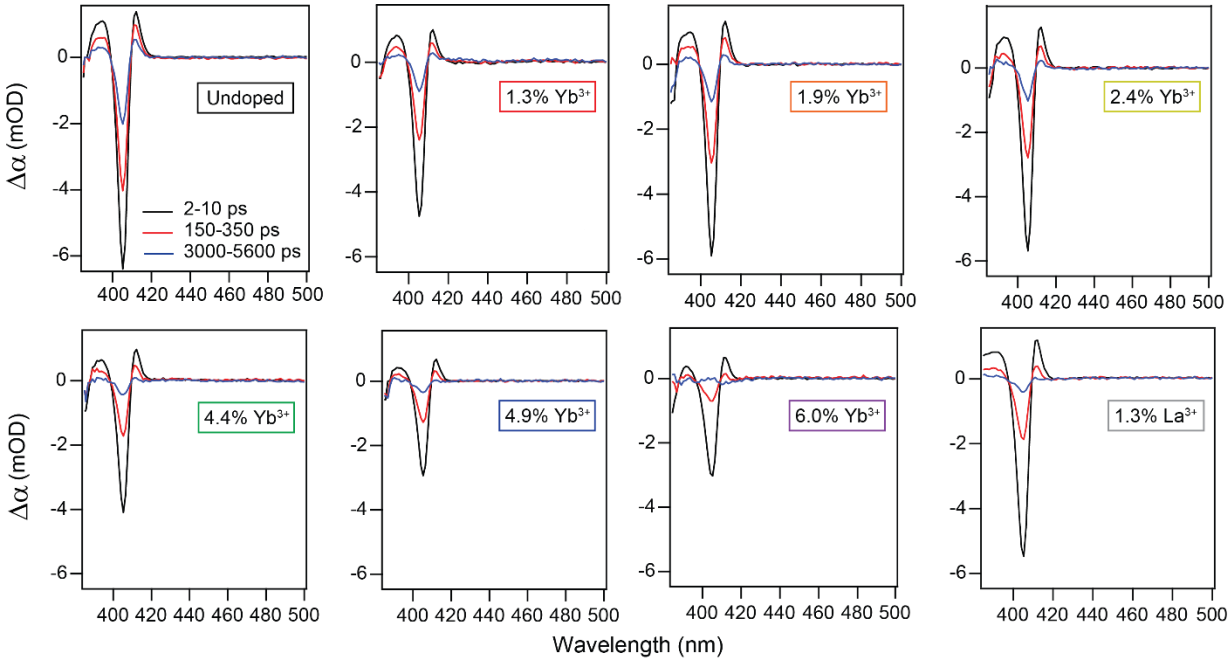

Appendix 2.11. **TA spectra of Yb^{3+}-doped and La^{3+}-doped NCs.** Varying TA spectra according to probe delay for undoped, Yb^{3+}-doped, and La^{3+}-doped $CsPbCl_3$ NC colloids dispersed in hexane for delays between 2-10 ps (black), 150-350 ps (red), and 3000-5600 ps (blue).

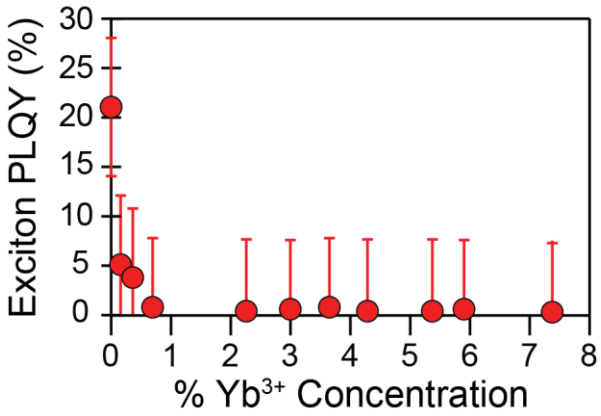

Appendix 2.12. **Exciton PLQYs plotted as a function of Yb^{3+} concentration**. From Figure 2.2B of the main text but plotted here on an expanded *y* scale.

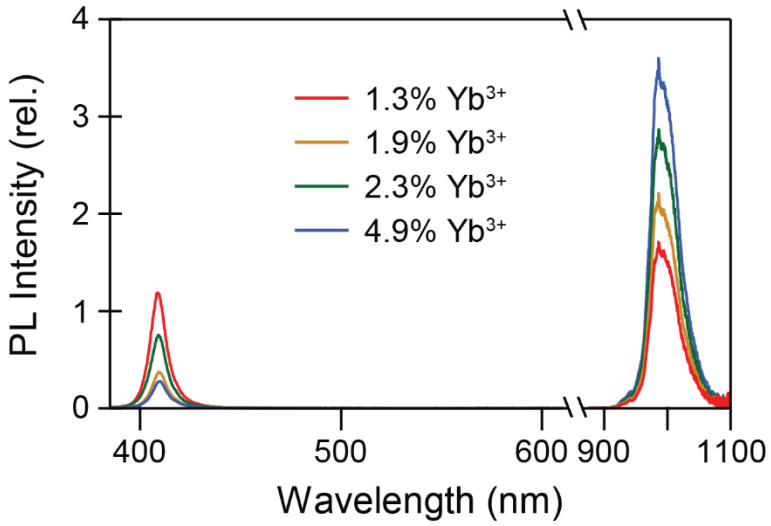

Appendix 2.13. PL spectra of $CsPb_{1-x}Yb_xCl_3$ NCs..Steady-state PL spectra of Yb^{3+}:$CsPbCl_3$ NCs used in Figure 2.4. Samples were irradiated with 375 nm light. Note: 6.0% Yb^{3+}:$CsPbCl_3$ is shown in Figure 2.1e.

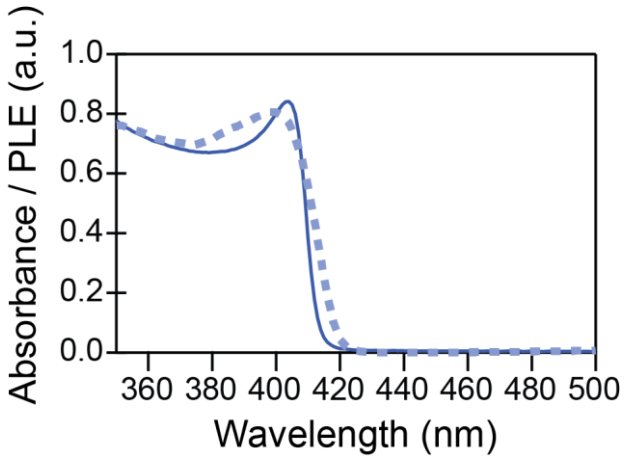

Appendix 2.14. **PLE of NIR emission.** Absorption (solid) and photoluminescence excitation (dashed; λ_{em} = 980 nm) spectra of 5.2% Yb^{3+}-doped $CsPbCl_3$ NCs, collected at room temperature.

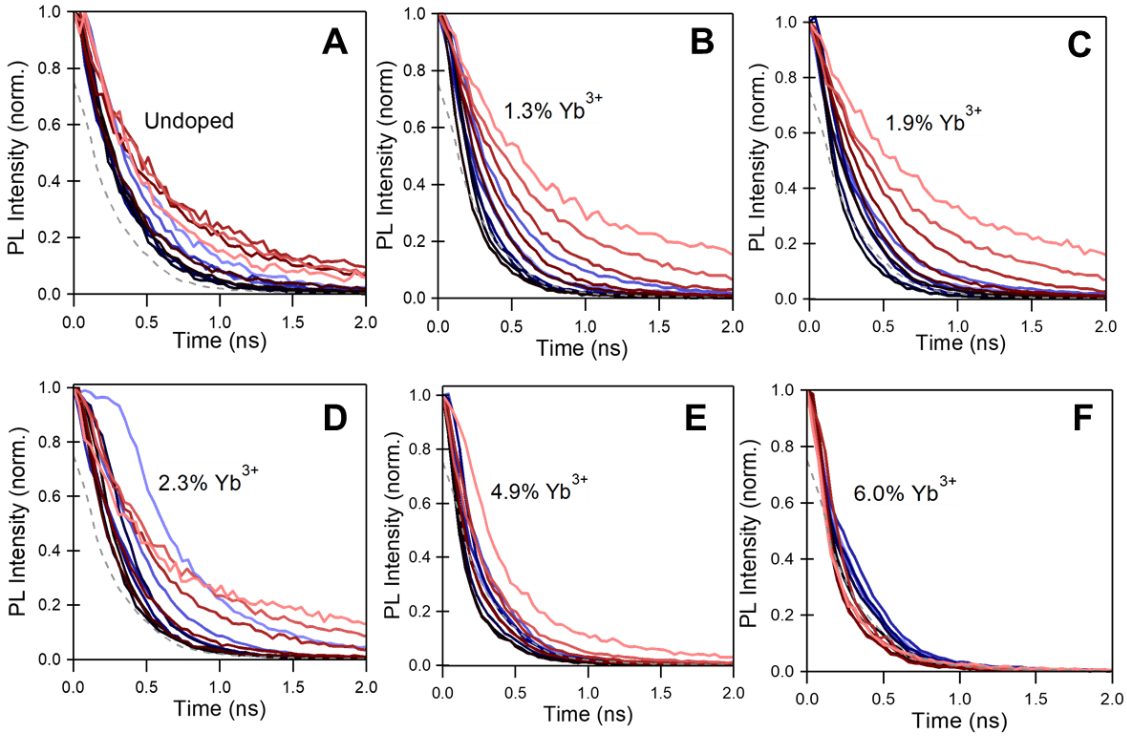

Appendix 2.15. **Temperature dependent PL decay of exciton luminescence**. Time-resolved PL decay traces of (**A**) undoped, (**B**) 1.3% Yb^{3+}, (**C**) 1.9% Yb^{3+}, (**D**) 2.4% Yb^{3+}, (**E**) 5.1% Yb^{3+}, and (**F**) 6.3% Yb^{3+}-doped $CsPbCl_3$ nanocrystals at various temperatures. The temperature range is 20 K (light blue) to 300 K (pink). The instrument response function is shown as the dashed grey line.

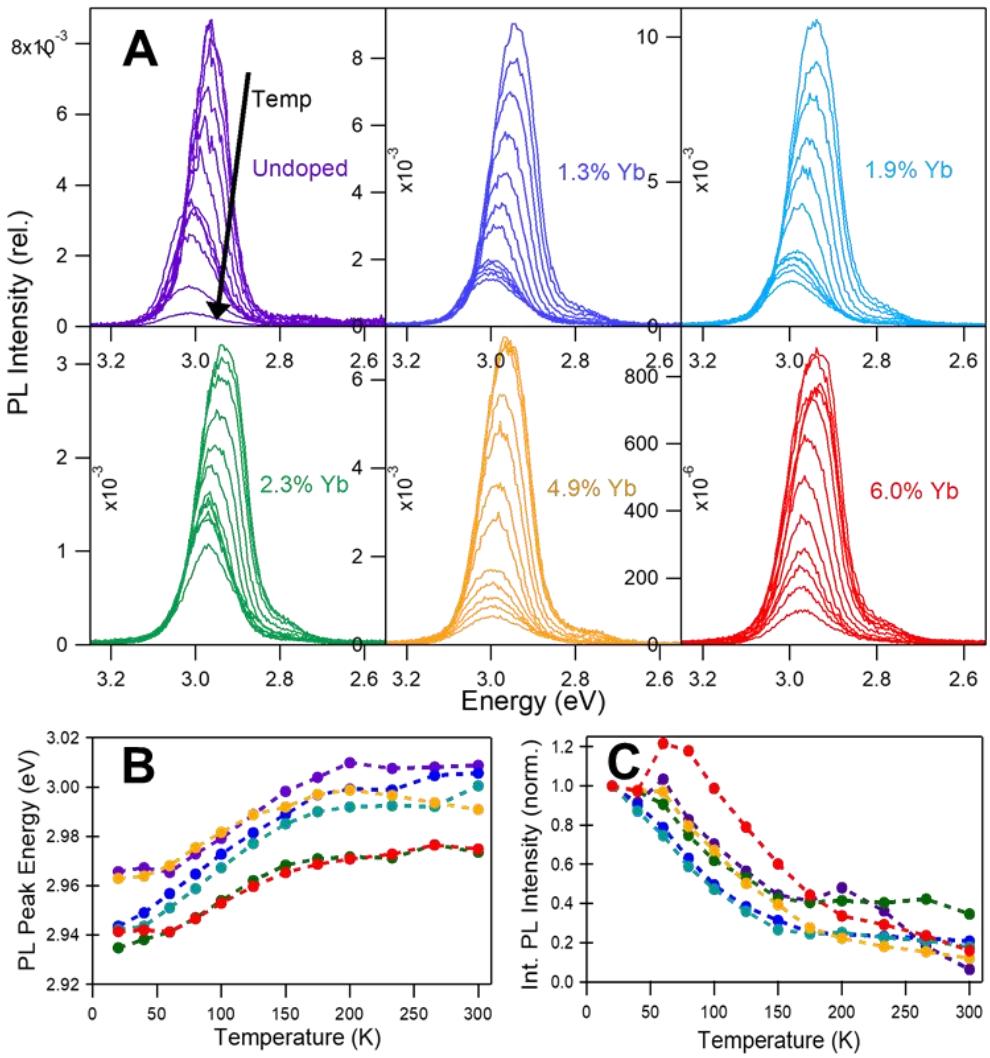

Appendix 2.16. **Variable Temperature Excitonic PL.** (**A**) Raw data of temperature dependent excitonic PL under 355 nm irradiation at temperatures from 20 to 300 K. (**B**) Peak energy and (**C**) normalized integrated intensity as a function of temperature. The colors match the corresponding samples from panel **A**.

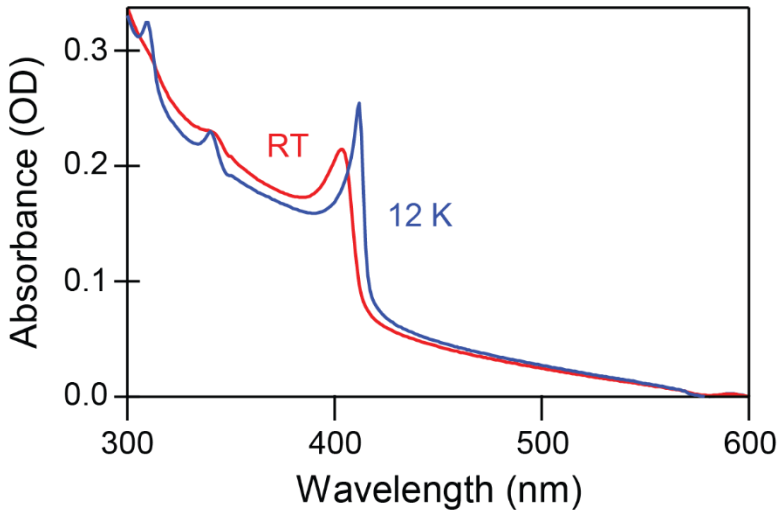

Appendix 2.17. Temperature-dependent absorption spectra. Low-temperature (blue) and room-temperature (red) absorption spectra of ~7% Yb^{3+}:$CsPbCl_3$ NCs.

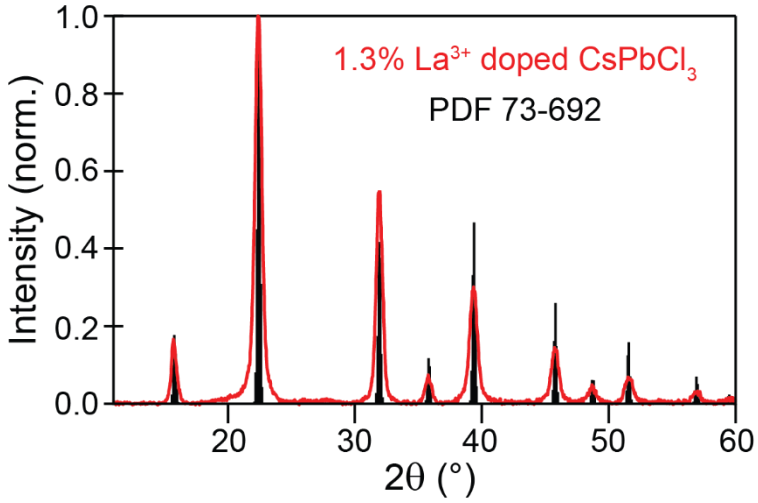

Appendix 2.18. **La^{3+}:$CsPbCl_3$ XRD.** X-ray diffraction data of 1.3% La^{3+}:$CsPbCl_3$ NCs compared to reference $CsPbCl_3$.

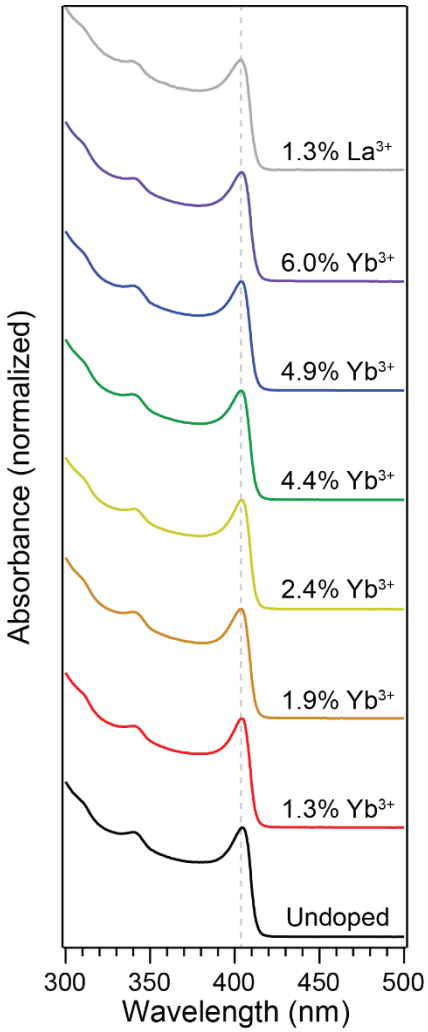

Appendix 2.19. **Room-temperature $CsPb_{1-x}Yb_xCl_3$ absorption spectra.** Ground state optical absorption spectra of undoped, Yb^{3+}-doped, and La^{3+}-doped $CsPbCl_3$ NC colloids dispersed in hexane.

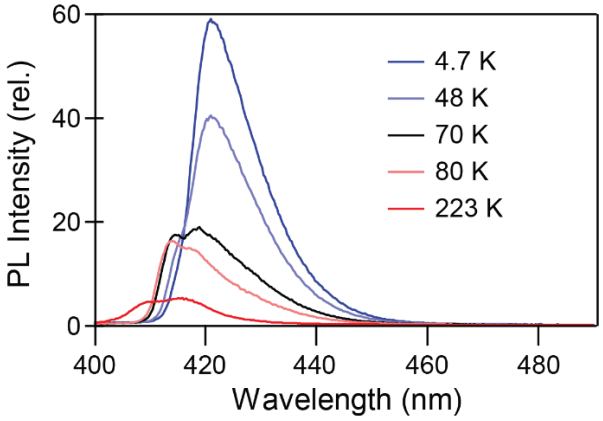

Appendix 2.20. **Induced-defect state PL.** Variable-temperature photoluminescence spectra of La^{3+}-doped $CsPbCl_3$ NCs.

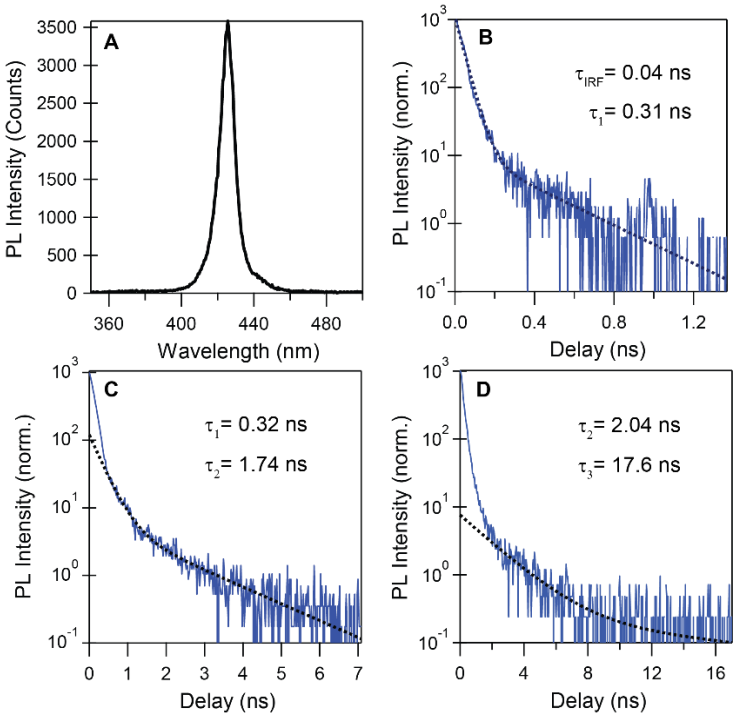

Appendix 2.21. **Low-Temperature, 20 K, PL decay of induced-defect luminescence**. (**A**) Low temperature PL spectra collected for 1.3% La^{3+}-doped $CsPbCl_3$ NCs. (**B**) Short- (**C**) medium-, and (**D**) long- time windows for PL decay from a shallow trap carrier. 99% of the emission occurs within the 40 ps instrument response of our detector, and the remaining emission is tri-exponential with time constants of ~ 0.3 ns, 1.9 ns, and 18 ns.

Chapter 3 Anion Exchange and the Quantum-Cutting Energy Threshold

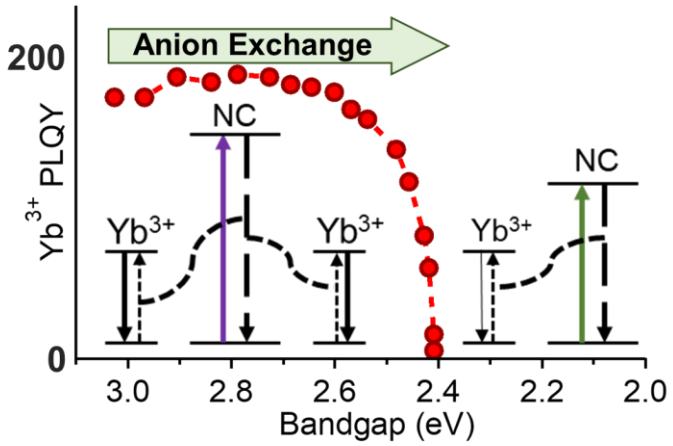

Abstract. Colloidal halide perovskite nanocrystals of $CsPbCl_3$ doped with Yb^{3+} have demonstrated remarkably high sensitized photoluminescence quantum yields (PLQYs), approaching 200%, attributed to a picosecond quantum-cutting process in which one photon absorbed by the nanocrystal generates two photons emitted by the Yb^{3+} dopants. This quantum-cutting process is thought to involve a charge-neutral defect cluster within the nanocrystal's internal volume. Here, we demonstrate that Yb^{3+}-doped $CsPbCl_3$ nanocrystals can be converted post-synthetically to Yb^{3+}-doped $CsPb(Cl_{1-x}Br_x)_3$ nanocrystals without compromising the desired high PLQYs. Nanocrystal energy gaps can be tuned continuously from E_g ~ 3.06 eV (405 nm) in $CsPbCl_3$ down to E_g ~ 2.53 eV (~490 nm) in $CsPb(Cl_{0.25}Br_{0.75})_3$ while retaining a constant PLQY above 100%. Reducing E_g further causes a rapid drop in PLQY, interpreted as reflecting an energy threshold for quantum cutting at approximately twice the energy of the Yb^{3+} $^2F_{7/2} \rightarrow {}^2F_{5/2}$ absorption threshold. These data demonstrate that very high quantum-cutting energy efficiencies can be achieved in Yb^{3+}-doped $CsPb(Cl_{1-x}Br_x)_3$ nanocrystals, offering the possibility to circumvent thermalization losses in conventional solar technologies. The presence of water during anion exchange is found to have a deleterious effect on the Yb^{3+} PLQYs but does not affect the nanocrystal shapes, morphologies, or even reduce the excitonic PLQYs of analogous undoped $CsPb(Cl_{1-x}Br_x)_3$ nanocrystals. These results provide valuable information relevant to development and application of these unique materials for spectral-shifting solar energy conversion technologies.

3.1 Introduction

Nanocrystals (NCs) of the all-inorganic lead-halide perovskite semiconductors, $CsPbX_3$ ($X = Cl^-$, Br^-, I^-), have demonstrated attractive photophysical properties such as bandgap tunability throughout the visible, broad absorption with large absorption cross sections, narrow emission linewidths, near-unity photoluminescence quantum yields (PLQYs), and defect tolerance.[1-3] Consequently, these materials have generated intense interest for numerous optoelectronics, photovoltaics, and photodetection applications.[4-7] Impurity doping with cations such as Mn^{2+}, Zn^{2+}, Cd^{2+}, Sn^{2+}, and others has also been explored as an approach to tune these optoelectronic properties.[8-10] Mn^{2+}-doping has received particular attention for shifting the NC PL relative to its absorption, and this approach has yielded families of luminescent materials that may be useful for white-light generation or other novel applications.[11-16]

Recently, colloidal Yb^{3+}-doped $CsPb(Cl_{1-x}Br_x)_3$ NCs (Yb^{3+}:$CsPb(Cl_{1-x}Br_x)_3$) were demonstrated to show extraordinarily high PLQYs in the near-IR sensitized by photoexcitation of the $CsPb(Cl_{1-x}Br_x)_3$ host NC, reaching as high as ~170%.[17-19] These very high PLQYs have been attributed to an extremely efficient quantum-cutting process that converts the energy from one short-wavelength absorbed photon into the energies of multiple longer-wavelength emitted photons. The emissive $^2F_{5/2} \rightarrow {}^2F_{7/2}$ *f-f* transition of Yb^{3+} in $CsPb(Cl_{1-x}Br_x)_3$, at ~980 nm, is aligned very well with the peak energy-conversion efficiency of crystalline Si (c-Si) photovoltaics, suggesting promise for various solar spectral-conversion applications.[17, 20-22] Solar-energy conversion using quantum cutting has been investigated for many years with other lanthanide-containing luminescent materials,[20-21, 23-27] but Yb^{3+}:$CsPb(Cl_{1-x}Br_x)_3$ is the first material that combines highly efficient quantum cutting with absorption that is sufficiently strong and broad for practical solar applications.

Anion alloying can be used to reduce the energy gap (E_g) from ~3.05 eV (~405 nm) in $CsPbCl_3$ NCs to ~2.39 eV (~518 nm) in $CsPbBr_3$ NCs,[28-33] enabling absorption of a much greater fraction of the solar spectrum. In principle, however, a fundamental energy-conservation threshold of $E_g > 2xE_{f\text{-}f}$ must exist if quantum cutting is indeed responsible for Yb^{3+} PL sensitization in Yb^{3+}:$CsPb(Cl_{1-x}Br_x)_3$ NCs. From NIR PL data,[19] we expect this absorption threshold to occur at $E_{f\text{-}f}$ ~ 2.53 eV (~490 nm), but to date there has been no systematic investigation of the relationship between quantum cutting and E_g in such NCs. Quantum-cutting polycrystalline films of Yb^{3+}:$CsPb(Cl_{1-x}Br_x)_3$ with substantially larger grain volumes do indeed show much smaller

PLQYs in Yb^{3+}:$CsPbBr_3$ than in wider-gap compositions,[33] but only large step sizes along the halide composition parameter (x) were examined. The ability to finely tune the Yb^{3+}:$CsPbX_3$ energy gap would be attractive for characterizing the specific energy-conservation threshold, and hence the quantum-cutting mechanism itself, and should also be useful for optimizing the performance of these materials for various applications. In principle, such tunability could be achieved by post-synthetic anion exchange; $CsPbCl_3$ NCs readily undergo anion exchange with several common halide reagents to form mixed-halide alloys,[28-32] but to date, all quantum-cutting Yb^{3+}:$CsPbCl_3$ and Yb^{3+}:$CsPb(Cl_{1-x}Br_x)_3$ NCs[17, 19, 22] and polycrystalline films[19] have been prepared by direct synthesis only. Anion exchange has not yet been reported in any quantum-cutting perovskites. It is unclear whether anion exchange will retain the charge-neutral defect clusters thought to be integral to the Yb^{3+}:$CsPb(Cl_{1-x}Br_x)_3$ quantum-cutting mechanism,[19] or whether such defects (or even the Yb^{3+} impurities themselves) may be passivated, dissociated, or extruded from the lattice during anion exchange, thereby sacrificing the high PLQYs.

Here we report a systematic investigation of the effects of $Cl^- \rightarrow Br^-$ anion exchange on the spectroscopic properties of Yb^{3+}:$CsPbX_3$ NCs. We find that it is possible to retain the high PLQYs of Yb^{3+}:$CsPbCl_3$ NCs (E_g ~ 3.06 eV, ~405 nm) during anion exchange while narrowing E_g to ~2.53 eV (~490 nm). For E_g below ~2.53 eV, the Yb^{3+} PLQY drops rapidly, demonstrating the anticipated energy threshold for quantum cutting. We further observe sensitivity of the Yb^{3+} PLQY to the presence of water in the anion-exchange reaction, either from air or deliberately introduced into an otherwise dry reaction. Whereas the NC absorption spectra show no apparent sensitivity to residual water under our reaction conditions, the Yb^{3+} PL is substantially diminished (by as much as 40%) when anion exchange is performed in the presence of water.

3.2 Physical Characterization of Yb^{3+}:$CsPb(Cl_{1-x}Br_x)_3$ NCs

Figure 3.1A shows TEM images of a representative sample of 7.7% Yb^{3+}:$CsPbCl_3$ NCs with average NC edge lengths of 14.1 ± 3.8 nm. The absorption and PL characteristics of $CsPbCl_3$ NCs are size-independent in this regime, and recent studies of Yb^{3+}:$CsPbCl_3$ polycrystalline thin films have demonstrated that quantum cutting is also largely unaffected by grain size.[19] **Figure 3.1B** shows TEM images of the same sample from **Figure 3.1A** after anion exchange to Yb^{3+}:$CsPbBr_3$ using trimethylsilyl bromide (TMS-Br) under dry, anaerobic conditions. The average NC size is now 14.8 ± 3.7 nm. A small degree of NC growth is to be expected due to the increase in lattice

parameter, and some NCs appear to have fused together during the anion-exchange reaction. **Figure 3.1C** presents XRD patterns for the Yb^{3+}:$CsPbCl_3$ and Yb^{3+}:$CsPbBr_3$ NCs along with reference peaks for the respective compositions. The experimental diffraction pattern obtained after anion exchange matches the anticipated orthorhombic $CsPbBr_3$ diffraction. No crystalline impurities are observed in either composition. Combined, these data illustrate successful conversion of $CsPbCl_3$ NCs into $CsPbBr_3$ NCs *via* anion exchange.

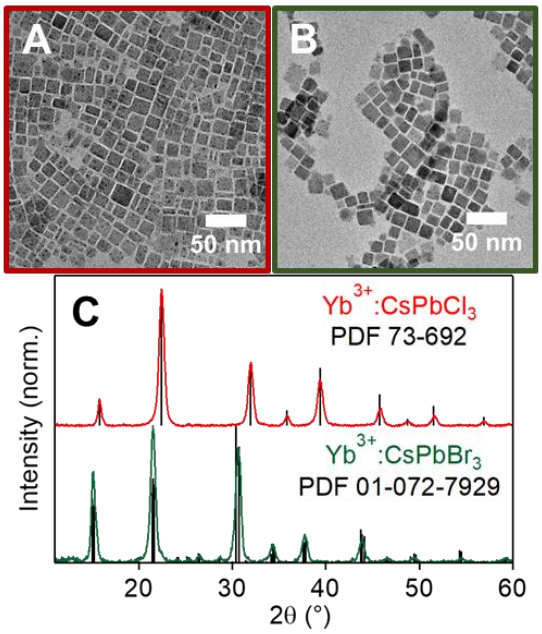

Figure 3.1 Physical Characterization of Yb^{3+}:$CsPbX_3$ (X = Cl, Br) NCs.

TEM images of 7.7% Yb^{3+}:$CsPbCl_3$ collected **(A)** before and **(B)** after anaerobic anion exchange with TMS-Br in dry hexane, which converts Yb^{3+}:$CsPbCl_3$ NCs into Yb^{3+}:$CsPbBr_3$ NCs. **(C)** Representative XRD data for the same NCs from panel A. Reference diffraction patterns are included for comparison, confirming essentially complete anion exchange.

3.3 *In situ* Optical Monitoring of Anion Exchange

Figure 3.2A plots absorption spectra collected *in situ* during a representative NC anion-exchange reaction. **Figure 3.2B** plots *in situ* PL spectra for the same reaction. For this data set, the NCs were excited at 375 nm using a constant per-NC excitation rate of 370 s^{-1}, with excitation powers adjusted during the course of the reaction according to the evolving optical density at 375 nm. The final absorption and PL spectra in this series exhibit the energy gap of $CsPbBr_3$, consistent with essentially complete anion exchange from Cl^- to Br^-. These data show that Yb^{3+} emission is still sensitized by NC photoexcitation even in the final Yb^{3+}:$CsPbBr_3$ NCs, but this PL is

substantially weaker in Yb^{3+}:$CsPbBr_3$ NCs than in Yb^{3+}:$CsPbCl_3$ or Yb^{3+}:$CsPb(Cl_{1-x}Br_x)_3$ NCs. **Figure 3.2C** summarizes these data by plotting the Yb^{3+} PL intensity *vs* the exciton PL wavelength from the data in **Figure 3.2B**. The PLQY of these specific Yb^{3+}:$CsPbCl_3$ NCs was ~114% before initiating the anion-exchange reaction. This plot shows that the Yb^{3+} PLQY remains above 100% until the first exciton shifts to below ~490 nm, at which point the Yb^{3+} PLQY drops rapidly with decreasing E_g. The narrowest energy gap where the full PLQY of the starting Yb^{3+}:$CsPbCl_3$ NCs corresponds to $x \approx 0.75$ in Yb^{3+}:$CsPb(Cl_{1-x}Br_x)_3$ NCs. Similar data have been obtained for many analogous samples, independent of PLQY (*vide infra*), consistent with this trend being intrinsic to the quantum-cutting mechanism itself. Overall, these data demonstrate the ability to finely tune E_g in quantum-cutting Yb^{3+}:$CsPb(Cl_{1-x}Br_x)_3$ NCs using anion exchange. Moreover, these results indicate that the quantum-cutting mechanism active in these materials remains effective despite the extensive lattice transformation that occurs during anion exchange.

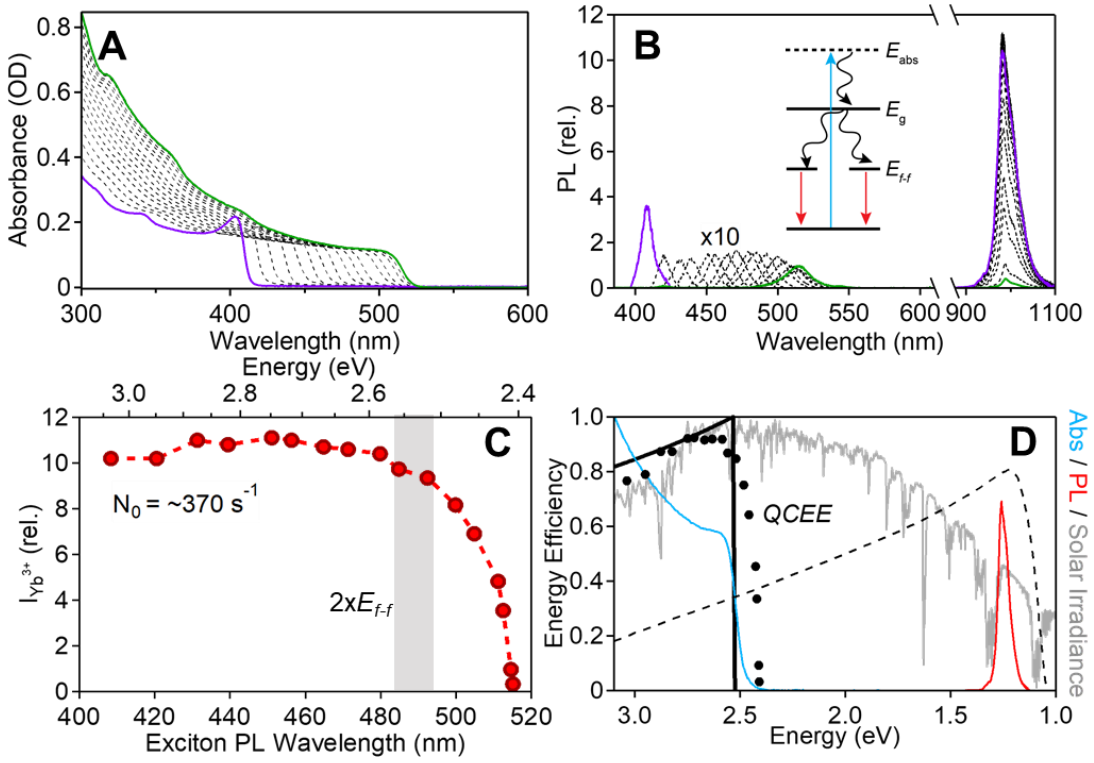

Figure 3.2 Optically-Monitored Chloride-to-Bromide Anion Exchange.

(A) Absorption spectra of 7.7% Yb^{3+}:$CsPb(Cl_{1-x}Br_x)_3$ NCs monitored *in situ* during anion exchange from Yb^{3+}:$CsPbCl_3$ (purple) to Yb^{3+}:$CsPbBr_3$ (green) using TMS-Br. **(B)** PL spectra collected *in situ* during the same reaction as in panel A. PL spectra were measured using 375 nm excitation at a constant NC excitation rate of

~370 s^{-1}. Absorption and PL spectra were recorded every ~14 min following addition of TMS-Br. **(C)** Plot of the Yb^{3+} $^2F_{5/2} \rightarrow {}^2F_{7/2}$ PL intensity *vs* the exciton PL wavelength, from the spectra in panel B. The gray shaded area marks approximately twice the Yb^{3+}($^2F_{7/2} \rightarrow {}^2F_{5/2}$) absorption onset ($2xE_{f\text{-}f}$) estimated from the PL spectra, *i.e.*, the anticipated energy threshold for quantum cutting in these materials below which energy conservation cannot be maintained. **(D)** The data from panel (C) replotted as quantum-cutting energy efficiency (QCEE, eq 2) *vs* E_{abs} (black circles) and eq 2 plotted for bandgap-optimized Yb^{3+}:$CsPb(Cl_{1-x}Br_x)_3$ NCs ($x \sim 0.75$, solid black curve) with an abrupt threshold. Both have been idealized to Φ_{max} = 200% for illustration. For comparison, the energy-conversion efficiency of a typical c-Si photovoltaic cell (dashed black), the AM1.5 solar spectral irradiance (grey), and the absorption (blue) and PL spectra (red) of the Yb^{3+}:$CsPb(Cl_{1-x}Br_x)_3$ NCs are also plotted. The inset in (B) illustrates the quantum-cutting process, including the thermalization loss when $E_{abs} > E_g \approx 2xE_{f\text{-}f}$ such as in bandgap-optimized Yb^{3+}:$CsPb(Cl_{1-x}Br_x)_3$ NCs.

The data in **Figure 3.2C** provide strong evidence of a discrete threshold energy for quantum cutting in these materials. The Yb^{3+} PL spectrum at low temperature shows its highest-energy feature at 1.267 eV (979 nm).[19] This feature is likely the first electronic origin within the crystal-field split $^2F_{5/2}$ multiplet, meaning it defines the low-temperature Yb^{3+}(*f-f*) absorption threshold as well. From the low-temperature origin, an energy threshold of $2xE_{f\text{-}f}$ = 2.534 eV (489 nm) is thus anticipated, indicated by the gray vertical bar in **Figure 3.2C**. At room temperature, vibronic hot bands broaden the *f-f* absorption spectrum slightly to lower energy, and this threshold is expected to shift correspondingly. From **Figure 3.2C**, the Yb^{3+} PL intensity indeed drops precisely when the excitonic PL energy crosses $2xE_{f\text{-}f}$.

The above results show that quantum cutting in Yb^{3+}:$CsPb(Cl_{1-x}Br_x)_3$ NCs has a very high intrinsic energy efficiency, *i.e.*, no step in the quantum cutting mechanism introduces any substantial thermalization losses. This high energy efficiency is consistent with our recent proposal that quantum cutting in these materials proceeds *via* a shallow trap state residing just a few tens of meV below the first exciton, because participation of a deeper trap state would result in PLQY losses that begin higher above $2xE_{f\text{-}f}$ than observed in **Figure 3.2C**. To highlight this energy efficiency, the data from **Figure 3.2C** are replotted in **Figure 3.2D** in terms of the quantum-cutting energy efficiency (QCEE) as defined by eq 3.1. These data are compared with the numerical results from eq 1 in the limit of zero thermalization, *i.e.*, for an idealized PLQY of Φ = 200% above threshold and 0% below threshold, and with a quantum-cutting threshold energy of $2xE_{f\text{-}f}$. Φ for the experimental data has also been idealized to 200% at its maximum value for the purposes of

comparison. For the idealized curve, the QCEE begins at ~82% for 3.06 eV band-edge absorption in Yb^{3+}:$CsPbCl_3$ NCs (and also for 3.06 eV absorption in bandgap-optimized Yb^{3+}:$CsPb(Cl_{1-x}Br_x)_3$ NCs) and it approaches 100% as E_{abs} approaches $2xE_{f\text{-}f}$, below which it drops rapidly to 0%. The experimental data follow this trend closely, except the drop-off is not as abrupt. **Figure 3.2D** also compares these QCEE plots with the energy-conversion efficiency curve of a high-performance c-Si photovoltaic cell. The latter has a value of only ~20% at 3.06 eV that increases to only ~35% at $2xE_{f\text{-}f}$. These low energy-conversion efficiencies reflect the narrow E_g of Si and hence the large thermalization losses in Si photovoltaics when converting blue photons. A QCEE of 100% in this region would allow thermalization losses normally associated with above-bandgap photoexcitation to be eliminated entirely and instead replaced by emission of an additional photon. As illustrated in **Figure 3.2D**, the Yb^{3+} emission from Yb^{3+}:$CsPb(Cl_{1-x}Br_x)_3$ NCs is very well aligned with the peak energy-conversion efficiency of c-Si photovoltaics. The high QCEEs of these Yb^{3+}:$CsPb(Cl_{1-x}Br_x)_3$ NCs thus motivates their use for eliminating thermalization losses in Si-based solar technologies.

$$QCEE = \frac{E_{PL}}{E_{abs}}\Phi \approx \frac{1.267\ eV}{E_{abs}}\Phi \tag{3.1}$$

In addition to high QCEEs, the *curvature* of the data in **Figure 3.2C** appears to be an intrinsic characteristic of this material system. Very similar curvature has been obtained in many analogous anion-exchange experiments for samples with many PLQYs, reaching as high as ~165% (see **Appendix 3.3**). Two potential sources of this curvature could be (*i*) loss of Yb^{3+} during anion exchange and (*ii*) PL power saturation.[19] The former possibility is ruled out by ICP-AES measurements showing that the Yb^{3+} content remains unchanged over the entire anion-exchange composition series, bolstered by the observation that converting product Yb^{3+}:$CsPbBr_3$ NCs back to Yb^{3+}:$CsPbCl_3$ NCs *via* anion exchange using oleylammonium chloride returns the Yb^{3+} PLQY to within ~20% of its original value, *i.e.*, well above 100% (see **Appendix 3.3**). The latter possibility is ruled out by performing the experiment at a constant excitation rate (**Figure 3.2**). When similar measurements are instead performed with a constant excitation source (fixed excitation wavelength and power density, *e.g.*, **Figure 3.3A**), then saturation also adds slightly to the decrease in PLQY with decreasing E_g (see **Appendix 3.2**), because anion exchange leads to increased NC excitation rates under these conditions. Instead of these two scenarios, it appears likely that the curvature seen in **Figure 3.2C** is intrinsic to the material and reflects changes in the energy matching between the energy donor (shallow trap) and energy acceptor ($2xE_{f\text{-}f}$) states

involved in quantum cutting. Such energy matching is required for energy conservation and hence contributes to the nonradiative energy-transfer rate, as summarized by Fermi's golden rule (eq 3.2, where R_{if} = energy transfer rate, M_{if} = electronic-coupling matrix element for the donor-acceptor interaction, ρ_f = density of acceptor states at the energy of the donor state, summed over donor energies). Our previous work has shown that trivalent-cation-doped $CsPbCl_3$ NCs have a broad trap-state PL with a peak maximum ~40 meV below the exciton PL,[19] indicating a multitude of viable donor energies and associated probabilities. This breadth, in conjunction with thermal broadening of the Yb^{3+}(*f-f*) absorption, causes the drop in R_{if} to be broadened in energy somewhat during the transition from the quantum-cutting ($E_g > 2xE_{f\text{-}f}$) regime to the non-quantum-cutting regime ($E_g < 2xE_{f\text{-}f}$) with anion exchange (**Figure 3.2C**).

$$R_{if} = \frac{2\pi}{\hbar}\left|M_{if}\right|^2 \rho_f \tag{3.2}$$

3.4 Anion Exchange Reaction Conditions

In the course of these anion-exchange measurements, we also noticed variations in the specific curves obtained under nominally similar reaction conditions, and we identified the presence of trace water as an important factor. For illustration, **Figure 3.3A** plots the Yb^{3+} PL intensity *vs* the exciton PL wavelength for reactions performed rigorously anaerobically (as in **Figure 3.2**) and aerobically. The Yb^{3+} PL of the aerobic anion-exchange reaction decreases already during the initial anion-exchange steps and remains ~20% lower than the reference anaerobic data set until the quantum-cutting threshold of ~489 nm is reached, beyond which the Yb^{3+} PL intensities in both data sets drop rapidly. Similarly, **Figure 3.3B** plots excitonic PL intensities *vs* exciton PL wavelength collected during the same reactions as shown in **Figure 3.3A**. Under anaerobic conditions, the excitonic PL intensity remains nearly constant throughout the entire anion-exchange reaction. When the reaction is performed aerobically, however, the exciton PL intensity increases by approximately an order of magnitude upon conversion from Yb^{3+}:$CsPbCl_3$ to Yb^{3+}:$CsPbBr_3$. For both reaction conditions, TMS-Br and benzoyl bromide anion-exchange reagents yield similar results. We note that both anion-exchange reagents react with water to form HBr, which may therefore be generated *in situ* under experimental conditions involving water and may be relevant to the observed influence of water.

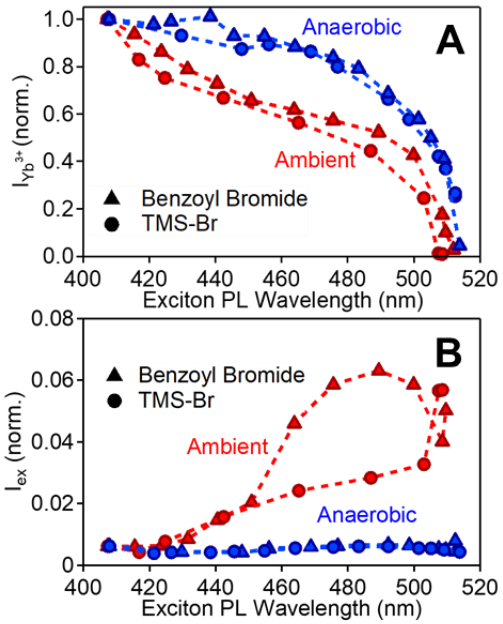

Figure 3.3 Monitoring Anion Exchange in Aerobic and Anaerobic Conditions

Relative **(A)** Yb^{3+} NIR (985 nm) and **(B)** excitonic PL intensities plotted *vs* excitonic PL wavelength, collected during $Cl^- \rightarrow Br^-$ anion exchange of 5.5% Yb^{3+}:$CsPbCl_3$ NCs using either TMS-Br or benzoyl bromide. PL intensities were collected using constant excitation power at 375 nm. Data were subsequently corrected for the changing absorbance at 375 nm, but not for changes in PL saturation. All intensities are normalized to the Yb^{3+} PL intensity of the starting Yb^{3+}:$CsPbCl_3$ NCs. Note the different *y*-axis scales.

A major difference between reactions performed with and without water present is their kinetics. **Figure 3.4** plots absorption spectra of Yb^{3+}:$CsPbCl_3$ NCs collected before and after anion exchange using TMS-Br for reactions performed under three different conditions: anaerobically in dry hexane, aerobically in aerated hexane, and anaerobically with water added to dry hexane (**Figures 3.4A, B, C**, respectively). Although all three data sets appear essentially identical, they arose from reactions with very different kinetics. **Figure 3.4D** plots the time evolution of the absorbance at 375 nm collected during each of these three anion-exchange reactions. Whereas the aerobic reaction was complete within 15 min, the anaerobic reaction took over 4 hr to reach completion. The entire kinetic trace for the anaerobic reaction is included in the inset of **Figure 3.4D**. **Figure 3.4E** summarizes the Yb^{3+} PL intensities measured during the same anion-exchange reactions. For the anaerobic reaction, the Yb^{3+} PL intensity remained constant until the energy gap reached ~489 nm, as in **Figure 3.2C**. Adding water to the reaction or aerating the solution both caused a decrease in Yb^{3+} PL intensity at earlier stages of the anion-exchange reaction. For

example, when the exciton PL was at 475 nm, the aerobic reaction showed Yb^{3+} PL intensities that were ~40% smaller than those of the anaerobic, dry reaction.

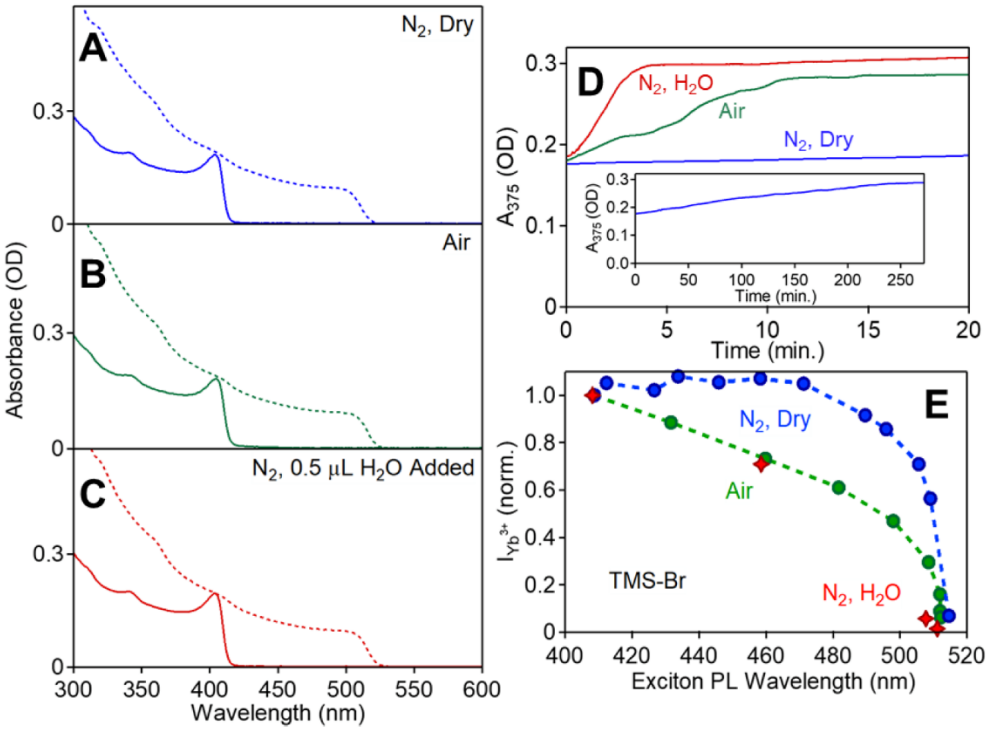

Figure 3.4 Probing the Effect of Water During Anion Exchange

Absorption spectra of 5.5% Yb^{3+}:$CsPbCl_3$ NCs collected before (solid lines) and after (dotted lines) anion exchange using TMS-Br under three different reaction conditions: **(A)** anaerobic in dry hexane, **(B)** aerobic in hexane, and **(C)** aerobic in dry hexane with added water (0.5 µL H_2O added to 3 mL dry hexane). **(D)** Kinetic traces monitoring the NC absorbance at 375 nm (A_{375}) following injection of TMS-Br under the three reaction conditions from panels A-C. Inset: Entire kinetic trace for the anaerobic anion-exchange reaction in dry hexane. **(E)** Intensity of Yb^{3+} PL at 985 nm plotted vs exciton PL wavelength for the same three anion exchange reactions, reacting 5.5% Yb^{3+}:$CsPbCl_3$ NCs with TMS-Br anaerobically in dry hexane (blue), aerobically (green), and anaerobically with 0.2 µL water added to 3 mL dry hexane (red).

One conceivable cause for the disparity between PL intensities obtained for anaerobic *vs* aerobic (hydrated) anion exchange could be a difference in the NCs themselves that results from the introduction of water, for example through extensive Ostwald ripening, oriented attachment, or NC dissolution. To test for such differences, the same reactions were probed by TEM, for both undoped and Yb^{3+}-doped NCs. **Figure 3.5** shows TEM images of undoped $CsPbCl_3$ and 4.1% Yb^{3+}-doped $CsPbCl_3$ NCs collected before and after anion exchange under the anaerobic and aerobic reaction conditions described in **Figure 3.4**. Whether the reaction is performed

anaerobically (slowly) or aerobically (rapidly), the NCs appear to grow slightly and maintain their cubic morphologies. Although some of the larger crystallites are observed after anion exchange that appear to arise from oriented attachment during reaction, formation of such morphologies is independent of Yb^{3+} doping. **Figures 3.5D,H** plot size-distribution histograms for these reactions with the undoped and doped NCs, respectively. The undoped NCs started with an edge length of 12.8 ± 3.3 nm, and this dimension grew to 13.7 ± 4.0 nm when anion exchange was performed aerobically, compared to 14.2 ± 5.7 nm when the reaction was performed anaerobically. The Yb^{3+}-doped NCs had a starting edge length of 11.8 ± 2.3 nm that grew to 14.7 ± 4.1 nm under aerobic reaction conditions, compared to 14.4 ± 4.3 nm under anaerobic conditions. These data show that the large increase in reaction rate and the substantial drop in Yb^{3+} PLQY observed when using aerobic reaction conditions are not accompanied by any detectable change in NC size or morphology. The effect of water on Yb^{3+} PL intensities during anion exchange thus appears to have a microscopic origin.

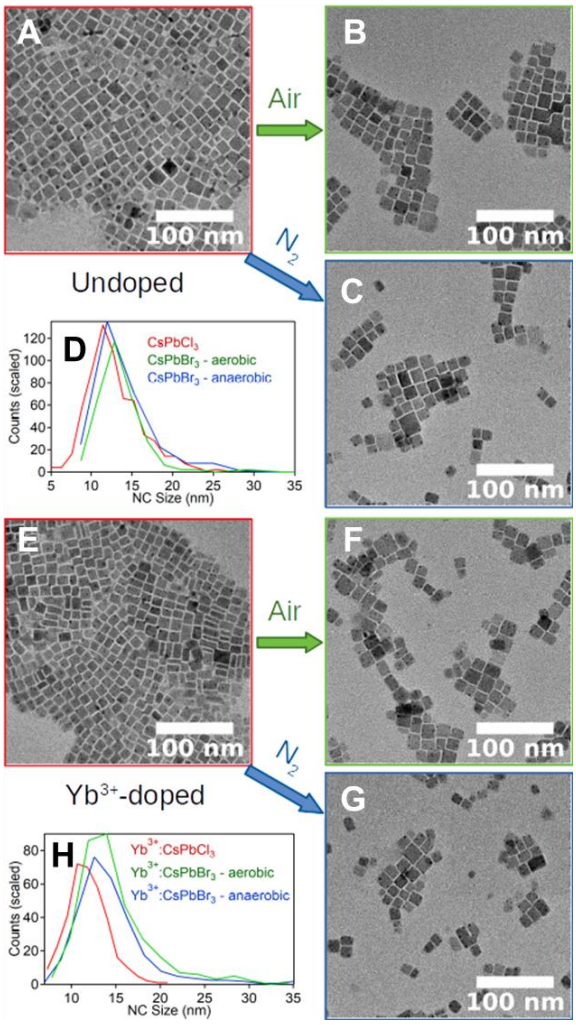

Figure 3.5 TEM of NCs Before and After Aerobic or Anaerobic Anion Exchange

TEM images and size distributions of **(A-D)** undoped $CsPbCl_3$ NCs and **(E-H)** 4.1% Yb^{3+}:$CsPbCl_3$ NCs collected before (A, E) and after (B, C, F, G) anion-exchange conversion to $CsPbBr_3$ and Yb^{3+}:$CsPbBr_3$ NCs using TMS-Br. Anion-exchange reactions were performed either aerobically (green, rapid reaction) after aerating dry hexane, or anaerobically (blue, slow reaction), as indicated in the figure and described by Figure 3.4.

We hypothesize that the presence of water may cause Yb^{3+} to be extruded from the NCs during the anion-exchange reaction, thereby eliminating the charge-neutral lattice defect clusters believed to be responsible for quantum cutting in these materials.[19] Such extraction could be driven by coordination of Yb^{3+} by water, given the high oxophilicity of Yb^{3+}. We have not observed any particularly strong sensitivity of Yb^{3+}:$CsPb(Cl_{1-x}Br_x)_3$ NCs to water under ambient storage conditions, which suggests that the lattice reorganization during anion exchange facilitates this

deactivation of Yb^{3+} PL. These results are particularly striking in light of the opposite trend observed in the excitonic PL intensities, which *increase* when the reaction is performed in the presence of water (**Figure 3.3B** and **Appendix 3.6**). Although the detailed microscopic mechanism of Yb^{3+} PL deactivation is still not entirely clear, these results highlight the need for dry solvents and atmosphere when tuning E_g in quantum-cutting Yb^{3+}:$CsPb(Cl_{1-x}Br_x)_3$ NCs *via* anion exchange.

3.5 Conclusions

In summary, we have demonstrated the use of anion-exchange chemistries to tune the energy gaps of Yb^{3+}:$CsPb(Cl_{1-x}Br_x)_3$ NCs continuously from $0 \leq x \leq \sim 1$. Quantum cutting is retained for x values as large as ~0.75, corresponding to ~2.53 eV (~489 nm). At larger x, a steep drop in PLQY is observed that is attributed to crossing an energy-conservation threshold. This threshold is a signature of the quantum-cutting mechanism. These results thus demonstrate that it is possible to tune E_g of quantum-cutting perovskite NCs over a reasonably large range to optimize these materials for solar- or other spectral-conversion technologies, without loss of PLQY. For example, for solar spectral downconversion applications involving Si, Yb^{3+}:$CsPbCl_3$ NCs absorb only ~3.3% of the solar photons above the Si absorption threshold of 1.1 eV (~2.1% of all AM1.5 solar photons), but Yb^{3+}:$CsPb(Cl_{0.25}Br_{0.75})_3$ NCs with the same PLQY can absorb ~13.2% of the solar photons absorbed by Si (~8.5% of all AM1.5 solar photons). Absorption of these blue photons and remission of that energy by Yb^{3+} with nearly perfect quantum-cutting energy efficiency may allow a sizable reduction in the thermalization losses of Si photovoltaics.

In addition to demonstrating retention of high PLQYs in quantum-cutting perovskite NCs during post-synthetic energy-gap tuning *via* anion exchange, the experiments here also demonstrate that anion exchange *does* diminish the PLQY substantially if the reaction is performed in the presence of water, even when E_g is still well above the quantum-cutting threshold. Water accelerates the anion-exchange reaction tremendously, independent of Yb^{3+}, but there is no detectable dependence of the NC morphology or average size on this reaction rate, suggesting that the loss of Yb^{3+} PLQY has a microscopic origin. In fact, the excitonic PLQY in undoped NCs actually increases when the anion-exchange reaction is performed in the presence of water, showing that water's influence is specific to Yb^{3+}. The reduction of Yb^{3+} PLQY during anion-exchange reactions performed in the presence of water is tentatively attributed to loss of Yb^{3+} from the internal NC volume, aided by its high oxophilicity. Overall, the results presented here provide new fundamental insight into the unique quantum-cutting process displayed by these NCs and also

offer valuable practical guidance for tuning the spectral characteristics of such NCs to optimize their performance in future solar and photonics applications.

3.6 Experimental

Materials. Octadecene (ODE) (90%, Acros Organic), oleylamine (OAm) (70%, Sigma Aldrich), oleic acid (OA) (90%, Sigma Aldrich), lead acetate trihydrate ($Pb(OAc)_2 \cdot 3H_2O$) (99.9%, Baker Chemical), ytterbium acetate hydrate [$Yb(OAc)_3 \cdot xH2O$] (99.9%, Alfa Aesar), cesium acetate (CsOAc) (99.9%, Alfa Aesar), anhydrous ethanol (200 proof, Decon Laboratories, Inc.), trimethylsilyl chloride (TMS-Cl) (98%, Acros Organics), hexanes (further dried over sodium benzophenone and distilled, 99%, Fisher Scientific), hydrochloric acid (Macron Fine Chemicals), coumarin153 (Exciton), and ethyl acetate (EtOAc) (99%, Sigma Aldrich) were used as received unless otherwise noted.

Synthesis of Yb^{3+}:$CsPbCl_3$ nanocrystals. Quantum-cutting Yb^{3+}:$CsPbCl_3$ NCs were synthesized following the procedure detailed in Milstein *et al.*[19] Briefly, 0.2 mmol $Pb(OAc)_2 \cdot 3H_2O$, 0.08 mmol $Yb(OAc) \cdot xH_2O$, and 0.28 mL 1 M CsOAc dissolved in ethanol were added to a 50 mL round bottom flask with 5 mL ODE, 1 mL OA, and 0.5 mL OAm. Using Schlenk line technique, the reaction vessel was then evacuated and degassed at 110 °C for 1 h. Afterwards, the vessel was flushed with N_2 and heated to 240 °C whereupon 0.2 mL TMS-Cl in 0.5 mL ODE were swiftly injected and the whole flask quenched via a room temperature water bath. After the mixture reached room temperature, it was centrifuged for 15 min and the supernatant was discarded; the pellet was resuspended in hexanes. The NCs were flocculated out of solution with EtOAc. The solution was then centrifuged for 10 min and the supernatant was discarded. The solution was resuspended in hexanes and centrifuged for 10 min. The supernatant was filtered through a 0.2 μm PTFE filter to obtain the final NC solution. For storage, the NC solution was dried down and resuspended in anhydrous solvent in an N_2-filled glovebox. All nanocrystal solutions were stored with a concentration ~6 mg/mL. For reference, undoped $CsPbCl_3$ NCs were synthesized following the same protocol except without $Yb(OAc) \cdot xH_2O$ and using only 0.24 mL of 1M CsOAc in EtOH.

Physical characterization. Absorption measurements were performed using an Agilent Cary 60 spectrometer. Photoluminescence (PL) data were measured using a 375 nm LED for excitation and a liquid-N_2-cooled silicon CCD mounted on a 0.3 m monochromator for detection. All PL spectra were corrected for the instrument's spectral response and, unless specified otherwise, for

the optical density of the NCs at the excitation wavelength. PL spectra with constant excitation rate were acquired by attenuating the excitation source using a variable-neutral-density filter and monitoring the excitation power with a power meter. Nanocrystal TEM images were obtained using an FEI TECNAI G2 F20 microscope operated at 200 kV. Samples for TEM were prepared by drop casting NCs onto UC-A 400 mesh Cu grids from TED Pella, Inc. The sample grids were then dried under vacuum overnight. Three hundred individual NCs per sample were sized to obtain the mean NC sizes reported here. Elemental compositions were determined by inductively coupled plasma – atomic emission spectroscopy (ICP-AES, PerkinElmer 8300). ICP-AES samples were prepared by digesting NCs in concentrated nitric acid overnight with sonication. Powder X-ray diffraction data were collected using a Bruker D8 Advance. Samples were prepared by drop casting NC suspensions onto silicon substrates. Quantum yields were measured following the methodology detailed in Milstein *et al*.[19] Briefly, dilute NCs solutions ($OD_{Exciton} < 0.2$) in sealed 1 cm path length quartz Spectrocell cuvettes were placed in a teflon integrating sphere fiber optically coupled to an LN_2-cooled CCD. The samples were excited using a 375 nm LED. All spectra were corrected for the wavelength-dependent detector response and attenuation by the optics, integrating sphere, fiber optic cable, and monochromator grating.

Anion exchange using TMS-Br. Anion-exchange reactions were carried out in a 1 cm path length FUV quartz Spectrocell cuvette. 30 μL of stock NC solution stored in the glovebox (typically stored at 6 mg/mL) was diluted in 2.95 mL of anhydrous hexane (OD at first exciton ~0.2). Absorption and PL spectra were measured before adding 20 μL 0.1 M TMS-Br to the solution in the glovebox. Absorption and PL spectra were monitored continuously until the reaction reached completion (next day for full equilibration). For the reactions performed in ambient conditions, NCs kept outside of the box were diluted in sintered glass vials to a concentration approximately equal to that used for reactions performed in the glovebox. Anion exchange was then performed by titration of the NCs with 0.01 M TMS-Br. After each addition of TMS-Br, the absorption and PL spectra were measured. Anion exchange reaction variants involving the addition of water to anaerobic, dry hexane were carried out by adding ultrapure H_2O to the solvent under an Ar gas flow followed by vigorous shaking. Reactions involving the addition of ambient air to anaerobic hexane was carried out by pipetting ambient air through the reaction mixture. The water or air were added before the addition of the bromide reagent.

Anion exchange using benzoyl bromide. Anion-exchange reactions were carried out

similarly to those reported above except 0.1 M and 0.01 M benzoyl bromide solutions were used for the reactions performed in and out of the glovebox, respectively.

Anion exchange using oleylammonium chloride. Oleylammonium chloride (OAm-HCl) was synthesized by reacting oleylamine with HCl following previous reports of their use in $CsPbCl_3$ NC preparation.[28] A 56 mM OAm-HCl solution in a 1:1 (v/v) solution of toluene and hexane was titrated with Yb^{3+}:$CsPbBr_3$ (prepared by anion exchanging Yb^{3+}:$CsPbCl_3$ NCs with TMS-Br in anaerobic, dry conditions) via dropwise addition and monitored using absorption and PL spectroscopies (detailed above).

Kinetics measurements. Anion-exchange reactions were initiated in a glovebox and the absorption monitored at 375 nm using the kinetics mode of an Agilent Cary 60. For some experiments, 0.5 μL of nanopore water was added to 3 ml of the NC solution under argon gas flow. For aerobic experiments, a glass pipette was used to bubble ambient air through the solution for about 5 s before anion exchange.

3.7 Acknowledgments.

The following people contributed to this chapter: Kyle T. Kluherz performed TEM imaging and analysis; Daniel M. Kroupa provided helpful discussion and performed exploratory anion exchange experiments; Christian S. Erickson helped perform the excitation-rate dependent PL measurements; James J. De Yoreo provided thoughtful analysis and supervised the project; Daniel R. Gamelin provided helpful discussion and supervised all the work.

This research was supported by the National Science Foundation (NSF) through the UW Molecular Engineering Materials Center, a Materials Research Science and Engineering Center (DMR-1719797). Additional support from DMR-1807394 (to DRG) and the Washington Research Foundation (to DMK) is gratefully acknowledged. Part of this work was conducted at the UW Molecular Analysis Facility, a National Nanotechnology Coordinated Infrastructure site supported in part by the NSF (ECC-1542101), the University of Washington, the Molecular Engineering and Sciences Institute, the Clean Energy Institute, and the National Institutes of Health. Dr. Matthew Crane is acknowledged for assistance with the solar-flux calculations.

References

1. Protesescu, L.; Yakunin, S.; Bodnarchuk, M. I.; Krieg, F.; Caputo, R.; Hendon, C. H.; Yang, R. X.; Walsh, A.; Kovalenko, M. V. *Nano Lett.* **2015,** *15*, 3692-3696.

2. ten Brinck, S.; Infante, I. *ACS Energy Lett.* **2016,** *1*, 1266-1272.
3. Akkerman, Q. A.; Rainò, G.; Kovalenko, M. V.; Manna, L. *Nat. Mater.* **2018,** *17*, 394-405.
4. Yakunin, S.; Protesescu, L.; Krieg, F.; Bodnarchuk, M. I.; Nedelcu, G.; Humer, M.; De Luca, G.; Fiebig, M.; Heiss, W.; Kovalenko, M. V. *Nat. Commun.* **2015,** *6*, 8056.
5. Ramasamy, P.; Lim, D.-H.; Kim, B.; Lee, S.-H.; Lee, M.-S.; Lee, J.-S. *Chem. Commun.* **2016,** *52*, 2067-2070.
6. Swarnkar, A.; Marshall, A. R.; Sanehira, E. M.; Chernomordik, B. D.; Moore, D. T.; Christians, J. A.; Chakrabarti, T.; Luther, J. M. *Science* **2016,** *354*, 92.
7. Sanehira, E. M.; Marshall, A. R.; Christians, J. A.; Harvey, S. P.; Ciesielski, P. N.; Wheeler, L. M.; Schulz, P.; Lin, L. Y.; Beard, M. C.; Luther, J. M. *Sci. Adv.* **2017,** *3*.
8. Swarnkar, A.; Ravi, V. K.; Nag, A. *ACS Energy Lett.* **2017,** *2*, 1089-1098.
9. van der Stam, W.; Geuchies, J. J.; Altantzis, T.; van den Bos, K. H. W.; Meeldijk, J. D.; Van Aert, S.; Bals, S.; Vanmaekelbergh, D.; de Mello Donega, C. *J. Am. Chem. Soc.* **2017,** *139*, 4087-4097.
10. Yao, J.-S.; Ge, J.; Han, B.-N.; Wang, K.-H.; Yao, H.-B.; Yu, H.-L.; Li, J.-H.; Zhu, B.-S.; Song, J.-Z.; Chen, C.; Zhang, Q.; Zeng, H.-B.; Luo, Y.; Yu, S.-H. *J. Am. Chem. Soc.* **2018,** *140*, 3626-3634.
11. Parobek, D.; Roman, B. J.; Dong, Y.; Jin, H.; Lee, E.; Sheldon, M.; Son, D. H. *Nano Lett.* **2016,** *16*, 7376-7380.
12. Liu, W.; Lin, Q.; Li, H.; Wu, K.; Robel, I.; Pietryga, J. M.; Klimov, V. I. *J. Am. Chem. Soc.* **2016,** *138*, 14954-14961.
13. Lin, C. C.; Xu, K. Y.; Wang, D.; Meijerink, A. *Sci. Rep.* **2017,** *7*, 45906.
14. Yuan, X.; Ji, S.; De Siena, M. C.; Fei, L.; Zhao, Z.; Wang, Y.; Li, H.; Zhao, J.; Gamelin, D. R. *Chem. Mater.* **2017,** *29*, 8003-8011.
15. Xu, K.; Lin, C. C.; Xie, X.; Meijerink, A. *Chem. Mater.* **2017,** *29*, 4265-4272.
16. Mir, W. J.; Mahor, Y.; Lohar, A.; Jagadeeswararao, M.; Das, S.; Mahamuni, S.; Nag, A. *Chem. Mater.* **2018,** *30*, 8170-8178.
17. Zhou, D.; Liu, D.; Pan, G.; Chen, X.; Li, D.; Xu, W.; Bai, X.; Song, H. *Adv. Mater.* **2017**, 1704149.
18. Pan, G.; Bai, X.; Yang, D.; Chen, X.; Jing, P.; Qu, S.; Zhang, L.; Zhou, D.; Zhu, J.; Xu, W.; Dong, B.; Song, H. *Nano Lett.* **2017,** *17*, 8005-8011.
19. Milstein, T. J.; Kroupa, D. M.; Gamelin, D. R. *Nano Lett.* **2018,** *18*, 3792-3799.
20. van der Ende, B. M.; Aarts, L.; Meijerink, A. *Adv. Mat.* **2009,** *21*, 3073-3077.
21. van der Ende, B. M.; Aarts, L.; Meijerink, A. *Phys. Chem. Chem. Phys.* **2009,** *11*, 11081-11095.
22. Luo, X.; Ding, T.; Liu, X.; Liu, Y.; Wu, K. *Nano Lett.* **2018,** *19*, 338-341.
23. Meijer, J.-M.; Aarts, L.; van der Ende, B. M.; Vlugt, T. J. H.; Meijerink, A. *Phys. Rev. B* **2010,** *81*, 035107.
24. Creutz, S. E.; Fainblat, R.; Kim, Y.; De Siena, M. C.; Gamelin, D. R. *J. Am. Chem. Soc.* **2017,** *139*, 11814-11824.
25. Shao, W.; Lim, C.-K.; Li, Q.; Swihart, M. T.; Prasad, P. N. *Nano Lett.* **2018,** *18*, 4922-4926.
26. Wang, Z.; Meijerink, A. *J. Phys. Chem. Lett.* **2018,** *9*, 1522-1526.
27. Rufino Souza, A. K.; Langaro, A. P.; Silva, J. R.; Costa, F. B.; Yukimitu, K.; Silos Moraes, J. C.; Antonio de Oliveira Nunes, L.; Humberto da Cunha Andrade, L.; Lima, S. M. *J. Alloys Comp.* **2018,** *781*, 1119-1126.

28. Nedelcu, G.; Protesescu, L.; Yakunin, S.; Bodnarchuk, M. I.; Grotevent, M. J.; Kovalenko, M. V. *Nano Lett.* **2015,** *15*, 5635-5640.
29. Akkerman, Q. A.; D'Innocenzo, V.; Accornero, S.; Scarpellini, A.; Petrozza, A.; Prato, M.; Manna, L. *J. Am. Chem. Soc.* **2015,** *137*, 10276-10281.
30. Parobek, D.; Dong, Y.; Qiao, T.; Rossi, D.; Son, D. H. *J. Am. Chem. Soc.* **2017,** *139*, 4358-4361.
31. Imran, M.; Caligiuri, V.; Wang, M.; Goldoni, L.; Prato, M.; Krahne, R.; De Trizio, L.; Manna, L. *J. Am. Chem. Soc.* **2018,** *140*, 2656-2664.
32. Creutz, S. E.; Crites, E. N.; De Siena, M. C.; Gamelin, D. R. *Chem. Mater.* **2018,** *30*, 4887–4891.
33. Kroupa, D. M.; Roh, J. Y.; Milstein, T. J.; Creutz, S. E.; Gamelin, D. R. *ACS Energy Lett.* **2018,** *3*, 2390-2395.
34. De Roo, J.; Ibáñez, M.; Geiregat, P.; Nedelcu, G.; Walravens, W.; Maes, J.; Martins, J. C.; Van Driessche, I.; Kovalenko, M. V.; Hens, Z. *ACS Nano* **2016,** *10*, 2071-2081.

3.8 Appendices

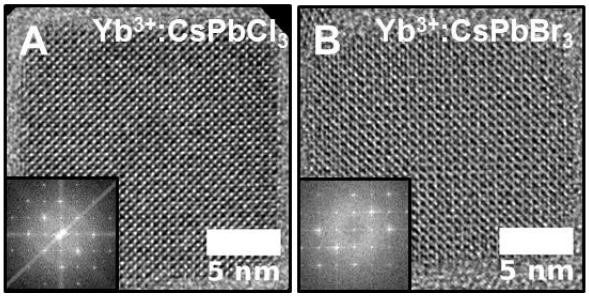

Appendix 3.1. **High-resolution TEM images.** TEM images of 7.7% Yb^{3+}:$CsPbCl_3$ **(A)** before and **(B)** after anaerobic anion exchange with TMS-Br in dry hexane. Insets: FFTs of the respective NCs imaged.

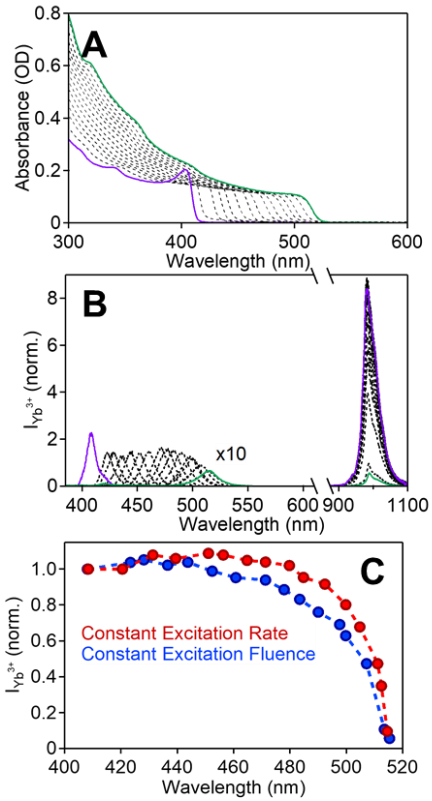

Appendix 3.2. **In-situ PL monitoring of chloride-to-bromide anion exchange using constant excitation rate.** (**A**) Absorption spectra of 7.7% Yb^{3+}:$CsPbCl_3$ NCs monitored *in situ* during anion exchange using TMS-Br. (**B**) PL spectra collected *in situ* during the same reaction as in panel A. PL spectra were measured using 375 nm excitation at a constant NC excitation power (40 mW through a 1mm pinhole). (**C**) Scatterplot of the Yb^{3+} $^2F_{5/2} \rightarrow {}^2F_{7/2}$ PL intensity vs the exciton PL wavelength from the spectra in B (blue) with the data from Figure 2C (red) in which the sample was excited with constant excitation rate.

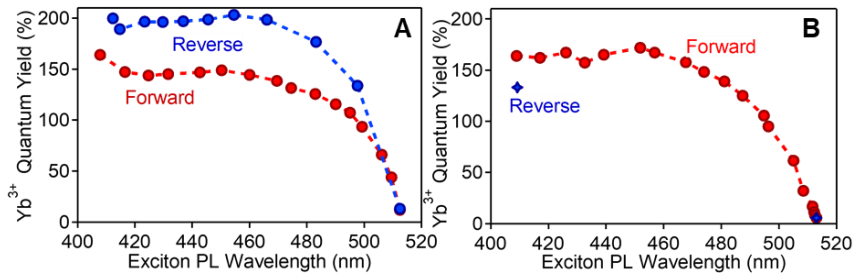

Appendix 3.3. **Chloride-to-bromide-to-chloride anion exchange.** Scatterplots detailing the forward anion exchange of 7.5% Yb^{3+}:$CsPbCl_3$ NCs using TMS-Br in anaerobic, dry hexane (red) and the reverse anion exchange back to the chloride via titration of OAm-HCl dissolved in an (**A**) anaerobic, dry or (**B**) ambient toluene:hexane (1:1, v:v) solution (blue). The NCs were excited at 375 nm and the PL spectra were corrected for their evolving absorption at 375 nm.[34]

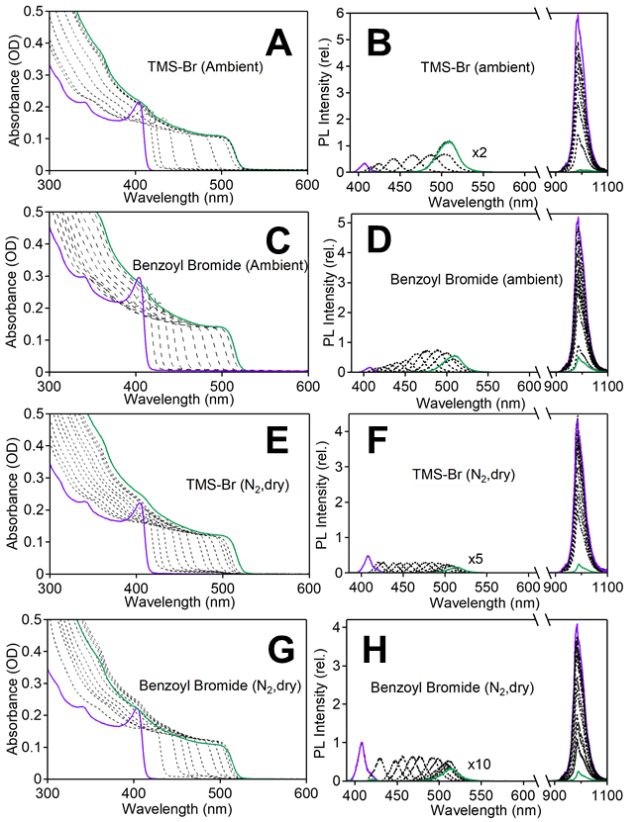

Appendix 3.4. **In-situ optical monitoring of chloride-to-bromide anion exchanges in ambient and anaerobic, dry solvents.** (**A**,**C**,**E**,**G**) Absorption and (**B**,**D**,**F**,**H**) PL spectra of the data corresponding to Figure 2. 5.5% Yb^{3+}:$CsPbCl_3$ NCs were reacted with TMS-Br and benzoyl bromide in ambient or anaerobic and dry hexane (purple to green). All PL spectra were measured using 375 nm excitation operating at constant power and corrected for the evolving optical density at 375 nm.

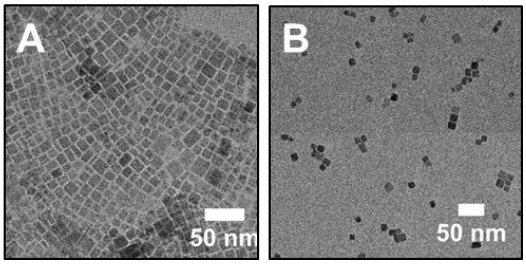

Appendix 3.5. TEM images before and after anion exchange. TEM images of undoped $CsPbCl_3$ NCs (**A**) before and (**B**) after anion exchange using TMS-Br in anaerobic and dry conditions.

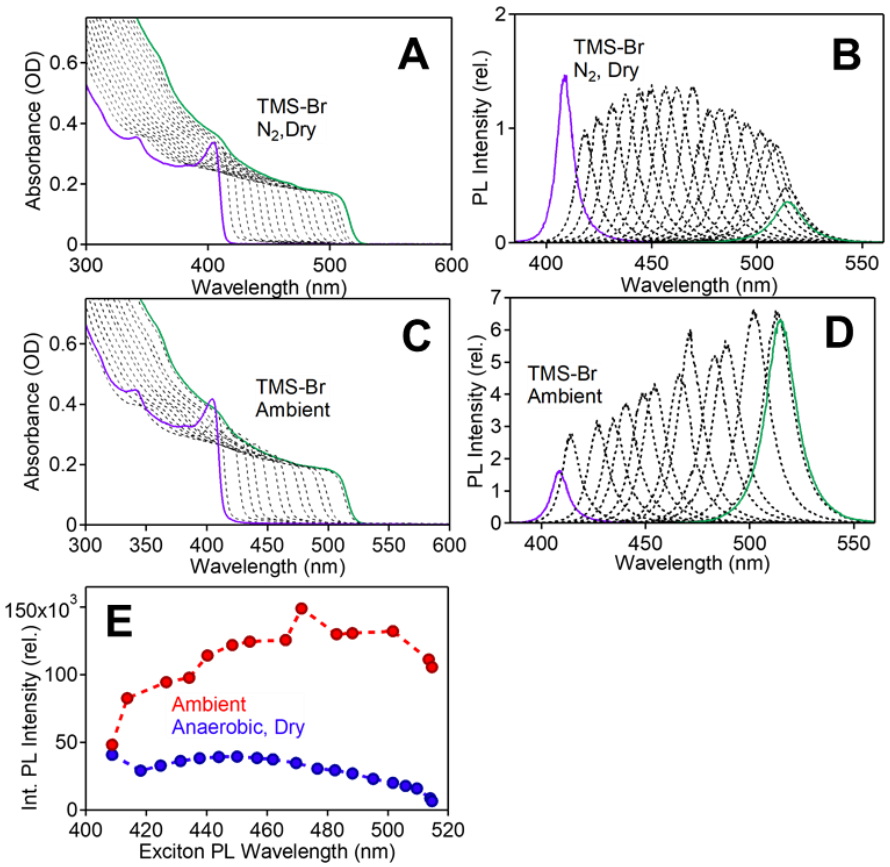

Appendix 3.6. Comparison of chloride-to-bromide anion exchange in ambient and anaerobic, dry conditions. (**A**,**C**) Absorption and (**B,D**) corresponding PL spectra of the anion exchange of $CsPbCl_3$ NCs using TMS-Br in aerobic (C,D) or anaerobic and dry reaction conditions (A,B) (purple to green). (**E**) Integrated exciton emission against the exciton PL wavelength for the reactions corresponding to A-D.

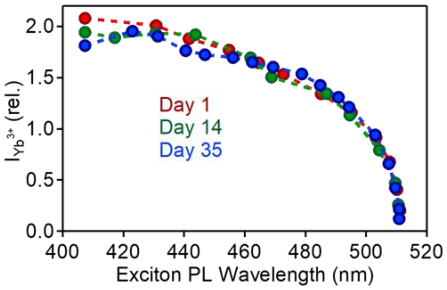

Appendix 3.7. **Replicability of chloride-to-bromide anion exchange several weeks after synthesis.** Yb^{3+} $^2F_{5/2} \rightarrow {}^2F_{7/2}$ PL intensity vs the exciton PL wavelength for the anion exchange of 6.6% Yb^{3+}:$CsPbCl_3$ using TMS-Br anaerobically in dry hexane repeated 2 and 5 weeks after synthesis. Emission intensity is relative to the Yb^{3+}:Coumarin153 integrated PL ratio.

Chapter 4 The Near-Band-Edge Defect State in Rare-Earth-Doped Lead-Halide Perovskites

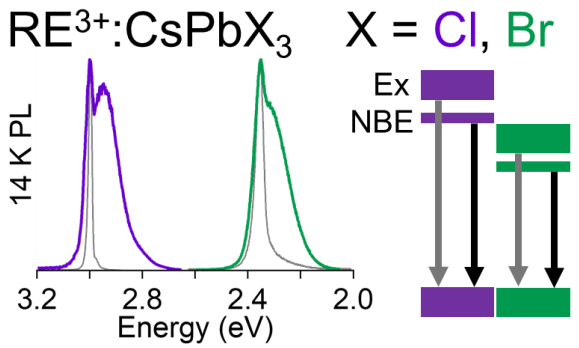

Abstract. $CsPb(Cl_{1-x}Br_x)_3$ ($0 \le x \le 1$) nanocrystals and thin films doped with a series of trivalent rare-earth ions (RE^{3+} = Y^{3+}, La^{3+}, Ce^{3+}, Gd^{3+}, Er^{3+}, Lu^{3+}) have been prepared and studied using variable-temperature and time-resolved photoluminescence spectroscopies. We demonstrate that aliovalent (trivalent) doping of this type universally generates a new and often-emissive defect state ca. 50 meV inside the perovskite band gap, independent of the specific RE^{3+} dopant identity or of the perovskite form (nanocrystals *vs* thin films). Chloride-to-bromide anion exchange is used to demonstrate that this near-band-edge photoluminescence shifts with changing band-gap energy to remain just below the excitonic luminescence for all compositions of $CsPb(Cl_{1-x}Br_x)_3$ ($0 \le x \le 1$). Computations show that this shift stems from the effect of the changing lattice dielectric constants on a shallow defect-bound exciton. Microscopic descriptions of this dopant-induced near-band-edge state and its relation to quantum cutting in Yb^{3+}-doped $CsPb(Cl_{1-x}Br_x)_3$ are discussed.

4.1 Introduction

Trivalent rare-earth (RE^{3+}) doping of all-inorganic lead-halide perovskites ($CsPbX_3$, X = halide) has recently attracted broad interest. In $CsPbI_3$, Eu^{3+} and Yb^{3+} dopants have been found to enhance stability of the desired α-phase and to yield superior photovoltaic efficiencies compared to their undoped counterparts.[1-2] Another study reported enhancement of power conversion efficiencies (PCEs) from 7% in solar cells based on undoped $CsPbBr_3$ to ~10% in cells using RE^{3+}-doped $CsPbBr_3$ (RE^{3+}:$CsPbBr_3$, where RE^{3+} = Sm^{3+}, Tb^{3+}, Ho^{3+}, Er^{3+}, Yb^{3+}).[3] RE^{3+} doping has also been reported to enhance excitonic photoluminescence quantum yields (PLQYs), even for RE^{3+} ions that are spectroscopically innocent (*i.e.*, lacking electronic transitions of their own within the perovskite energy gap), such as Y^{3+},[4] La^{3+},[4] Ce^{3+},[5-6] Gd^{3+},[7] and Lu^{3+}.[4] Other RE^{3+} dopants that do have internal electronic excited states at mid-gap energies have been used to generate new near-infrared (NIR) and/or visible emission from lead-halide perovskites through PL sensitization.[8-9]

Particularly notable is the observation of PLQYs exceeding 100% in Yb^{3+}:$CsPb(Cl_{1-x}Br_x)_3$ perovskites.[8-27] This phenomenon occurs *via* "quantum cutting", in which absorption of a high-energy photon generates emission of two Yb^{3+} $^2F_{5/2} \rightarrow {}^2F_{7/2}$ photons in the NIR, each at *ca.* half the absorbed photon's energy. It has been hypothesized[12] that quantum cutting in Yb^{3+}:$CsPb(Cl_{1-x}Br_x)_3$ is facilitated by a defect state associated with charge compensation of the aliovalent Yb^{3+} dopants. Transient-absorption measurements have demonstrated perovskite exciton-bleach recovery on the timescale as short as a few picoseconds upon Yb^{3+} doping,[12] but Yb^{3+} PL shows a rise time of ~8 ns,[22] supporting participation of an intermediate state in this quantum-cutting mechanism. The strong PLQY dependence on the $CsPbX_3$ energy gap in the region of $E_g \sim 2xE_{f\text{-}f}$ further suggests that this intermediate state must be close in energy to the exciton.[18] An interesting related hypothesis is that the quantum-cutting intermediate state involves capture of a photogenerated conduction-band electron by an individual Yb^{3+} ion to form Yb^{2+}, which subsequently relaxes to excite two Yb^{3+} ions to their $^2F_{5/2}$ excited states.[23, 27] One approach to refine the above hypotheses experimentally is to examine the photophysical effects of spectroscopically innocent RE^{3+} dopants in $CsPbX_3$ perovskites. Despite numerous studies of RE^{3+}:$CsPbX_3$ aimed at applications, the more general effects of aliovalent RE^{3+} doping in lead-halide perovskites are not yet well characterized. Such fundamental studies will improve the understanding of aliovalent doping in these materials, and of the ensuing photophysical consequences.

To this end, we report here an investigation of the low- and variable-temperature PL of a series

of RE^{3+}:$CsPb(Cl_{1-x}Br_x)_3$ nanocrystals (NCs) and thin films to understand the effects of RE^{3+} dopants on the perovskite electronic structure and photophysics. To ensure we are only probing structural and electrostatic effects, we focus primarily on RE^{3+} dopants that have no interfering *f-f, d-d, f-d,* or charge-transfer transitions within the perovskite energy gap (Y^{3+}, La^{3+}, Ce^{3+}, Gd^{3+}, and Lu^{3+}). These experiments reveal that *all* of these spectroscopically innocent RE^{3+} dopants give rise to similar near-band-edge (NBE) PL at low temperatures, characterized by a binding energy of ~50 meV. Intense NBE PL is observed for $0 \leq x \leq 1$, with a binding energy that decreases slightly on converting from RE^{3+}:$CsPbCl_3$ to RE^{3+}:$CsPbBr_3$, attributable to the increasing dielectric constants of the perovskite lattice across this series. The NBE PL also shows a strong temperature dependence that suppresses most intensity above ~100 K, but it is still clearly manifested in time-resolved PL measurements at room temperature, indicating that this state remains influential. The study is further extended to Er^{3+}:$CsPb(Cl_{1-x}Br_x)_3$, which also displays the same NBE PL at low temperature despite having internal *f-f* excited states within the perovskite energy gap. The RE^{3+} dopants examined here thus span the full range of lanthanide atomic numbers and include the non-lanthanide, Y^{3+}. Consequently, we conclude that *all* trivalent substitutional dopants will generate the same NBE defect state in $CsPbX_3$ perovskites. These results have interesting ramifications for interpretation of doping effects on both the photophysical and electronic properties of lead-halide perovskites and they inform the development of doped perovskites for future optoelectronic technologies.

4.2 Nanocrystals.

Figures 4.1A,B show room-temperature absorption and PL data for $CsPbCl_3$ and 7.7% Gd^{3+}:$CsPbCl_3$ NCs, respectively. Doping concentrations are determined analytically using ICP-OES and reported with respect to all B-site cations. Despite the large Gd^{3+} content in the doped NCs, their absorption spectrum closely resembles that of undoped $CsPbCl_3$ NCs. The room-temperature PL spectrum of the Gd^{3+}-doped NCs also closely matches that of the undoped $CsPbCl_3$ NCs. The Stokes shift between the excitonic absorption and PL maxima is small (~22 meV peak-to-peak) for both samples. Figure 4.1C plots X-ray diffraction data collected for the NCs from Figures 4.1A,B. The observation of very similar diffraction angles despite high Gd^{3+} incorporation is attributed to the offsetting structural effects of charge-compensating Pb^{2+} vacancies.[28] Figures 4.1D,E show representative TEM images of the NCs from Figures 4.1A,B, respectively. The

$CsPbCl_3$ and 7.7% Gd^{3+}:$CsPbCl_3$ NCs have an average edge-to-edge length of 10.9 ± 2.1 and 11.5 ± 4.0 nm, respectively. These NCs are larger than the $CsPbCl_3$ Bohr exciton diameter of ~5 nm,[29] and consequently no quantum confinement is expected. Overall, Gd^{3+}-doped and undoped $CsPbCl_3$ NCs are thus essentially indistinguishable in these measurements.

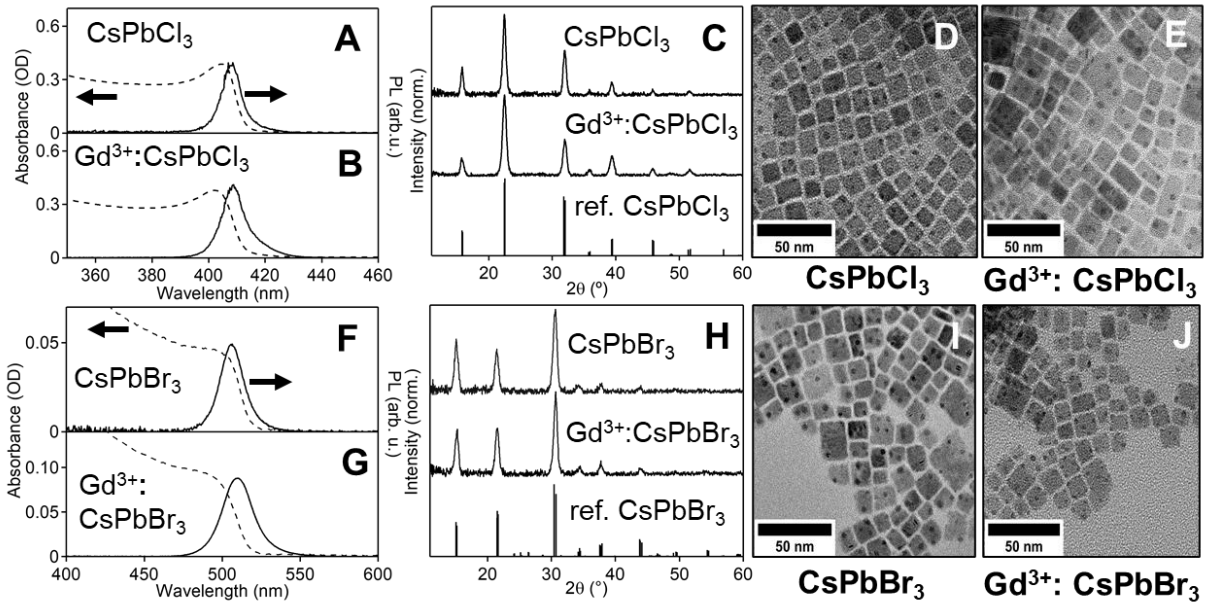

Figure 4.1 Physical Characterization of $CsPbX_3$ and Gd^{3+}:$CsPbX_3$ NCs.

(A, B) Room-temperature absorption and PL spectra of $CsPbCl_3$ (panel A) and 7.7% Gd^{3+}:$CsPbCl_3$ (panel B) NCs. **(C)** X-ray diffraction patterns of the NCs from panels A, B. Reference orthorhombic $CsPbCl_3$.[30] **(D, E)** TEM images of the NCs from panels A, B. Scale bar: 50 nm. **(F, G)** Room-temperature absorption and PL spectra of $CsPbBr_3$ (panel F) and 7.7% Gd^{3+}:$CsPbBr_3$ (panel G) NCs. **(H)** X-ray diffraction patterns of the NCs from panels F, G. Reference orthorhombic $CsPbBr_3$.[30] **(I, J)** TEM images of the NCs from panels F, G. Scale bar: 50 nm.

The same similarity is found between doped and undoped $CsPbBr_3$ NCs. Figures 4.1F,G show room-temperature absorption and PL spectra of $CsPbBr_3$ and 7.7% Gd^{3+}:$CsPbBr_3$ NCs made from the parent chloride NCs by anion exchange. The room-temperature absorption and PL spectra of the Gd^{3+}-doped NCs again closely resemble those of the undoped $CsPbBr_3$ NCs. Likewise, Figure 4.1H shows X-ray diffraction data collected for the NCs from Figures 4.1F,G, and these also look indistinguishable. Figures 4.1I,J show representative TEM images of the NCs from Figures 4.1F,G. The $CsPbBr_3$ and 7.7% Gd^{3+}:$CsPbBr_3$ NCs have average edge-to-edge lengths of 11.6 ± 2.4 and 12.9 ± 3.8 nm, respectively. These sizes relative to those in panels D and E are consistent

with expectations from replacement of chloride anions with larger bromide anions during anion exchange. The $CsPbBr_3$ NCs are larger than the $CsPbBr_3$ Bohr exciton diameter of ~7 nm,[29] and hence, quantum confinement effects are again not expected.

Although the PL spectra of Gd^{3+}-doped and undoped $CsPb(Cl_{1-x}Br_x)_3$ NCs look essentially identical at room temperature, major differences emerge at low temperatures. Figure 4.2A plots 14 K PL spectra of a series of Gd^{3+}:$CsPbCl_3$ NCs with doping concentrations ranging from 0.0 to 9.3%. A small low-energy tail is observed in the 14 K PL spectrum of the undoped $CsPbCl_3$ NCs that is attributable to radiative surface trap states (see Appendix). As doping increases, there is a dramatic increase in PL intensity of a near-band-edge (NBE) feature ~50 meV below the excitonic PL. The NBE-to-exciton PL intensity ratio (I_{NBE}/I_{exc}) increases 20-fold going from 1.5 to 9.3% Gd^{3+}, demonstrating that this NBE emission is indeed induced by Gd^{3+} doping. Figure 4.2B summarizes the exciton-to-NBE splitting energies (ΔE) from the data in Figure 4.2A, plotting ΔE *vs* the Gd^{3+} doping concentration. From this plot, ΔE increases slightly with increasing doping concentration, growing by ~3.5 meV per %Gd^{3+}. Overall, the NBE emission is qualitatively unchanged between 1.5 and 9.3% Gd^{3+}. Importantly, the half-filled ($4f^7$) ground electronic configuration of Gd^{3+} pushes its lowest-energy *f-f* and charge-transfer transitions all to very high energies (~4 eV), well above the perovskite energy gaps investigated here, so we can conclude that this NBE emission does not come from any electronic excited state of Gd^{3+} itself.

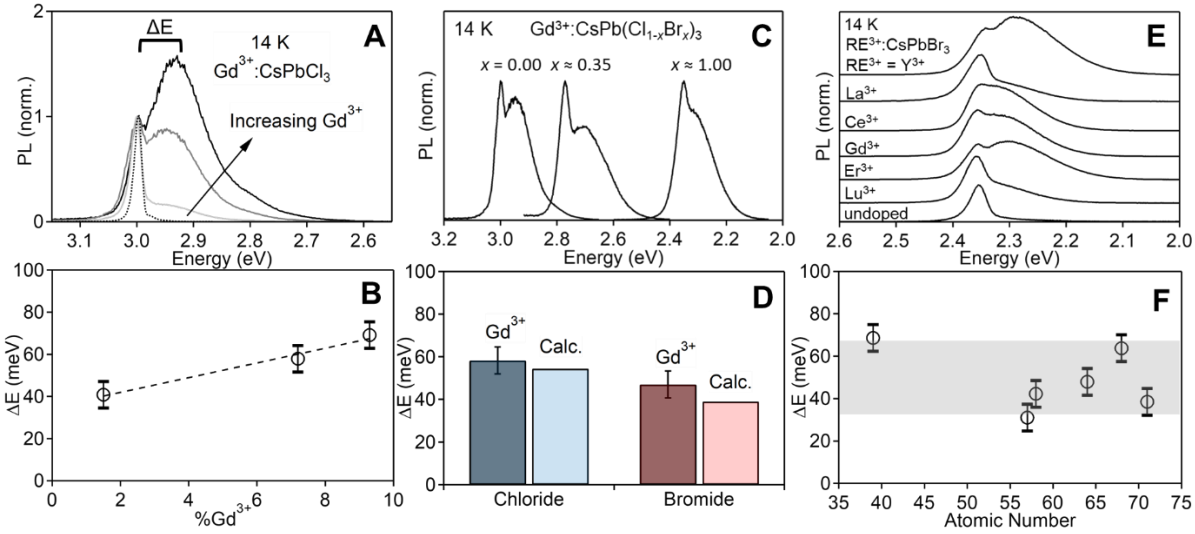

Figure 4.2 Low-Temperature PL of RE^{3+}:$CsPb(Cl_{1-x}Br_x)_3$ NCs.

(A) 14 K PL spectra of a series of Gd^{3+}:$CsPbCl_3$ NCs with different Gd^{3+} doping levels (1.5%, 7.2%, 9.3%), collected using CW 375 nm excitation. **(B)** The exciton-

to-NBE PL splitting energy, ΔE, plotted *vs* the Gd^{3+} B-site cation mole fraction, from panel A. The dashed line shows a linear best fit of the data, yielding the relationship ΔE = [35.0 + 3.5*(%Gd^{3+})] meV. **(C)** 14 K PL spectra of 7.1% Gd^{3+}:$CsPb(Cl_{1-x}Br_x)_3$ (x = 0.00, 0.35, 1.00) NCs, collected using 375 nm (x = 0) or 405 nm ($x \approx$ 0.35, 1.00) excitation. **(D)** Comparison of experimental ΔE values for Gd^{3+}-doped $CsPbCl_3$ and $CsPbBr_3$ NCs from panel C with calculated binding energies of the exciton to V_{Pb} in $CsPbCl_3$ and $CsPbBr_3$ (see text). **(E)** 14 K PL spectra of $CsPbBr_3$ NCs doped with 10.5% Y^{3+}, 8.5% La^{3+}, 7.6% Ce^{3+}, 10.3% Gd^{3+}, 9.6% Er^{3+}, and 7.4% Lu^{3+}. The bottom spectrum is of undoped $CsPbBr_3$ NCs. **(F)** ΔE plotted *vs* the RE^{3+} atomic number for the series of RE^{3+}-doped $CsPbBr_3$ NCs from panel E. The gray bar is a guide to the eye. The error bars on the experimental ΔE values are estimated from the fitting analysis (see Appendix).

To explore this NBE emission further, we examined its dependence on the $CsPb(Cl_{1-x}Br_x)_3$ energy gap, using anion exchange to tune that gap. ICP measurements performed before and after anion exchange and washing show no statistically significant change in the dopant concentration. Figure 4.2C plots the 14 K PL spectra of ~7.1% Gd^{3+}:$CsPb(Cl_{1-x}Br_x)_3$ NCs at three different bromide concentrations (x = 0.00, ~0.35, 1.00), all stemming from the same parent 7.1% Gd^{3+}:$CsPbCl_3$ NCs (x = 0.00). The NBE PL remains distinct below the excitonic PL in all compositions. When comparing x = 0.00 to x = 1.00, the NBE feature appears to be closer to the exciton in the latter. The NBE band shape is also noticeably broader in the intermediate (x = 0.35) spectrum, suggesting that its energy is sensitive to microscopic heterogeneities introduced in the mixed-halide composition. Figure 4.2D illustrates that ΔE *vs* x decreases from 58 meV at x = 0.00 to 47 meV at x = 1.00.

To test the assertion that the NBE PL observed in Gd^{3+}-doped $CsPb(Cl_{1-x}Br_x)_3$ NCs does not come from any electronic excited state of Gd^{3+} itself, we compare the low-temperature PL spectra of a series of RE^{3+}-doped $CsPbBr_3$ NCs, where RE^{3+} = Y^{3+}, La^{3+}, Ce^{3+}, Gd^{3+}, Lu^{3+}. Most of this series of RE^{3+} ions possess either closed- or half-filled *f*-shell configurations. Ce^{3+} ($4f^1$) often shows an *f-d* transition at relatively low energies, but this transition falls outside of the $CsPbBr_3$ band gap.[31] Figure 4.2E plots 14 K PL spectra of this series of samples in comparison with the spectrum of undoped $CsPbBr_3$ NCs. Although there are differences in I_{NBE}/I_{exc}, the characteristic NBE PL is observed in *every* RE^{3+}-doped NC sample of this series. Moreover, this NBE PL is not limited to spectroscopically innocent RE^{3+} dopants: Figure 4.2E also plots the low-temperature PL spectrum of 9.6% Er^{3+}:$CsPbBr_3$ NCs, and this, too, shows very similar NBE PL. The dependence of the NBE PL on halide in Er^{3+}:$CsPb(Cl_{1-x}Br_x)_3$ NCs is essentially identical to that shown in Figure

4.2C (see Appendix). No other lower-energy *f-f* emission is observed in any of these Er^{3+}-doped NCs. Figure 4.2F plots ΔE *vs* RE^{3+} atomic number for this RE^{3+}:$CsPbBr_3$ NC series, showing that in all cases, ΔE = 49 ± 15 meV. This result allows the conclusion that this NBE defect state is ubiquitous in RE^{3+}-doped $CsPbX_3$ perovskite NCs. We thus equate the spectroscopic energy difference (ΔE) with the binding energy (E_b) of an exciton to a dopant-induced defect.

To understand the properties of this NBE state in greater detail, we performed variable-temperature (VT) PL measurements. Figure 4.3A plots VTPL spectra of $CsPbBr_3$ NCs collected from 14 to 296 K. Like in the undoped $CsPbCl_3$ NCs, the low-temperature spectrum shows a weak tail below the exciton, attributed to surface states (see appendix). Figure 4.3B plots VTPL spectra collected over the same temperature range for 7.7% Gd^{3+}:$CsPbBr_3$ NCs. In both samples, I_{exc} increases with increasing temperature until ~90 K before turning over and decreasing again up to room temperature. In contrast, I_{NBE} in the Gd^{3+}:$CsPbBr_3$ NCs only decreases as the temperature increases, and by ~200 K this feature is no longer discernable. Figure 4.3C plots the total integrated PL intensity (I_{tot}) for both samples as a function of temperature and normalized to the intensity at 14 K. Despite the large spectral changes observed in the doped NC spectra, both samples show essentially the same gradual decrease of I_{tot} with increasing temperature. Figure 4.3D plots I_{exc}/I_{tot} and I_{NBE}/I_{tot} separately at each temperature for the Gd^{3+}:$CsPbBr_3$ NCs. I_{NBE}/I_{tot} is greatest at 14 K and decreases as the temperature is raised. I_{exc}/I_{tot} shows the opposite temperature dependence, such that by room temperature the PL spectrum is essentially entirely excitonic. Remarkably similar results were also found in a VTPL comparison of $CsPbCl_3$ and Gd^{3+}:$CsPbCl_3$ NCs (see appendix). These data show that the overall temperature dependence is independent of Gd^{3+} doping, and must therefore relate to other thermally activated nonradiative recombination pathways native to $CsPb(Cl_{1-x}Br_x)_3$ NCs, but changing the temperature dramatically alters the relative probabilities of NBE *vs* excitonic PL. Because of its lower energy, the NBE PL intensity increases as the temperature is lowered. These data also suggest that these two states are not in simple thermal equilibrium with one another, however, because in this limit, no excitonic PL would be observed at 14 K, given the ~50 meV binding energy of the NBE state (see Appendix).

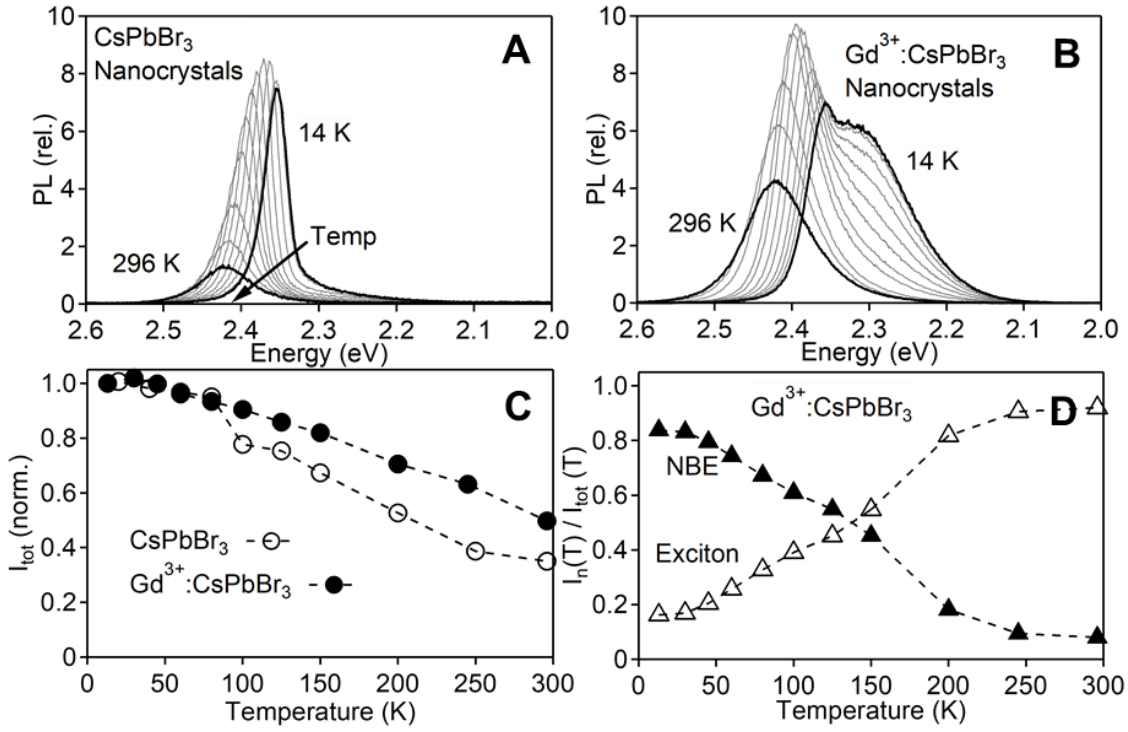

Figure 4.3 Variable-Temperature PL of $CsPbBr_3$ and Gd^{3+}:$CsPbBr_3$ NCs.

PL spectra measured from 14 to 296 K of **(A)** $CsPbBr_3$ and **(B)** 7.7% Gd^{3+}:$CsPbBr_3$ NCs, collected using CW 405 nm (3.06 eV) excitation. **(C)** Total integrated PL intensity plotted as a function of temperature, normalized to the PL intensity at 14 K (Open circles: $CsPbBr_3$ NCs; Solid circles: 7.7% Gd^{3+}:$CsPbBr_3$ NCs). The dashed lines are guides to the eye. **(D)** Temperature dependence of the integrated exciton (open triangles) and NBE (solid triangles) PL intensities from the 7.7% Gd^{3+}:$CsPbBr_3$ NC data in panel B, normalized to the total PL intensity at each temperature.

To examine the dynamics associated this NBE state, time-resolved PL measurements were performed at various temperatures and the results are summarized in Figure 4.4. Figures 4.4A,B plot representative streak-camera images of the first 20 ns of PL decay from $CsPbBr_3$ and 7.7% Gd^{3+}:$CsPbBr_3$ NCs, respectively, collected at 14 K. Figure 4.4C plots a streak-camera image of the same Gd^{3+}:$CsPbBr_3$ NC PL decay, but now covering a much longer time window (> 400 ns). Over the first 20 ns, the two samples show similar excitonic PL decay. Whereas no substantial further PL is observed in the undoped NCs, the Gd^{3+}:$CsPbBr_3$ NCs show additional NBE PL decay at lower energy and over longer times. Figures 4.4D,E plot excitonic PL decay traces for the undoped $CsPbBr_3$ and 7.7% Gd^{3+}:$CsPbBr_3$ NCs taken from such streak-camera images, and now

include data collected at several temperatures from 14 to 296 K. The doped and undoped NCs show very similar temperature dependence of their excitonic PL decay. At low temperatures, ~90% of the excitonic PL is depleted within ~2.5 ns for both samples. In both samples, the excitonic PL decay gets progressively slower as the temperature is raised, such that at room temperature it takes nearly 8 ns to deplete 90% of the excitonic PL in the undoped NCs and nearly 18 ns in the Gd^{3+}-doped NCs. Figure 4.4F plots PL decay curves for the NBE PL of the 7.7% Gd^{3+}:$CsPbBr_3$ NCs measured at the same series of temperatures. The NBE PL decay is much slower than the excitonic PL decay, and it appears independent of temperature until ~150 K, above which it begins to shorten slightly (See Appendix for complete analysis). Power-law behavior is noted for the last ~10% of NBE emission (see Appendix), suggesting delayed PL. Notably, the exciton and NBE decay dynamics never converge, as would be required in the limit of thermal equilibrium. These TRPL data thus confirm the conclusion drawn from the VTPL spectra that the exciton and NBE populations are not in simple thermal equilibrium with one another; a subset of excitons appears unaffected by the introduction of Gd^{3+}.

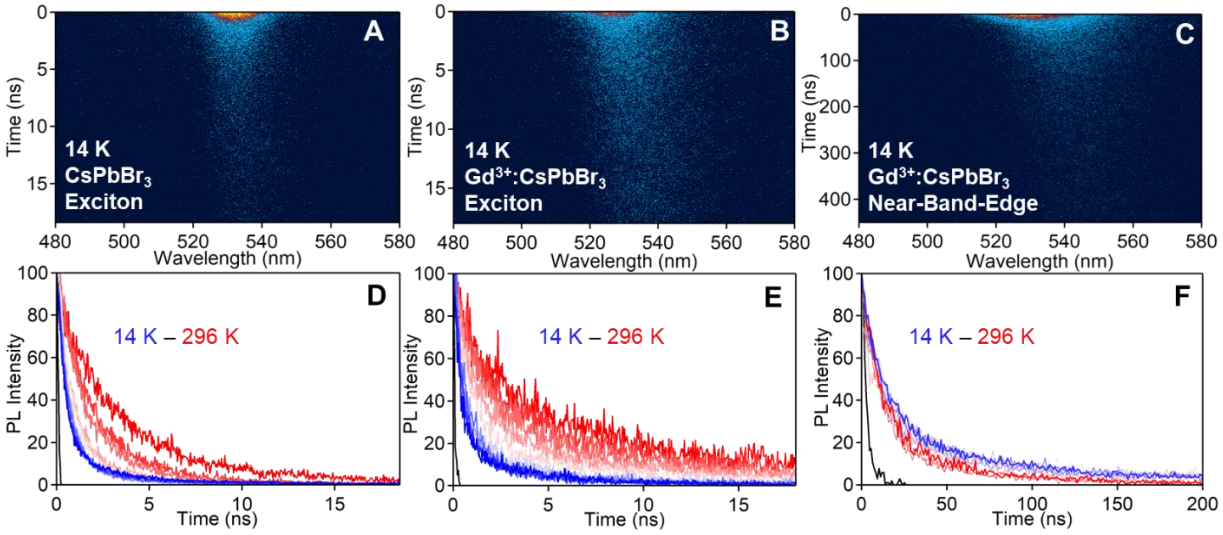

Figure 4.4 Variable-Temperature, Time-Resolved PL of $CsPbBr_3$ and Gd^{3+}:$CsPbBr_3$ NCs.

Streak-camera images of the 14 K TRPL from **(A)** $CsPbBr_3$ NCs and **(B, C)** 7.7% Gd^{3+}:$CsPbBr_3$ NCs. Note the long time scale of panel C. Similar streak-camera data were collected at multiple temperatures between 14 K and room temperature. **(D)** Variable-temperature exciton PL decay traces for the $CsPbBr_3$ NCs from panel A, measured from 14 K (blue) to room temperature (red), extracted from streak-camera data. **(E)** Variable-temperature exciton PL decay traces for the 7.7%

Gd^{3+}:$CsPbBr_3$ NCs, as in panel D. **(F)** Variable-temperature NBE PL decay traces for the 7.7% Gd^{3+}:$CsPbBr_3$ NCs, as in panel C. Note the long time scale of panel C. The black curves in panels D, E, and F show the instrument response functions for each measurement. For the Gd^{3+}:$CsPbBr_3$ NC decay traces in panels E and F, the exciton PL decay was integrated between 510-525 nm (13 – 80 K), 500-520 nm (100 – 150 K), or 490-515 nm (200 – 296 K), and the NBE PL was integrated between 535-585 nm (13 – 30 K) or 530-575 nm (45 – 150 K), or 520-555 nm (200 – 296 K) .

4.3 Thin Films

To test the potential role of high surface-to-volume ratios in generating this NBE PL, we prepared and examined the spectroscopy of analogous thermally evaporated thin films of $CsPbBr_3$ and Gd^{3+}:$CsPbBr_3$. Figure 4.5A shows photographs of representative thin films of $CsPbBr_3$ and 9.3% Gd^{3+}:$CsPbBr_3$, placed on top of white paper with drawn lines to illustrate their color, size, and transparency. Both perovskite films are ~0.2 μm thick. The films possess excellent optical quality, showing minimal scattering. Figure 4.5B plots X-ray diffraction data collected for the samples in Figure 4.5A. Both samples show diffraction consistent with orthorhombic $CsPbBr_3$. Figures 4.5C,D plot room-temperature absorption and PL spectra of the undoped and doped thin films, respectively. Both absorption spectra show a well-defined exciton peak at ~515 nm, and both also show sub-bandgap interference fringes consistent with the film thickness. Weak exciton emission is observed from both samples at room temperature. Overall, the two samples appear very similar at room temperature, just as the doped and undoped NCs did.

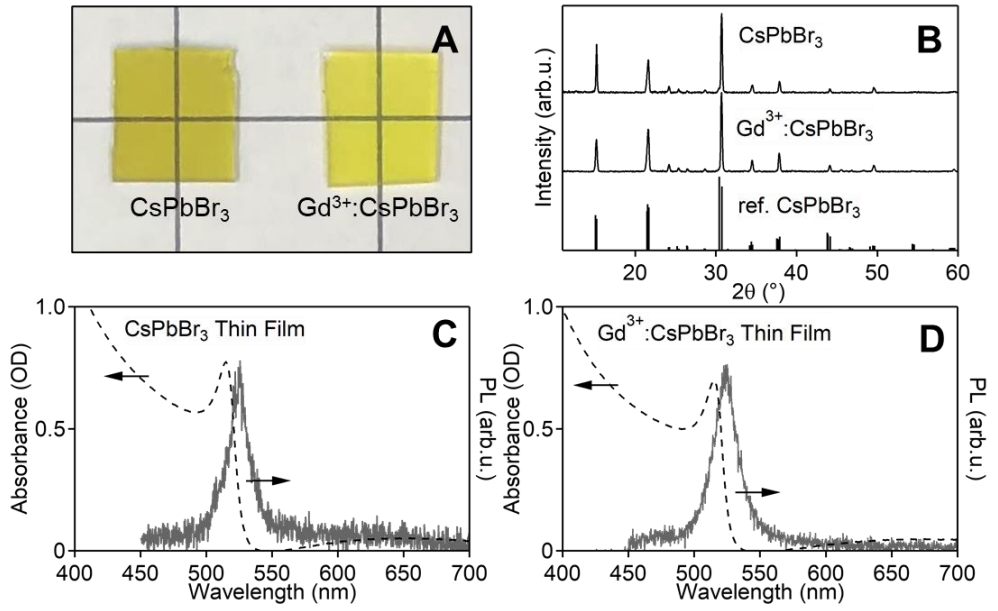

Figure 4.5 Characterization of Evaporated $CsPbBr_3$ and Gd^{3+}:$CsPbBr_3$ Thin Films.

(A) Photo of representative thermally evaporated perovskite thin films deposited on glass substrates. Left: $CsPbBr_3$; Right: 9.3% Gd^{3+}:$CsPbBr_3$. Grid spacing: 2 cm. Both films are ~0.2 μm thick **(B)** X-ray diffraction data for $CsPbBr_3$ and 9.3% Gd^{3+}:$CsPbBr_3$ thin films. A reference X-ray diffraction pattern for orthorhombic $CsPbBr_3$ is included for comparison.[30] Room-temperature absorption and PL spectra of representative **(C)** undoped $CsPbBr_3$ and **(D)** 9.3% Gd^{3+}-doped $CsPbBr_3$ thin films.

Figures 4.6A,B plot VTPL spectra of the $CsPbBr_3$ and 9.3% Gd^{3+}:$CsPbBr_3$ thin films measured from 15 to 296 K. Both samples show a distinct NBE emission feature ΔE ~ 50 meV below the exciton emission, but this feature is four times larger in the Gd^{3+}-doped sample at 15 K. The NBE PL bandshape is narrower in the Gd^{3+}-doped thin film than in the corresponding NCs, consistent with the conclusion drawn above that this feature is susceptible to inhomogeneous broadening. These results demonstrate that this NBE PL is indeed induced by Gd^{3+} doping. Because the surface-to-volume ratios of these thin films are orders of magnitude smaller than in the NCs, we conclude that the NBE PL is not associated with surfaces. These results also suggest that the NBE PL induced by Gd^{3+} doping has a native analog in undoped bulk $CsPbX_3$, *i.e.*, the native defect responsible for the NBE PL observed in the undoped $CsPbBr_3$ data of Figure 4.6A. A similar sub-bandgap PL feature has indeed been observed in other bulk $CsPbBr_3$ samples, but its assignment has varied. It has been attributed to bound excitons at structural defects, and to a Rashba effect induced by dynamic fluctuations in the position of the A-site cation, Cs^+.[32-34] For both samples in Figure 4.6, I_{exc} decreases rapidly with increasing temperature, in contrast with the NCs. Figure 4.6C plots $I_{tot}(T)/I_{tot}(15\ K)$ as a function of temperature for each sample. Both data sets show the same rapid decrease in I_{tot} between 15 and 80 K, indicative of efficient thermally activated nonradiative recombination. By room temperature, both samples have lost over 99% of their 15 K PL intensity. Figure 4.6D plots I_{exc}/I_{tot} and I_{NBE}/I_{tot} for the Gd^{3+}:$CsPbBr_3$ thin film, measured from 15 K to room temperature. I_{NBE}/I_{tot} is greatest at 15 K and decreases as the temperature is raised. By 40 K, I_{exc} exceeds I_{NBE}, and the latter drops to nearly 0 by ~70 K. The values of ΔE and the temperature dependence of both I_{exc}/I_{tot} and I_{NBE}/I_{tot} are thus very similar to those observed in the analogous NCs, despite the fact that the thin-film emission is far more susceptible to thermal quenching. This observation supports attribution of this NBE PL feature to the same RE^{3+}-induced

defect in both NC and thin-film samples.

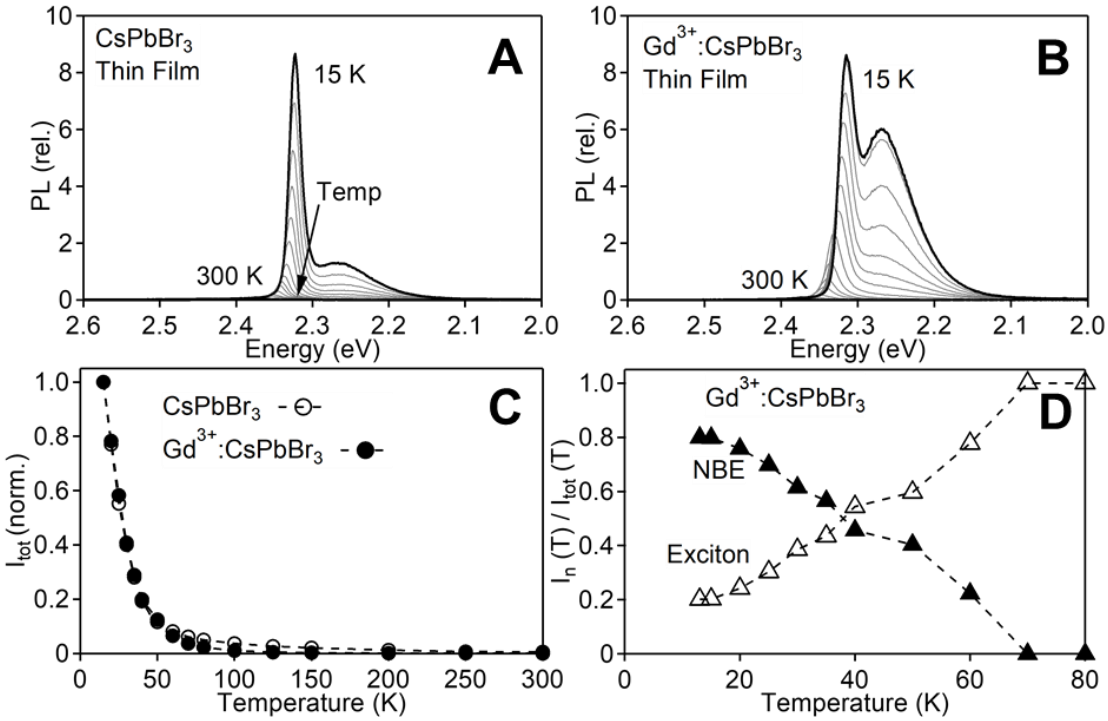

Figure 4.6 Variable-Temperature PL of Evaporated $CsPbBr_3$ and Gd^{3+}:$CsPbBr_3$ Thin Films.

Photoluminescence spectra of **(A)** 9.3% Gd^{3+}-doped $CsPbBr_3$ thin film and **(B)** $CsPbBr_3$ thin film collected at temperatures of 15, 20, 25, 30, 35, 40, 45, 50, 60, 70, 80, 100, 125, 150, 200, 250, 300 K. **(C)** Integrated PL intensities from panels A and B, plotted *vs* temperature. Open circles: $CsPbBr_3$; Filled circles: 9.3% Gd^{3+}:$CsPbBr_3$. **(D)** Temperature dependence of the integrated exciton (open triangles) and NBE (solid triangles) PL intensities from the Gd^{3+}:$CsPbBr_3$ data in panel B, normalized to the total PL intensity at each temperature.

4.4 Calculated Exciton-Binding Energies

Previously,[28] we applied first-principles electronic-structure calculations and a thermodynamic model to investigate the effects of Yb^{3+} doping in single-crystalline $CsPbCl_3$. These calculations identified conditions under which locally bound charge-neutral $[2Yb_{Pb} + V_{Pb}]^0$ defect complexes become prevalent and also revealed significant $[Yb_{Pb} + V_{Pb}]^-$ defect formation. Examination of the electronic properties of such defect complexes showed shallow binding of both electrons and holes. The predicted defect structures arise from the electrostatics of aliovalent doping and were thus largely independent of the specific RE^{3+} dopant, in good agreement with experiment (Figure

4.2). We now show that the shallow exciton binding predicted by these calculations follows the same trend as observed experimentally in Figures 4.2C,D.

To assist interpretation of the experimental data, we consider here charge-carrier trapping to a shallow defect. For illustration, we assume that a doubly charged Pb^{2+} vacancy (V_{Pb}^{2-}) provides the dominant contribution to an exciton bound by the charge-neutral $[2RE_{Pb} + V_{Pb}]^0$ defect complex, although the same conclusions are drawn for any shallow defect. In the Born-Oppenheimer adiabatic approximation, this shallow acceptor-bound exciton (AX) is described by the effective Hamiltonian,

$$H_{AX} = -\frac{1}{2}\nabla_1^2 - \frac{1}{2\sigma}\nabla_2^2 - \frac{q_d}{r_1} + \frac{q_d}{r_2} + V_H(r_{12}) \tag{4.1}$$

written in atomic units with respect to the electron effective mass (m_e^*) and the static dielectric constant (ϵ_s). The distances separating the conduction-band (CB) electron and valence-band (VB) hole from the V_{Pb}^{2-} are denoted r_1 and r_2, respectively, and the ratio of their effective masses is $\sigma = m_h^*/m_e^*$. The nominal charge state of the V_{Pb}^{2-} is $q_d = -2$, and its interactions with the excited electron-hole pair are screened according to ϵ_S of the material. In lead-halide perovskites, large differences between static and high-frequency (ϵ_∞) dielectric constants imply strong Fröhlich couplings,

$$\alpha_{e,h} = \frac{e^2}{\hbar}\left(\frac{1}{\epsilon_\infty} - \frac{1}{\epsilon_s}\right)\sqrt{\frac{m_{e,h}^*}{2E_{LO}}}, \tag{4.2}$$

between charge carriers and longitudinal optical (LO) phonons, with characteristic excitation energy, E_{LO}. To account for phonon screening effects, we model the electron-hole interaction following the work of Haken,[35-36]

$$V_H(r) = -\frac{e^2}{\epsilon_s r} - \frac{e^2}{2r}\left(\frac{1}{\epsilon_\infty} - \frac{1}{\epsilon_s}\right)\left(\mathrm{e}^{-\frac{r}{l_h}} + \mathrm{e}^{-\frac{r}{l_e}}\right) \tag{4.3}$$

where effective length scales for electron- and hole-polarons are defined by

$$l_{e,h} = \sqrt{\hbar^2/2m_{e,h}^*\,E_{LO}} \tag{4.4}$$

Dynamical screening by LO phonons also leads to renormalized effective masses,[37]

$$\tilde{m}_{e,h}^* = m_{e,h}^*\left(1 + \alpha_{e,h}/6\right) \tag{4.5}$$

which are accounted for in the kinetic energy terms in H_{AX}. For consistency, we treat the free exciton (X) with the same level of theory, described by the Hamiltonian

$$H_X = -\frac{1}{2}\nabla^2 + V_H(r) \tag{4.6}$$

in the center-of-mass frame of the free exciton. To parameterize these models, we used *ab initio* dielectric constants, effective masses, and LO phonon energies reported[38] for $CsPbX_3$ (X = Cl, Br, I) in the low-temperature, orthorhombic (*Pnma*) perovskite phase. These quantities were calculated from density functional theory (DFT) and the GW-Bethe-Salpeter equation (GW-BSE) method.[38] Ground states of H_{AX} and H_X were determined by the variational method.[28]

Table 1 summarizes the results of our variational ground-state calculations of free-exciton (E_X) and V_{Pb}^{2-}-bound-exciton (E_{AX}) energies, along with the specific *ab initio* parameters used for those calculations. Table 1 also includes experimental exciton-binding energies (E_X^{exp}) for comparison.[39-41] For $CsPbBr_3$, we find good agreement between our calculated E_X and the experimental values.[39-41] Although the discrepancy is larger for $CsPbCl_3$, it is smaller than for other reported computational values (*e.g.*, 146 meV in ref. [38]). We note that the authors of ref. [38] found reductions of 12% to 17% in the exciton binding energy in the $CsPbX_3$ series due to phonon screening.

Table 4.1. Parameterized *ab initio* constants and exciton energies in $CsPbX_3$ (X = Cl, Br, I) doped with RE^{3+} impurities. Experimental defect-binding energies (ΔE^{exp}, Gd^{3+}) from Figure 4.2 are compared with the difference between free-exciton and V_{Pb}^{2-}-bound-exciton energies, $\Delta E^{calc} = |E_{AX} - E_X|$.

	E_{LO} [meV]	ϵ_s	ϵ_∞	m_h^*	m_e^*	E_{AX} [meV]	E_X [meV]	E_X^{exp} [meV]	ΔE^{calc} [meV]	ΔE^{exp} [meV]
$CsPbCl_3$	26	17.5	3.7	0.28	0.30	-158.9	-104.4	-72,[39] -64[41]	54.5	58 ± 6
$CsPbBr_3$	18	18.6	4.5	0.20	0.21	-79.3	-40.3	-38,[39] -33[40]	39.0	47 ± 6
$CsPbI_3$	14	22.5	5.5	0.20	0.18	-44.9	-21.3	-15[40]	23.6	N/A

From these calculations, the energy differences $|E_{AX} - E_X|$ are then used to approximate the splitting energy between exciton and NBE emission probed experimentally. The calculations show $\Delta E^{calc} = |E_{AX} - E_X|$ decreasing as the halide atomic number increases in the $CsPbX_3$ series. This trend essentially reflects the changing dielectric constants across this series: Coulomb interactions are more effectively screened in lattices with heavier halides. Phonon screening does contribute to the predicted values of ΔE^{calc}, however. For example, the computed value of ΔE^{calc} in $CsPbCl_3$ neglecting phonon screening is 108.6 meV, compared to 54.5 meV in Table 4.1.

The calculated splitting energies are compared with the experimental values of ΔE in Table 1 and Figure 4.2D. The quantitative agreement between calculated and experimental magnitudes of ΔE may be fortuitous, given that these calculations have assumed that exciton binding is dominated by V_{Pb}^{2-}, whereas RE_{Pb}^{+} may also contribute significantly. For example, solving eq 4.3 for trapping an exciton to a single shallow +1 donor defect like RE_{Pb} yields $\Delta E^{\mathrm{calc}} = |E_{DX} - E_X|$ = 18.1 (Cl), 10.0 (Br), and 7.4 (I) eV, and carrier binding to a more complex defect cluster involving both donor and acceptor defects is even more complicated. Critically, the calculations predict the decrease in ΔE with increasing halide atomic number well, from which we conclude that the decrease in ΔE observed in Figure 4.2 on changing from RE^{3+}:$CsPbCl_3$ to RE^{3+}:$CsPbBr_3$ results from increased dielectric screening rather than from any specific electronic-structure property of the trap state itself (*e.g.*, relative electron *vs* hole binding). We note that we were unsuccessful in our attempts to synthesize RE^{3+}:$CsPbI_3$ NCs *via* anion exchange or direct methods; these calculations thus provide a prediction for ΔE in $CsPbI_3$ that remains to be tested experimentally.

4.5 RE^{3+} Doping, Shallow Defects, and Related Observations

The data and analysis presented above describe the appearance of a prominent NBE PL feature in $CsPb(Cl_{1-x}Br_x)_3$ NCs upon doping with RE^{3+} ions. Similar NBE PL features have been reported for other forms of $CsPbX_3$, both doped and undoped (*e.g.*, Figure 4.6A), but clear consensus about the origins of this NBE PL has not yet emerged. In many cases, this NBE PL has been attributed to surfaces. In $CsPbBr_3$ nanosheets, for example, low-temperature PL reveals a broad feature ~35 meV below the exciton that was attributed to trapped excitons.[42] Nanoscale $CsPbBr_3$ structures formed in Pb^{2+}-doped CsBr single crystals show a similar feature, attributed to trapping at $CsPbBr_3$/CsBr interfaces or electronic transitions associated with Pb^{2+}.[43] $CsPbBr_3$ NCs have also shown a similar NBE PL feature at 80 K (~70 meV below the exciton emission with a 10 ns lifetime), attributed to donor-acceptor pair luminescence involving surface-trapped carriers.[44] Similar NBE PL was also observed in the low-temperature spectra of La^{3+}:$CsPbCl_3$ NCs[12] and single crystals.

The results presented here demonstrate that RE^{3+} doping of $CsPbX_3$ universally generates such an NBE defect state. The RE^{3+} series examined here spans all of the lanthanides and additionally includes the $4d^0$ Y^{3+} ion as a pseudo-lanthanide, yet essentially the same NBE PL is observed in all cases, independent of the specific RE^{3+} dopant. Most of the RE^{3+} ions examined here possess

no internal *f-f* or charge-transfer excited states within the perovskite energy gap, indicating that this NBE PL must arise from a perturbation of the $CsPbX_3$ lattice and not from the dopant itself. The observation of the same NBE PL in Er^{3+}-doped $CsPb(Cl_{1-x}Br_x)_3$ NCs extends this conclusion to include RE^{3+} ions that do possess mid-gap internal states. We conclude that formation of this NBE defect state is a universal consequence of such aliovalent doping in perovskite $CsPbX_3$.

One common challenge in studying defects experimentally is their irreproducibility. The NBE defect generated by RE^{3+} doping is robust in ways not observed for the analogous native defects. For example, the native NBE PL in undoped $CsPbBr_3$ NCs can be changed and even completely suppressed through surface modification, whereas the NBE PL of RE^{3+}-doped NCs is insensitive to the same surface chemistry (see Appendix). This result suggests that the NBE state in RE^{3+}-doped $CsPbX_3$ resides within the internal volume of the lattice, a conclusion supported by the observation that similar NBE PL is induced by RE^{3+} doping in thin films with vastly smaller surface-to-volume ratios. These observations indicate that doping with spectroscopically innocent RE^{3+} ions offers a powerful tool for generating well-behaved defects in lead-halide perovskites.

The microscopic structure of this defect remains unclear. Recent first-principles electronic-structure calculations probing defect formation in Yb^{3+}-doped $CsPbCl_3$ have identified several locally bound and dissociated configurations of $[2Yb_{Pb} + V_{Pb}]^0$ with similar thermodynamics, and have predicted the prevalence of a series of closely related charge-neutral $[Yb\text{-}V_{Pb}\text{-}Yb]^0$ defect clusters at high Yb^{3+} concentrations.[28] DFT calculations on such clusters suggest their role as shallow electron traps rather than shallow hole traps.[45] DFT has also been used to predict that substitution of Pb^{2+} with Ce^{3+} in $CsPbBr_3$ (in the absence of additional charge-compensating defects) does not induce deep traps that quench exciton PL but rather promotes emission at or near the band edge.[6] An intriguing alternative possibility is that RE^{3+} dopants and their associated defects may locally polarize the perovskite lattice, lowering the site symmetry, and thereby enhancing the Rashba effect. In $CsPbBr_3$ nanocrystals, however, typical Rashba splittings observed in magneto-optical measurements are only ~1-2 meV,[46] *i.e.*, much smaller than the binding energies observed here. Preliminary magneto-PL measurements on these RE^{3+}-doped $CsPb(Cl_{1-x}Br_x)_3$ samples do show circular polarization of the NBE emission (see Appendix), but further measurements will be required to determine whether this polarization could be associated with a Rashba effect or just reflects the natural spin characteristics of a defect-bound exciton in this lattice.

These results may also have significant implications for understanding the mechanism of quantum cutting in Yb^{3+}:$CsPb(Cl_{1-x}Br_x)_3$ NCs and thin films. In this process, perovskite photoexcitation leads to energy-transfer excitation of two Yb^{3+} dopants simultaneously, allowing PL quantum yields to exceed 100%. Spectroscopic studies have identified signatures of an intermediate state in this energy-transfer process, residing between the $CsPb(Cl_{1-x}Br_x)_3$ exciton and the Yb^{3+} *f-f* excited states.[12, 22] This intermediate state depletes the exciton population on the picosecond time scale and passes that energy to Yb^{3+} with a time constant of ~8 ns at room temperature.[12, 22] The observations detailed above indicate that an NBE defect state is formed upon Yb^{3+} doping, even though NBE PL has not been observed in Yb^{3+}:$CsPb(Cl_{1-x}Br_x)_3$, presumably because of rapid energy capture by Yb^{3+}. The ubiquitous NBE state described here appears to be consistent with all of the known properties of the intermediate state in quantum cutting.

4.6 Conclusion

In summary, a combination of nanocrystal and thin-film synthesis, variable-temperature and time-resolved PL spectroscopy, and calculations of exciton-binding energies has been used to elucidate the impact of RE^{3+} doping on the electronic structures and photophysics of all-inorganic $CsPb(Cl_{1-x}Br_x)_3$ ($0 \leq x \leq 1$) lead-halide perovskites. The data show that RE^{3+} doping universally generates a new shallow defect state ca. 50 meV inside the perovskite band gap, regardless of the specific RE^{3+} dopant. Although most easily observed at low temperatures as the origin of a distinct PL band, this defect state is still influential at room temperature, leading to elongated PL decay times relative to the analogous undoped perovskite compositions. The appearance of this NBE PL even when doping with spectroscopically innocent RE^{3+} ions suggests it originates in the charge-compensating defects that accompany substitution of Pb^{2+} by RE^{3+}. Overall, these findings advance our general fundamental understanding of defects in lead-halide perovskites by demonstrating that controlled aliovalent RE^{3+} doping can be used to reproducibly tune the concentrations of well-behaved shallow defects, with potential ramifications for understanding and controlling the physical properties of metal-halide perovskites in various photovoltaic, electronic, and photonic technologies.

4.7 Experimental

Materials. 1-octadecene (ODE, 90%, Sigma Aldrich), oleylamine (OAm, 70%, Sigma

Aldrich), oleic Acid (OA, 90%, Sigma Aldrich), n-hexane (99%, Sigma Aldrich), ethyl acetate (EtOAc, 99%, Sigma Aldrich), ethanol (EtOH, 200 proof, Decon Laboratories, Inc.), trimethylsilyl chloride (TMS-Cl, 98%, Acros Organics), trimethylsilyl bromide (TMS-Br, 97%, Sigma Aldrich), lead (II) acetate trihydrate (99.999%, $Pb(OAc)_2 \cdot 3H_2O$, Sigma Aldrich), cesium acetate (CsOAc, 99.9%, Sigma Aldrich), yttrium (III) acetate hydrate (99.9%, $Y(OAc)_3 \cdot xH_2O$, Sigma Aldrich), lanthanum (III) acetate hydrate (99.9%, $La(OAc)_3 \cdot xH_2O$, Strem Chemical), cerium(III) acetate hydrate (99.9%, $Ce(OAc)_3 \cdot xH_2O$, Sigma Aldrich), gadolinium (III) acetate hydrate (99.9%, $Gd(OAc)_3 \cdot xH_2O$, Sigma Aldrich), erbium (III) acetate tetrahydrate (99%, $Er(OAc)_3 \cdot 4H_2O$, Alfa Aesar) and lutetium (III) acetate hydrate (99.9%, $Lu(OAc)_3 \cdot xH_2O$, Alfa Aesar) were used as received.

Synthesis and Purification of RE^{3+}:$CsPbCl_3$ nanocrystals. RE^{3+}-doped $CsPbCl_3$ NCs (RE^{3+} = Y^{3+}, La^{3+}, Ce^{3+}, Gd^{3+}, Lu^{3+}) were synthesized according to the protocol published earlier.[12] In a representative procedure, using Schlenk line techniques, an oven-dried, 3-neck flask containing 5 mL ODE, 0.25 mL OAm, 1 mL OA, 75 mg $Pb(OAc)_2 \cdot 3H_2O$, 12 mg $Gd(OAc)_3 \cdot xH_2O$, and 280 μL 1M CsOAc in EtOH was heated under vacuum at 110 °C for an hour before being flushed with N_2 and heated to 240 °C. Immediately upon reaching 240 °C, a room temperature TMS-Cl solution (0.5 mL ODE + 0.2 mL TMS-Cl) was injected, and the flask was cooled to room temperature using a water bath. The mother liquor was centrifuged at 1318 xg for 5 minutes, and the supernatant was discarded. The pellet was resuspended in n-hexane, and the NCs were flocculated out of solution with EtOAc. The suspension was centrifuged again for 5 min, and the supernatant was once again discarded. The pellet was resuspended in n-hexane and centrifuged for 10 min. The resulting supernatant containing the NCs was stored ambiently in the dark in a glass vial. These NCs stay in solution for ~2 weeks when stored in a dark drawer in ambient atmosphere but they can remain stable for several months if stored in inert atmosphere and dry solvent. For undoped NCs, no $RE(OAc)_3 \cdot xH_2O$ reagent was added to the reaction vessel and only 200 μL of the 1M Cs^+ solution was used.

Anion Exchange. RE^{3+}:$CsPbBr_3$ NCs were prepared by anion exchange using the chloride NCs described in the previous section, according to protocols outlined previously.[18, 47-48] Briefly, NCs were dispersed in dry solvent in a nitrogen-filled glovebox and titrated with 1 M TMS-Br until the desired band gap was obtained, as determined by absorption and PL spectroscopies. The solvent and residual TMS-X were then removed by vacuum evaporation. The NCs were

resuspended in dry hexane and stored in the glovebox.

Single-Source Vapor Deposition of 9.3% Gd^{3+}:$CsPbBr_3$ and $CsPbBr_3$ Thin Films. *Materials*. Cesium bromide (99.9%, CsBr, Alfa Aesar), lead (II) bromide (99.9%, $PbBr_2$, Alfa Aesar), and gadolinium (III) bromide (99.9%, $GdBr_3$, Alfa Aesar). *Deposition*. Vapor-deposited thin films were made via rapid thermal evaporation (single-source vapor deposition; SSVD) similar to a process we have reported earlier.[15, 49] First, CsBr, $PbBr_2$, and $GdBr_3$ were added in stoichiometric amounts to an agate mortar and pestle and ground for 10 minutes, until a yellow powder was formed. The powder was then annealed in air at 150 °C until it converted to an orange color. The SSVD was performed in a home-built evaporator comprising a bell jar, a roughing pump, a diffusion pump, and a high-current power supply. Approximately 60 mg of powder was loaded onto a Ta evaporation boat. Substrates (quartz for variable temperature photoluminescence) were sonicated in sodium thiosulfate, water, and hexanes in that order for cleaning. Substrates were suspended 13.5 cm above the evaporation boat. The chamber was evacuated to ~10^{-5} torr, and the powder was sublimated by passing a high current through the evaporation boat. The powder was deposited on to the substrate at a rate of ~1000 Å/s over an approximately 2 second window. The samples were immediately transferred to a nitrogen filled glove box where they were annealed at 150 °C for 10 min and subsequently stored until use.

Analytical Characterization. Powder X-ray diffraction data were measured with a Bruker D8 Discover with a high-efficiency IμS microfocus X-ray source for Cu Kα radiation operating at 50000 mW (50 kV, 1 mA). Samples were prepared by dropcasting NC stock solutions on silicon substrates or by thermally evaporating thin films onto glass substrates. Elemental analysis to determine NC doping concentrations was measured via ICP-AES using a PerkinElmer 8300. Samples were prepared by digesting the NC powders in concentrated nitric acid with sonication and diluting in ultrapure H_2O. TEM images were acquired with an FEI TECNAI F20 microscope operating at 200 kV. A narrow C2 aperture was used to minimize in-situ reduction of Pb^{2+} to Pb^0 by the electron beam. NC stock solutions were diluted by about one half and 5 μL of solution was deposited onto ultrathin carbon-coated copper grids from TED Pella, Inc.

Spectroscopic Measurements. All optical measurements were performed on NCs or thermally evaporated thin films deposited on quartz substrates. Absorption spectra were collected using an Agilent Cary 5000. PL measurements were performed with the sample loaded in a custom-built cryostat cooled by a closed-cycle helium compressor. An LN_2-cooled silicon CCD

was used for PL detection. All spectra have been corrected for the wavelength dependence of the instrument response. Chloride samples were excited using a focused 375 nm LED. Bromide samples were excited using a collimated 405 nm LED. Both LEDs were operated as continuous-wave (cw) excitation sources. Variable-temperature (VT) PL spectra were acquired at temperatures between 14 and 296 K with the sample under continuous illumination. The temperature was allowed to stabilize at each point before data collection. Low-temperature absorption spectra were collected using a Cary 5000 with the NCs dropcast on a quartz substrate and mounted in the same cryostat used for VTPL measurements.

Time-Resolved Photoluminescence (TRPL). For time-resolved PL measurements, NCs were dropcast onto quartz substrates and loaded into a closed-cycle helium cryostat. Samples were excited using the third harmonic of a Nd^{3+}:YAG laser (355 nm) firing with a repetition rate of 50 hz and having a 30 ps pulse width. The excitation flux was kept constant at 60 nJ/pulse. A Hamamatsu streak camera was used for PL detection. Temporal windows of 20 ns, 500 ns, 5 μs, and 50 μs were measured.

Experiment Demonstrating Reduction of Trap PL Following Surface Treatment (Appendix 4.1). *Materials used*. Lead acetate trihydrate (99.9%, $Pb(OAc)_2{\cdot}3H_2O$, Baker Chemical), cesium carbonate (99.9%, Cs_2CO_3, Sigma Aldrich), cesium acetate (99.9%, CsOAc Alfa Aesar), bromotrimethylsilane (97%, TMS-Br, Sigma Aldirch), 1-octadecene (90%, ODE Sigma Aldrich), oleylamine (70%, OAm Sigma Aldrich), oleic acid (90%, OA Sigma Aldrich), hexanes (99%, mixture of isomers, Sigma Aldrich), toluene (HPLC, Fischer Chemical), anhydrous ethyl acetate (99%, Sigma Aldrich), didodecyldimethylammonium bromide (98%, R_4NBr, Sigma Aldrich) were all used without further purification.

Synthesis of undoped $CsPbBr_3$ nanocrystals. Undoped $CsPbBr_3$ NCs were prepared following a published protocol.[50] Briefly, separately prepared and pre-heated solutions of cesium oleate and lead oleate were loaded into a 100 mL 3-neck round bottom flask in an N_2-filled glovebox. ODE and OAm were added once the flask was taken out of the glovebox. The precursors were degassed on a Schlenk line at 120 °C for 1-2 hr before being flushed with N_2 and heated to 180 °C. A solution of TMS-Br in dry ODE (180 and 400 uL, respectively) was injected into the precursor solution, resulting in the formation of NCs. The reaction was quenched after ~5 s with an ice water bath. Purification involved flocculating the NCs out of solution with excess anhydrous ethyl acetate, centrifuging at 1318 xg for 15 min, and resuspending in hexane. This purification was repeated

once more, and the NCs were then transferred to an N_2-filled glovebox and resuspended in hexane. $CsPbBr_3$ NCs doped with Gd^{3+} were prepared as detailed in the main text.

Ligand Exchange. Surface passivation of Gd^{3+}:$CsPbBr_3$ and $CsPbBr_3$ NCs was done by adapting a procedure reported for preparing high PLQY NCs.[51] Briefly, a small fraction of the NC stock solution was treated with 30 μL of neat OA and 50 mM didocyldimethylammonium bromide in toluene and stirred at room temperature for 5 min.

Magnetic Circularly Polarized Luminescence (MCPL) Spectroscopy (Appendix 4.2). Samples were prepared by dropcasting nanocrystal solutions onto quartz substrates. These samples were loaded into a LHe-cooled magneto-optical cryostat. Samples were excited with a CW 405 nm LED in an applied co-linear magnetic field whose strength was varied from 0 to 6 T. Emission was collected co-linearly and passed through a λ/4 plate and linear polarizer to separate left- and right-circularly polarized light. The emission was then coupled into a fiber-optic cable attached to a monochrometer and detected using a LN_2-cooled CCD.

4.8 Acknowledgments

The following people contributed to this chapter: J.Y. Diana Roh performed TRPL measurements; Laura M. Jacoby and Matthew J. Crane prepared and characterized thin film samples and assisted with VTPL measurements; David E. Sommer and Scott T. Dunham carried out calculations to determine the origin of the changing NBE-to-exciton splitting energy; Daniel R. Gamelin provided helpful discussion and supervised all the work.

This work was primarily supported by the U.S. National Science Foundation through the University of Washington Molecular Engineering Materials Center, a Materials Research Science and Engineering Center (DMR-1719797 to D.R.G. and S.T.D.). Additional support from the U.S. National Science Foundation (DMR-1807394 to D.R.G.) is gratefully acknowledged. The authors thank the Research Corporation for Science Advancement (RCSA) for supporting this research *via* a 2021 Cottrell Fellowships Award (award #27993) to D.R.G. in support of M.J.C.. Part of this work was conducted at the Molecular Analysis Facility, a National Nanotechnology Coordinated Infrastructure (NNCI) site at the University of Washington, which is supported in part by funds from the National Science Foundation (awards NNCI-2025489, NNCI-1542101), the Molecular Engineering & Sciences Institute, and the Clean Energy Institute. Dr. Samantha Young is acknowledged for acquiring XRD data. Dr. Ellen Lavoie and Atch Gopalan are acknowledged for

acquiring TEM images.

References

1. Jena, A. K.; Kulkarni, A.; Sanehira, Y.; Ikegami, M.; Miyasaka, T. *Chem. Mater.* **2018,** *30*, 6668-6674.
2. Shi, J.; Li, F.; Yuan, J.; Ling, X.; Zhou, S.; Qian, Y.; Ma, W. *J. Mater. Chem. A* **2019,** *7*, 20936-20944.
3. Duan, J.; Zhao, Y.; Yang, X.; Wang, Y.; He, B.; Tang, Q. *Adv. Energy Mater.* **2018,** *8*, 1802346.
4. Liu, Y.; Pan, G.; Wang, R.; Shao, H.; Wang, H.; Xu, W.; Cui, H.; Song, H. *Nanoscale* **2018,** *10*, 14067-14072.
5. Yao, J.-S.; Ge, J.; Han, B.-N.; Wang, K.-H.; Yao, H.-B.; Yu, H.-L.; Li, J.-H.; Zhu, B.-S.; Song, J.-Z.; Chen, C.; Zhang, Q.; Zeng, H.-B.; Luo, Y.; Yu, S.-H. *J. Am. Chem. Soc.* **2018,** *140*, 3626-3634.
6. Yin, J.; Ahmed, G. H.; Bakr, O. M.; Brédas, J.-L.; Mohammed, O. F. *ACS Energy Lett.* **2019**, 789-795.
7. Guvenc, C. M.; Yalcinkaya, Y.; Ozen, S.; Sahin, H.; Demir, M. M. *J. Phys. Chem. C* **2019,** *123*, 24865-24872.
8. Pan, G.; Bai, X.; Yang, D.; Chen, X.; Jing, P.; Qu, S.; Zhang, L.; Zhou, D.; Zhu, J.; Xu, W.; Dong, B.; Song, H. *Nano Lett.* **2017,** *17*, 8005-8011.
9. Zhou, D.; Sun, R.; Xu, W.; Ding, N.; Li, D.; Chen, X.; Pan, G.; Bai, X.; Song, H. *Nano Lett.* **2019,** *19*, 6904-6913.
10. Zhou, D.; Liu, D.; Pan, G.; Chen, X.; Li, D.; Xu, W.; Bai, X.; Song, H. *Adv. Mater.* **2017**, 1704149.
11. Kroupa, D. M.; Roh, J. Y.; Milstein, T. J.; Creutz, S. E.; Gamelin, D. R. *ACS Energy Lett.* **2018,** *3*, 2390-2395.
12. Milstein, T. J.; Kroupa, D. M.; Gamelin, D. R. *Nano Lett.* **2018,** *18*, 3792-3799.
13. Zhang, X.; Zhang, Y.; Zhang, X.; Yin, W.; Wang, Y.; Wang, H.; Lu, M.; Li, Z.; Gu, Z.; Yu, W. W. *J. Mater. Chem. C* **2018,** *6*, 10101-10105.
14. Cohen, T. A.; Milstein, T. J.; Kroupa, D. M.; MacKenzie, J. D.; Luscombe, C. K.; Gamelin, D. R. *J. Mater. Chem. A* **2019,** *7*, 9279-9288.
15. Crane, M. J.; Kroupa, D. M.; Roh, J. Y.; Anderson, R. T.; Smith, M. D.; Gamelin, D. R. *ACS Appl. Energy Mater.* **2019,** *2*, 4560-4565.
16. Erickson, C. S.; Crane, M. J.; Milstein, T. J.; Gamelin, D. R. *J. Phys. Chem. C* **2019,** *123*, 12474-12484.
17. Luo, X.; Ding, T.; Liu, X.; Liu, Y.; Wu, K. *Nano Lett.* **2019,** *19*, 338-341.
18. Milstein, T. J.; Kluherz, K. T.; Kroupa, D. M.; Erickson, C. S.; De Yoreo, J. J.; Gamelin, D. R. *Nano Lett.* **2019,** *19*, 1931-1937.
19. Cai, T.; Wang, J.; Li, W.; Hills-Kimball, K.; Yang, H.; Nagaoka, Y.; Yuan, Y.; Zia, R.; Chen, O. *Adv. Sci.* **2020,** *7*, 2001317.
20. Ding, N.; Xu, W.; Zhou, D.; Ji, Y.; Wang, Y.; Sun, R.; Bai, X.; Zhou, J.; Song, H. *Nano Energy* **2020,** *78*, 105278.
21. Ishii, A.; Miyasaka, T. *J. Chem. Phys.* **2020,** *153*, 194704.
22. Roh, J. Y. D.; Smith, M. D.; Crane, M. J.; Biner, D.; Milstein, T. J.; Krämer, K. W.; Gamelin, D. R. *Phys. Rev. Mater.* **2020,** *4*, 105405.

23. Zeng, M.; Artizzu, F.; Liu, J.; Singh, S.; Locardi, F.; Mara, D.; Hens, Z.; Van Deun, R. *ACS Appl. Nano Mater.* **2020,** *3*, 4699-4707.
24. Zhu, Y.; Pan, G.; Shao, L.; Yang, G.; Xu, X.; Zhao, J.; Mao, Y. *J. Alloys Compd.* **2020,** *835*, 155390.
25. Huang, H.; Li, R.; Jin, S.; Li, Z.; Huang, P.; Hong, J.; Du, S.; Zheng, W.; Chen, X.; Chen, D. *ACS Appl. Mater. Interfaces* **2021,** *13*, 34561-34571.
26. Xu, K.; Chen, D.; Huang, D.; Zhu, H. *J. Lumin.* **2021,** *240*, 118464.
27. Chang, W. J.; Irgen-Gioro, S.; Padgaonkar, S.; López-Arteaga, R.; Weiss, E. A. *J. Phys. Chem. C* **2021,** *125*, 25634-25642.
28. Sommer, D. E.; Gamelin, D. R.; Dunham, S. T. *Phys. Rev. Mater.*, in press.
29. Protesescu, L.; Yakunin, S.; Bodnarchuk, M. I.; Krieg, F.; Caputo, R.; Hendon, C. H.; Yang, R. X.; Walsh, A.; Kovalenko, M. V. *Nano Lett.* **2015,** *15*, 3692-3696.
30. Linaburg, M. R.; McClure, E. T.; Majher, J. D.; Woodward, P. M. *Chem. Mater.* **2017,** *29*, 3507-3514.
31. Quarati, F. G. A.; Dorenbos, P.; van der Biezen, J.; Owens, A.; Selle, M.; Parthier, L.; Schotanus, P. *Nucl. Instrum. Methods Phys. Res., Sect. A* **2013,** *729*, 596-604.
32. Steele, J. A.; Puech, P.; Monserrat, B.; Wu, B.; Yang, R. X.; Kirchartz, T.; Yuan, H.; Fleury, G.; Giovanni, D.; Fron, E.; Keshavarz, M.; Debroye, E.; Zhou, G.; Sum, T. C.; Walsh, A.; Hofkens, J.; Roeffaers, M. B. J. *ACS Energy Lett.* **2019,** *4*, 2205-2212.
33. Dendebera, M.; Chornodolskyy, Y.; Gamernyk, R.; Antonyak, O.; Pashuk, I.; Myagkota, S.; Gnilitskyi, I.; Pankratov, V.; Vistovskyy, V.; Mykhaylyk, V.; Grinberg, M.; Voloshinovskii, A. *J. Lumin.* **2020,** *225*, 117346.
34. Ryu, H.; Park, D. Y.; McCall, K. M.; Byun, H. R.; Lee, Y.; Kim, T. J.; Jeong, M. S.; Kim, J.; Kanatzidis, M. G.; Jang, J. I. *J. Am. Chem. Soc.* **2020,** *142*, 21059-21067.
35. Haken, H. *Z. Physik* **1956,** *146*, 527-554.
36. Haken, H. *Fortschritte der Physik* **1958,** *6*, 271-334.
37. Feynman, R. P. *Phys. Rev.* **1955,** *97*, 660-665.
38. Filip, M. R.; Haber, J. B.; Neaton, J. B. *Phys. Rev. Lett.* **2021,** *127*, 067401.
39. Zhang, Q.; Su, R.; Liu, X.; Xing, J.; Sum, T. C.; Xiong, Q. *Adv. Funct. Mater.* **2016,** *26*, 6238-6245.
40. Yang, Z.; Surrente, A.; Galkowski, K.; Miyata, A.; Portugall, O.; Sutton, R. J.; Haghighirad, A. A.; Snaith, H. J.; Maude, D. K.; Plochocka, P.; Nicholas, R. J. *ACS Energy Lett.* **2017,** *2*, 1621-1627.
41. Baranowski, M.; Plochocka, P.; Su, R.; Legrand, L.; Barisien, T.; Bernardot, F.; Xiong, Q.; Testelin, C.; Chamarro, M. *Photonics Res.* **2020,** *8*, A50-A55.
42. Lao, X.; Yang, Z.; Su, Z.; Wang, Z.; Ye, H.; Wang, M.; Yao, X.; Xu, S. *Nanoscale* **2018,** *10*, 9949-9956.
43. Nikl, M.; Nitsch, K.; Mihóková, E.; Polák, K.; Fabeni, P.; Pazzi, G. P.; Gurioli, M.; Santucci, S.; Phani, R.; Scacco, A.; Somma, F. *Phys. E (Amsterdam, Neth.)* **1999,** *4*, 323-331.
44. Han, Q.; Wu, W.; Liu, W.; Yang, Q.; Yang, Y. *J. Lumin.* **2018,** *198*, 350-356.
45. Li, X.; Duan, S.; Liu, H.; Chen, G.; Luo, Y.; Ågren, H. *J. Phys. Chem. Lett.* **2019**, 487-492.
46. Isarov, M.; Tan, L. Z.; Bodnarchuk, M. I.; Kovalenko, M. V.; Rappe, A. M.; Lifshitz, E. *Nano Lett.* **2017,** *17*, 5020-5026.
47. Creutz, S. E.; Crites, E. N.; De Siena, M. C.; Gamelin, D. R. *Chem. Mater.* **2018,** *30*, 4887–4891.

48. Creutz, S. E.; Crites, E. N.; De Siena, M. C.; Gamelin, D. R. *Nano Lett.* **2018,** *18*, 1118-1123.
49. Kroupa, D. M.; Crane, M. J.; Gamelin, D. R. *Proc. SPIE* **2019**, 11084-0J.
50. Cohen, T. A.; Huang, Y.; Bricker, N. A.; Juhl, C. S.; Milstein, T. J.; MacKenzie, J. D.; Luscombe, C. K.; Gamelin, D. R. *Chem. Mater.* **2021,** *33*, 3779-3790.
51. Rainò, G.; Landuyt, A.; Krieg, F.; Bernasconi, C.; Ochsenbein, S. T.; Dirin, D. N.; Bodnarchuk, M. I.; Kovalenko, M. V. *Nano Lett.* **2019,** *19*, 3648-3653.

4.9 Appendices

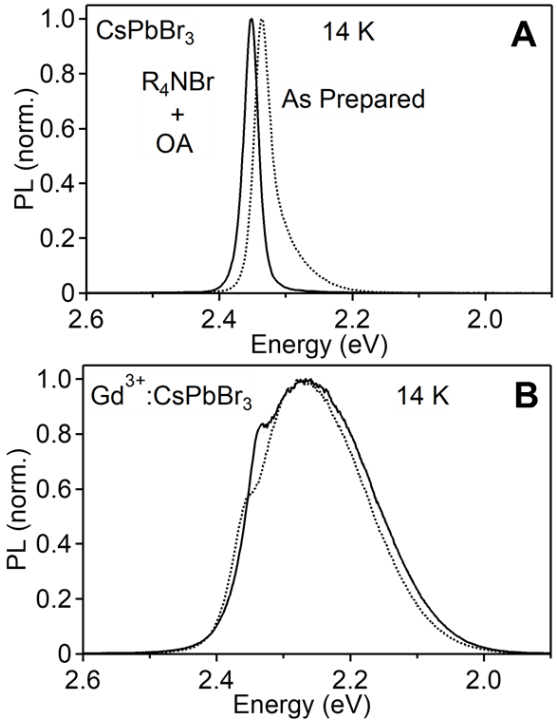

Appendix 4.1. Low-temperature PL spectra of undoped and Gd^{3+}-doped $CsPbBr_3$ before and after surface treatment. 14 K PL spectra of **(A)** $CsPbBr_3$ and **(B)** 11% Gd^{3+}:$CsPbBr_3$ NCs before (dotted) and after (solid) treatment with didodecyldimethylammonium bromide (R_4NBr) and oleic acid (OA) ligands. A shallow sub-band tail is observed below the exciton in the as-prepared NCs. This tail is no longer observed after ligand addition, suggesting that it arises from native traps on the NC surfaces. The same surface treatment does not eliminate the NBE emission in the Gd^{3+}:$CsPbBr_3$ NCs, indicating that this NBE emission does not come from the same NC surface defects.

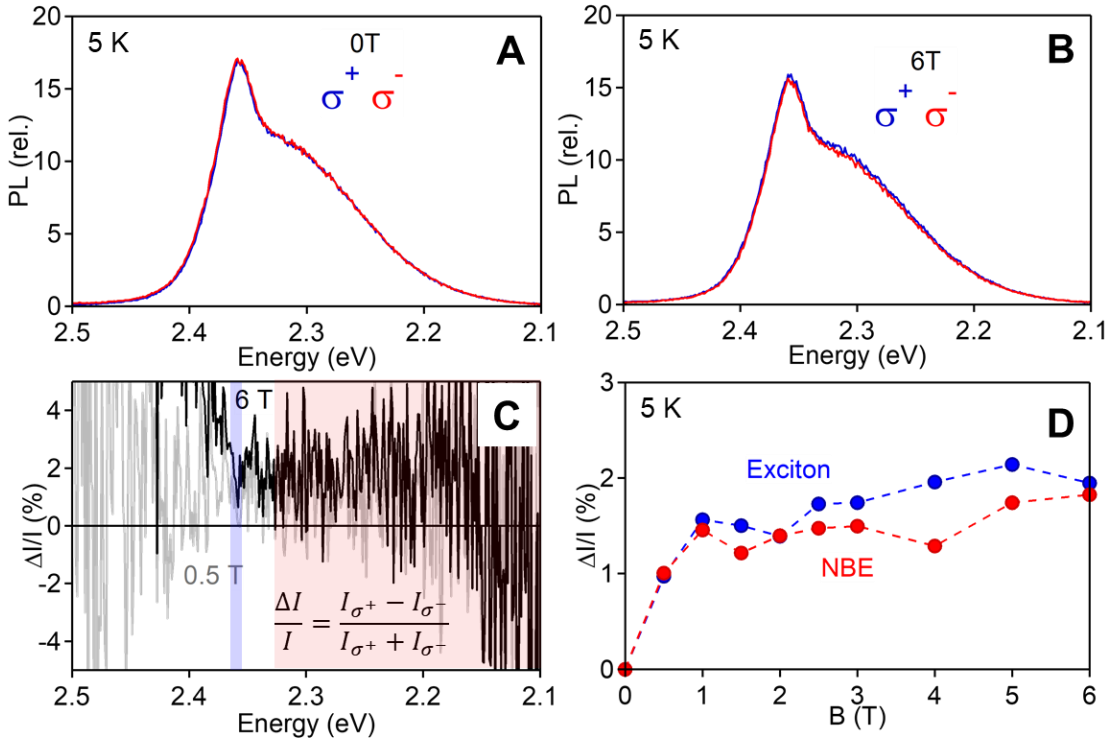

Appendix 4.2. MCPL monitoring of Gd^{3+}:$CsPbBr_3$ nanocrystal emission. 5 K MCPL spectra of 7.7% Gd^{3+}:$CsPbBr_3$ NCs collected at **(A)** 0 T and **(B)** 6 T. Blue: RCP (σ^+); Red: LCP (σ^-). **(C)** 5 K MCPL polarization ratio, $\Delta I/I$, measured at 6 T (black) and at 0.5 T (gray). Shaded areas denote (blue) exciton and (red) NBE energy ranges integrated to construct panel D. **(D)** $\Delta I/I$ for the exciton (blue, 2.35 to 2.37 eV) and NBE PL (red, 2.10 to 2.33 eV), plotted *vs* magnetic field strength, ***B***(T). The dashed lines are guides to the eye.

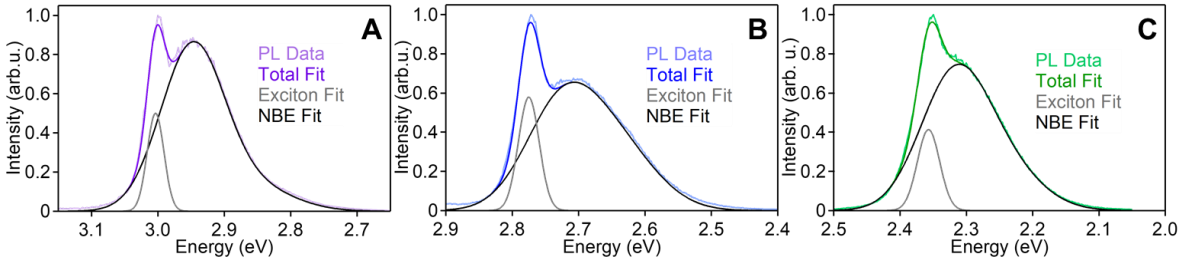

Appendix 4.3. Deconvolution of the 14 K PL spectra of 7.1% Gd^{3+}:$CsPb(Cl_{1-x}Br_x)_3$ NCs in which x = **(A)** 0.00, **(B)** ~0.35, and **(C)** 1.00, from Figure 4.2C. Exciton (gray), NBE (black), total (colored = gray + black).

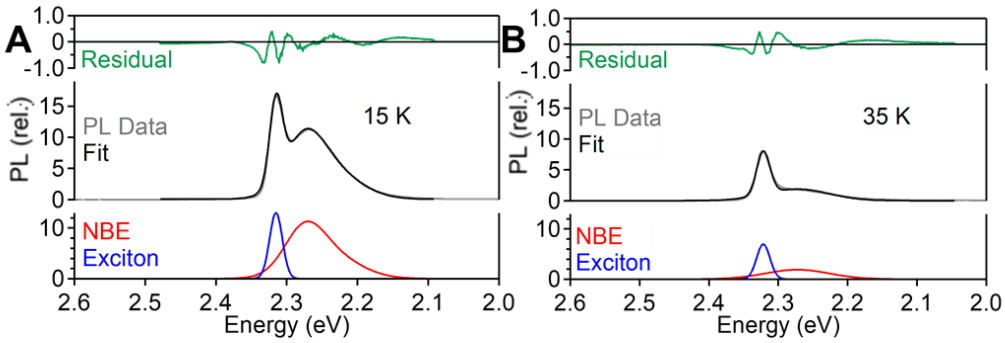

Appendix 4.4. Spectral deconvolution of the **(A)** 15 and **(B)** 35 K PL spectra of 9.3% Gd^{3+}:$CsPbBr_3$ thin films from Figure 4.6 of the main text. Each panel plots the experimental data (middle, grey), the total fit function (middle, black), the deconvolved exciton (bottom, blue) and NBE (bottom, red) features, and the fitting residual (top, green).

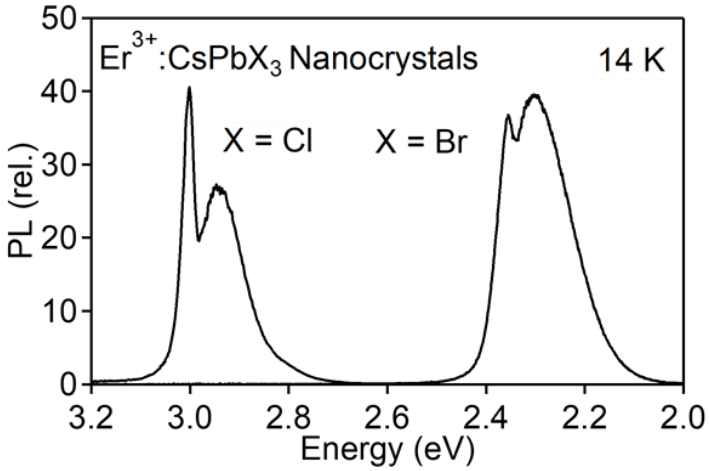

Appendix 4.5. 14 K PL spectra of 9.6% Er^{3+}:$CsPbX_3$ (X = Cl, Br) NCs. No other emission was observed for either sample at any temperature between 14 and 296 K.

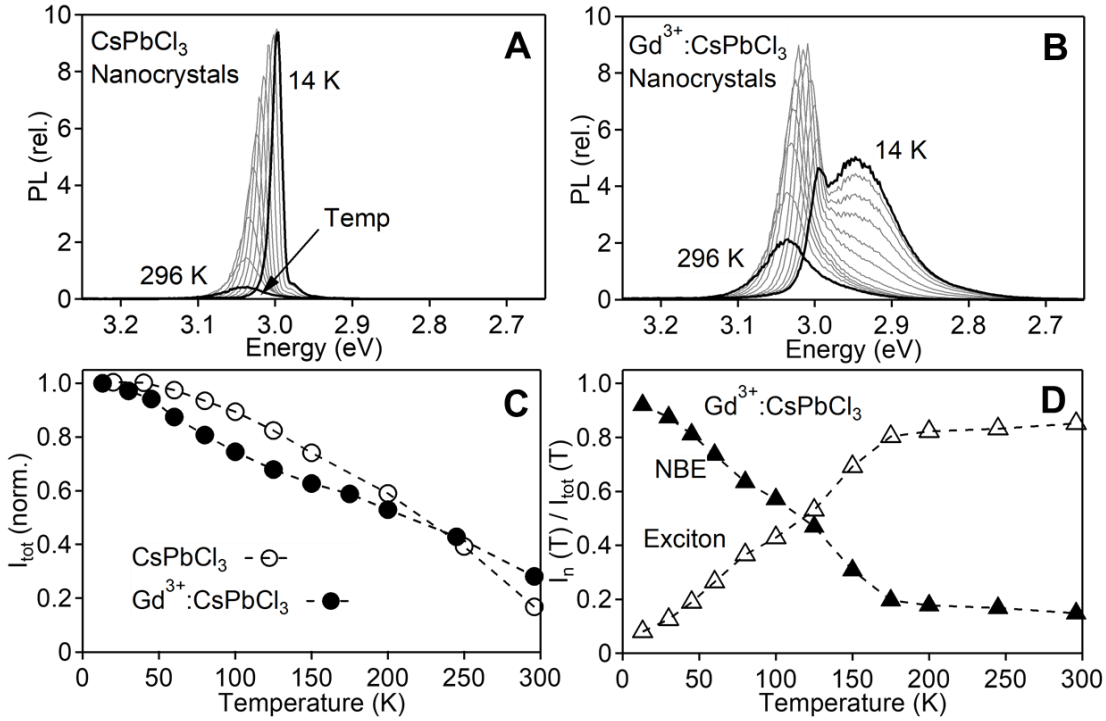

Appendix 4.6. Variable-temperature PL spectra measured from 13 to 296 K of **(A)** $CsPbCl_3$ and **(B)** 7.7% Gd^{3+}:$CsPbCl_3$ NCs, collected using CW 375 nm excitation. **(C)** Total integrated PL intensity plotted as a function of temperature normalized to the PL intensity at 14 K (Open circles: $CsPbCl_3$ NCs. Solid circles: 7.7% Gd^{3+}:$CsPbBr_3$ NCs). The dashed lines are guides to the eye. **(D)** Integrated exciton (open triangles) and NBE (closed triangles) PL intensities normalized to the total intensity at each temperature. The lines are guides to the eye.

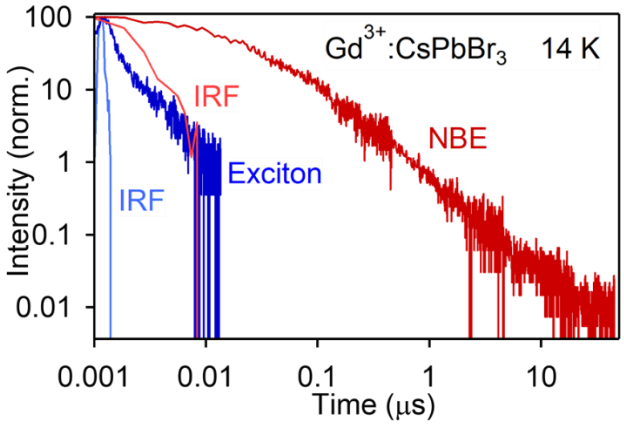

Appendix 4.7. Double-log plot of the 14 K exciton (blue) and NBE (red) PL decay measured for 7.7% Gd^{3+}:$CsPbBr_3$ NCs. The respective IRF traces are also plotted. Power-law decay is observed at long times, suggesting delayed luminescence.

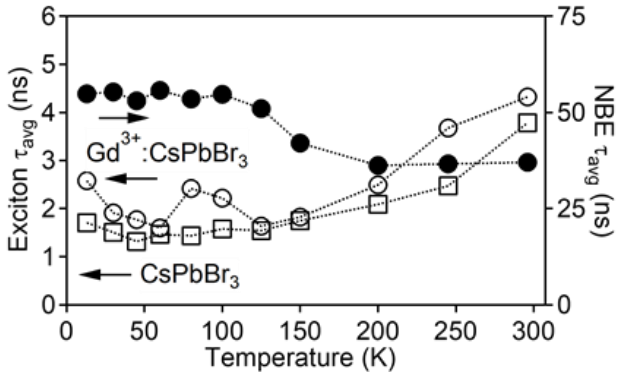

Appendix 4.8. Average PL decay times, τ_{avg}, obtained by fitting the data from Figure 4.4 of the main text using Appendix eq 4.1, plotted *vs* temperature. The dotted lines are guides to the eye. Open squares: $CsPbBr_3$ NC exciton; open circles: 7.7% Gd^{3+}:$CsPbBr_3$ exciton; solid circles: 7.7% Gd^{3+}:$CsPbBr_3$ NBE.

$$\tau_{\text{avg}} = \frac{\sum \tau_n^2 * A_n}{\sum \tau_n * A_n} \qquad \text{(App. 4.1)}$$

The time constants (τ_n) and amplitudes (A_n) of the fast (n = 1) and slow (n = 2) PL decay components were extracted from the data in Figures 4.4A-C of the main text (replotted in a semi-log representation in Appendix Figures 4.9A-C) by fitting to the bi-exponential decay function of Appendix eq 4.2, and the results are plotted in Appendix Figure 4.9D-I.

$$I(t) = A_1 e^{-\frac{t}{\tau_1}} + A_2 e^{-\frac{t}{\tau_2}} \qquad \text{(App. 4.2)}$$

I(t) represents the time-dependent PL intensity. At low temperature, the fast component of the exciton decay in both samples is sub-nanosecond and accounts for ~80% of emitted photons. With increasing temperature, both components of the exciton decay get slightly slower, and the relative amplitude of the fast component decreases substantially. The NBE PL also decays bi-exponentially, with lifetimes of 11 and 70 ns at low temperature. The fast component dominates (75-80%) at all temperatures. With increasing temperature, the slow component appears to accelerate, but overall, the changes are fairly small. Although NBE PL is not clearly observed at high temperatures in the Gd^{3+}:$CsPbBr_3$ NCs, the influence of the NBE state persists up to room temperature, as evidenced by the slow exciton decay in the Gd^{3+}:$CsPbBr_3$ NCs compared to undoped $CsPbBr_3$ NCs (Appendix 4.9-4.10).

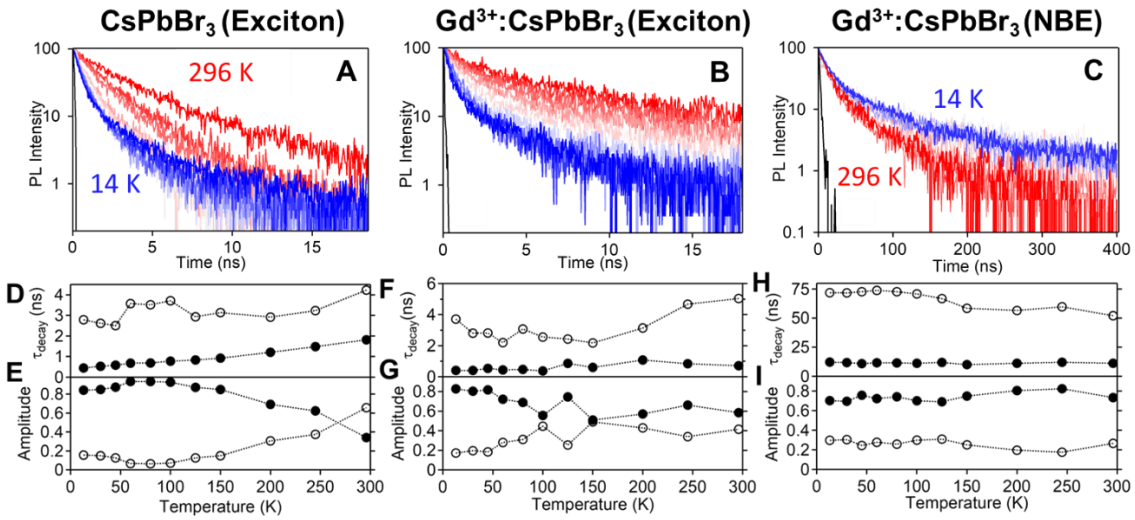

Appendix 4.9. Semi-log plots of the VT-TRPL data shown in Figure 4.4 of the main text. **(A)** $CsPbBr_3$ NCs, and **(B)** exciton and **(C)** NBE emission of 7.7% Gd^{3+}:$CsPbBr_3$ NCs. Note the different time scale of panel C. The black curves at short times in panels A, B, and C show the instrument response functions for these measurement conditions. **(D-I)** Summary of the VT-TRPL data from panels A-C. (panels D, F, H) Time constants and (panels E, G, I) amplitudes obtained from fitting the data in panels A-C using the bi-exponential function of Appendix eq 4.2. Solid circles: fast component (A_1 and τ_1). Open circles: slow component (A_2 and τ_2). The dotted lines are guides to the eye.

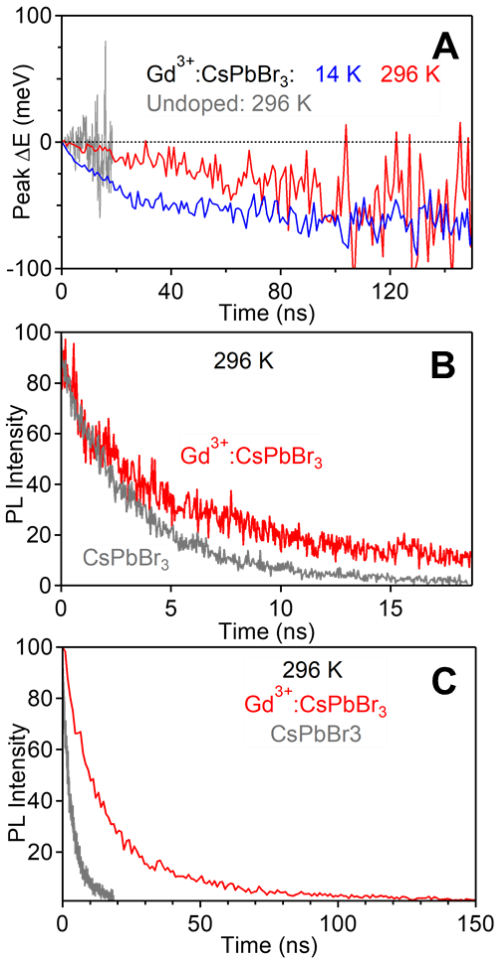

Appendix 4.10. Fingerprints of NBE emission at room temperature. **(A)** Relative average energies (in meV) of all emitted photons measured for (gray) $CsPbBr_3$ and (red) 7.7% Gd^{3+}:$CsPbBr_3$ NCs, plotted *vs* time at 296 K. The blue trace plots the relative average energies measured for the same Gd^{3+}:$CsPbBr_3$ NCs at 14 K. Room-temperature PL decay curves plotted over the first **(B)** 18 ns and **(C)** 150 ns for the samples from panel A.

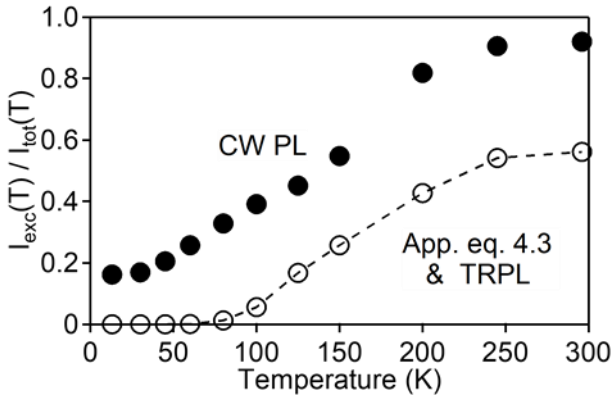

Appendix 4.11. $I_{exc}(T)/I_{tot}(T)$ plotted *vs* temperature, from the spectra in Figure 4.3 of the main text. The open circles plot the function described by Appendix eq 4.3 for the following parameters: ΔE = 55 meV, measured from the difference in exciton and NBE PL peak maxima at 14 K; $k_{exc}(T) = 1/\tau_{exc,avg}(T)$, from the undoped exciton TRPL data summarized in Appendix Figure 4.7; $k_{NBE}(T) = 1/\tau_{NBE,avg}(T)$, from the NBE TRPL data for the 7.7% Gd^{3+}:$CsPbBr_3$ NCs summarized in Appendix Figure 4.7. This comparison highlights a key inconsistency between the experimental data and the model of app. 4.3, namely that the experimental $I_{exc}(T)/I_{tot}(T)$ does not go to zero at low temperature. The dashed line is a guide to the eye.

Appendix eq 4.3 describes the scenario of thermal population equilibration between two states, an upper-energy and a lower-energy state, as probed by their PL intensities. Here, the exciton state is higher in energy than the NBE state, and the equilibrium populations are reflected in the intensity ratio I_{exc}/I_{tot}. The PL intensities from each state at each temperature are determined by the radiative decay rate constants (k_{exc} and k_{NBE}) and the Boltzmann populations of each state, *i.e.*, by the energy difference (ΔE) between the two states and the sample temperature (T). In this scenario thermal equilibrium, I_{exc} should go to zero as T approaches 0 K, but the data do not show this behavior (Appendix Figure 4.11).

$$\frac{I_{exc}(T)}{I_{Total}(T)} = \frac{I_{exc}(T)}{I_{exc}(T)+I_{NBE}(T)} = \frac{k_{exc}(T)exp(-\frac{\Delta E}{kT})}{k_{exc}(T)exp\left(-\frac{\Delta E}{kT}\right)+k_{NBE}(T)\left(1-exp\left(-\frac{\Delta E}{kT}\right)\right)} \qquad \text{(App. 4.3)}$$

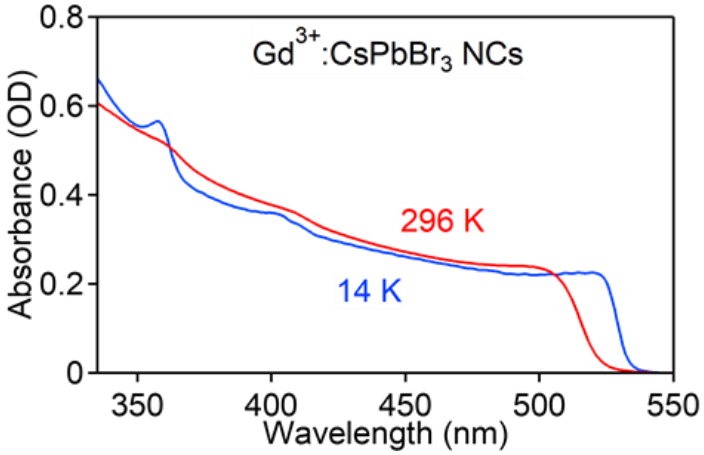

Figure S12. Absorption spectra of a representative sample of 6.6% Gd^{3+}:$CsPbBr_3$ NCs collected at 14 (blue) and 296 K (red).

Chapter 5 Supplementary Material

5.1 Glossary of Abbreviations

Abs – Absorption

CB – Conduction Band

c-Si – Crystalline Silicon

CW – Continuous Wave

DFT – Density Functional Theory

$E_{f\text{-}f}$ – *f-f* Transition Energy

E_g – Bandgap Energy

EQE – External Quantum Efficiency

ES – Excited State

ET – Energy Transfer

eV – Electron volt

FFT – Fast Fourier Transform

FG – Flux Gain

FWHM – Full Width at Half Maximum

GS – Ground State

ICP-AES – Inductively Coupled Plasma Atomic Emission Spectroscopy

LED – Light Emitting Diode

Ln^{3+} -- Lanthanide (III)

LO – Longitudinal Optical

LSC – Luminescent Solar Concentrator

MCPL – Magnetocircular Photoluminescence

NBE – Near Band Edge

NCs -- Nanocrystals

NIR – Near Infrared

OA – Oleic Acid

OAc – Acetate

OAm – Oleylamine

ODE – Octadecene

PCE – Power Conversion Efficiency

PL – Photoluminescence

PLE – Photoluminescence Excitation

PLQY – Photoluminescent Quantum Yield

PV – Photovoltaic

QC – Quantum Cutting

QCE(E/T) – Quantum Cutting Energy (Efficiency/Threshold)

RE^{3+} – Rare Earth (III)

SHJ – Silicon Heterojunction

TA – Transient Absorption

TEM – Transmission Electron Microscopy

TMS-Cl(Br) – Trimethylsilyl Chloride (Bromide)

TR – Time-Resolved

UV – Ultraviolet

VB – Valence Band

VIS – Visible

V_{Pb} – Lead Vacancy

VT – Variable-Temperature

XRD – X-Ray Diffraction

5.2 Acknowledgements

There are so many people to thank for my success in my time here. First and foremost, Professor Daniel Gamelin is acknowledged for his constant mentorship and dedication to science. He has had a major hand in the formulation of new projects, the dissemination of this research, and acquiring funding so each project would only be limited by what is physically possible to measure. Professors Brandi Cossairt, Alexandra Velian, Xiaosong Li, and Vincent Holmberg are acknowledged for their help in the development and review of my thesis. Each committee member was selected for their knowledge of chemical principles and semiconductor physics related to my work. Dr. Daniel Kroupa is acknowledged for his significant contributions to my first two first-author papers and for his mentorship as I was starting to do research in the lab. His guidance quickly catalyzed my ability to do research nearly independently. Professor Sidney Creutz is acknowledged for his mentorship, thoughtful discussion about data, and help with physical characterization of many materials that helped to optimize the synthetic protocols of the materials reported in this thesis. Dr. Matthew Crane is acknowledged for his assistance in physical measurements, bulk material synthesis, and his helpful discussion of data. Drs. Matt Crane and Daniel Kroupa developed the thermal evaporation technique to make high quality bulk thin films of Ln^{3+}:$CsPbX_3$ which have been very useful for comparisons to the nanocrystal data. J.Y. Diana Roh (soon-to-be Dr. J.Y. Diana Roh) is acknowledged for her significant help acquiring important spectroscopic data, mentorship in the laser room, detailed data analysis, and constant discussion about each Yb^{3+}-related project. Drs. David Sommer and Scott Dunham are acknowledged for their contribution as collaborators to the calculations in Chapter 4. Todd Eliason is acknowledged for helping make a plethora of samples for use in many experiments. Chantalle Krajewska is acknowledged for her help in the lab making remarkable samples. She also kept the energy in the lab at an all-time high, and we are thankful to have had her as a group member. The rest of the Gamelin group who overlapped with me in my time here are all acknowledged for their discussion of data and help on maintaining the lab so that effective research can be done. Science is a discipline that requires many people to work together, and I am thankful to have had the people in my group as my colleagues. The Chemistry Department and Molecular Analysis Facility staff that maintain each instrument and teach others how to correctly operate each instrument are also acknowledged for their help. Lochlan Hickok in the chem department's stockroom is also gratefully acknowledged for his constant help with shipping samples, keeping the stockroom open and stocked, and being a great person to talk to. The NSF, DOE, Clean Energy Institute, UW MRSEC, and the WRF are all acknowledged for their helpful funding of our research. My friends and family that have been a part of this journey are dearly acknowledged for their support. Everything from the small coffee breaks to rock climbing and backpacking in some of the most beautiful parts of the Pacific Northwest (PNW) have been memorable and important to me. Three people that deserve special acknowledgement are Andrew Perkins (my coach who has not only taught me everything he knows about Brazilian Jiu Jitsu but also has helped me constantly on and off the mats), Ian Flanigan (my brother who has conversed with me about anything in life from philosophy to science), and Ed Milstein (my father who has supported me since t = 0 and has given me every opportunity I can ask for in life while only asking that I make the most of each opportunity in return).